

University of Strathclyde

Department of Biomedical Engineering

# In Silico size effects in Cancellous Bone

Carl Muscat

PhD. in Biomedical Engineering, 2023



## Abstract

Cancellous bone is a heterogeneous material with a complex lattice microstructure. The description of this microstructure in terms of the mechanical properties of cancellous bone exhibited on the macroscopic scale is important in the understanding of periprosthetic stress concentrations which eventually lead to aseptic loosening or radiolucency in implants.

Micropolar elasticity is a higher order continuum theory which could potentially be used to describe the influence of the microstructure of cancellous bone on its mechanical behaviour at a macroscopic scale. This theory predicts a size effect behaviour in bending and torsion while predicting no size effect behaviour in compression. This has been investigated computationally and validated experimentally using bovine distal femoral trabecular bone. Computational models of various idealised lattice models have also been analysed and compared to priorly investigated models.

It was observed that the idealised lattice models exhibited size effect behaviour as predicted by micropolar theory whilst the experimental models and the computational models of cancellous bone exhibited a size effect behaviour that was opposite to that predicted by micropolar theory.

The ramifications of this are that micropolar theory may not be suitable to model the size effect behaviour of trabecular bone and that further mathematical models and/or idealised lattice arrays may need to be further investigated to create a more accurate representation of trabecular bone. These findings are important because they in silico testing has been validated through experimental testing. Analysis of the stress and strain distributions also provides insight as to why size effects that are opposite to those predicted by micropolar theory have been observed both in silico and experimentally.

## Acknowledgements

I would like to thank my supervisors Dr. Philip Riches and Dr. Marcus Wheel for their continuous help, support, patience, and guidance throughout this research project.

A special thank you is also due to my parents who have always encouraged me in pursuing my studies and education, and for their unconditional support for the duration of this research project.

I would also like to thank the University of Strathclyde for the opportunity in further expanding my education, my research interests, and for the overall incredible experience that this journey has been.

## Declaration

This thesis is the result of the author's original research. It has been composed by the author and has not been previously submitted for examinations which has led to the award of a degree.

The copyright of this thesis belongs to the author under the terms of the United Kingdom Copyright Acts as qualified by the University of Strathclyde Regulations 3.50. Due acknowledgement must always be made of the use of any material contained in, or derived from this thesis.

Signed:

Dated:

# Contents

Abstract.....	2
Acknowledgements.....	3
Declaration.....	4
Contents.....	5
List of Figures .....	9
List of Tables .....	11
1 Introduction .....	1
1.1 – Background .....	1
1.2 – Periprosthetic stress .....	1
1.3 – Modelling of trabecular bone .....	2
1.4 – Outline.....	4
2 Elasticity of Cancellous Bone .....	6
2.1 – Cancellous bone morphology .....	6
2.1.1 – Hierarchical Model of Cancellous Bone .....	6
2.1.2 – Mechanical Properties of Cancellous Bone.....	8
2.2 – Micropolar Elasticity and higher order non-continuum theories .....	11
2.2.1 – Micro-continuum theories .....	12
2.2.2 – Constitutive equations of Micropolar Theory.....	14
2.2.3 – Experiments on micropolar materials.....	20
2.3 – Cancellous bone as a micropolar material.....	22
3 Thesis rationale and objectives.....	25
3.1 – Rationale .....	25
3.2 – Objectives.....	26
4 A mathematical comparison of classical and micropolar elasticity in compression, torsion and bending .....	27
4.1 – Overview .....	27
4.2 – Loading of Micropolar materials.....	27
4.2.1 – Unconfined Uniaxial Compression of Micropolar materials .....	28
4.2.2 – Torsion of Micropolar materials .....	31
4.2.3 – Cantilever Bending of Micropolar materials .....	34
4.3 – Summary .....	39
5 Obtaining a model of Bovine $\mu$ CT samples .....	40
5.1 – Introduction .....	40

5.2 - $\mu$ CT Scanning of a Bovine Distal Femur .....	40
5.2.1 – Sample preparation.....	40
5.2.2 - $\mu$ CT Scanning.....	40
5.3 – Reconstruction .....	42
5.3.1 – Region of Interest.....	43
5.3.2 – Smoothing .....	43
5.3.3 – Misalignment Compensation .....	43
5.3.4 – Ring Artefact Reduction .....	44
5.3.5 – Beam Hardening Correction.....	44
5.4 – Image Processing and Analysis.....	45
5.4.1 – Thresholding.....	45
5.4.2 – Despeckling .....	45
5.4.3 – Morphometric Analysis .....	46
5.4.4 – 3D model generation .....	48
5.5 – 3D model manipulation .....	49
6 FEA of Bovine samples .....	52
6.1 - Introduction .....	52
6.2 – Methodology (ANSYS).....	52
6.2.1 – Compression.....	53
6.2.2 – Bending .....	54
6.2.3 – Torsion.....	56
6.3 – Results and Discussion .....	57
6.3.1 – Compression.....	59
6.3.2 – Bending .....	63
6.3.3 – Torsion.....	66
6.4 – Summary .....	69
7 Idealised models .....	71
7.1 – Introduction .....	71
7.2 - Models used.....	71
7.3 - Mesh sensitivity .....	75
7.4 – Results .....	76
7.4.1 – Compression.....	76
7.4.2 – Torsion.....	81
7.4.3 – Bending .....	85

7.5 – Discussion.....	89
7.6 – Summary .....	90
8 Experimental Validation .....	91
8.1 – Background.....	91
8.2 – 3D Printing.....	92
8.3 - Experimental setting.....	95
8.3.1 - Number of samples.....	95
8.3.2 - Procedure overview .....	96
8.4 – Testing .....	97
8.4.1 – Compression testing.....	97
8.4.2 - Torsion testing.....	100
8.4.3 - Bending test .....	100
8.4.4 – Results .....	100
8.5 – Summary .....	102
9 Discussion and Conclusions .....	104
9.1 – Discussion.....	104
9.2 – Limitations and Further work.....	110
9.3 – Conclusion.....	111
10 References .....	114
11 Appendices.....	121
Appendix 1 – ANSYS script used for compression of bovine samples .....	122
Appendix 2 – ANSYS script used for cantilever bending of bovine samples.....	123
Appendix 3 – ANSYS script used for torsion of bovine samples .....	124
Appendix 4 – ANSYS script used for creation and compression of the regular cross array .....	125
Appendix 5 – ANSYS script used for creation and torsion of the regular cross array.....	126
Appendix 6 – ANSYS script used for creation and cantilever bending of the regular cross array .....	128
Appendix 7 – ANSYS script used for creation and compression of the perturbed array.....	129
Appendix 8 – ANSYS script used for creation and torsion of the perturbed array .....	131
Appendix 9 – ANSYS script used for creation and cantilever bending of the perturbed array ..	133
Appendix 10 – ANSYS script used for creation and compression of the cubic array.....	135
Appendix 11 – ANSYS script used for creation and torsion of the cubic array .....	137
Appendix 12 – ANSYS script used for creation and cantilever of the cubic array .....	139

Appendix 13 – ANSYS script used for creation and compression of the cubic array with added diagonals .....	141
Appendix 14 – ANSYS script used for creation and torsion of the cubic array with added diagonals .....	144
Appendix 15 – ANSYS script used for creation and cantilever bending of the cubic array with added diagonals .....	146

## List of Figures

Figure 2.1: Hierarchical model of trabecular bone .....	7
Figure 2.2: Quarter-staggered structure of collagen fibrils .....	8
Figure 4.1: Schematic for unconfined compression .....	28
Figure 4.2: Schematic for uniaxial torsion .....	31
Figure 4.3: Graphical representation of $T11$ and $M13$ .....	35
Figure 4.4: Cantilever bending .....	37
Figure 5.1: Shadow Transmission Images obtained from the scan .....	42
Figure 5.2: Image preview used for setting the level of misalignment .....	43
Figure 5.3: Distribution of Trabecular Thickness within the scanned sample .....	47
Figure 5.4: Distribution of Trabecular Separation within the scanned sample .....	48
Figure 6.1: Compression loading boundary conditions using Finite Element Analysis (FEA) .....	54
Figure 6.2: Cantilever bending boundary conditions using Finite Element Analysis (FEA). (Boundary conditions in blue represent the master nodes while those in black represent the slave nodes)... 55	55
Figure 6.3: Uniaxial torsion boundary conditions using Finite Element Analysis (FEA). (Boundary conditions in blue represent the master nodes while those in black represent the slave nodes)... 57	57
Figure 6.4: Von-Mises equivalent stresses in the smallest analysed bovine samples under compression..... 59	59
Figure 6.5: Size-effect behaviour of bovine cancellous bone under compression .....	60
Figure 6.6: Von-Mises equivalent stresses in the smallest analysed bovine samples under cantilever bending .....	63
Figure 6.7: Size-effect behaviour of bovine cancellous bone under cantilever bending..... 64	64
Figure 6.8: Von-Mises equivalent stresses in the smallest analysed bovine samples under torsion..... 66	66
Figure 6.9: Size-effect behaviour of bovine cancellous bone under torsion .....	67
Figure 7.1: Unit cell of the regular cross array..... 72	72
Figure 7.2: The regular cross array with multiple unit cells..... 72	72
Figure 7.3: The perturbed array..... 73	73
Figure 7.4: Unit cell of the cubic array .....	73
Figure 7.5: Unit cell of the cubic array with diagonal intersections .....	74
Figure 7.6: Results of the mesh sensitivity studies .....	75
Figure 7.7: Von-Mises Stresses for compression of the cubic array..... 76	76
Figure 7.8: Von-Mises Stresses for compression of the regular cross array..... 77	77
Figure 7.9: Size-effect behavior of computer-generated models under compression..... 79	79
Figure 7.10: Von-Mises Stresses for the regular cross array with perturbations .....	80
Figure 7.11: Von-Mises Stresses for torsion of the cubic array .....	81
Figure 7.12: Von-Mises Stresses for torsion of the regular cross array..... 82	82
Figure 7.13: Von-Mises Stresses fro the regular cross array with added perturbations .....	83
Figure 7.14: Size effect behaviour of computer-generated models compared to the bovine samples .....	84
Figure 7.15: Size effect behaviour of the computer-generated models..... 84	84
Figure 7.16: Von-Mises Stresses for cantilever bending of the cubic array .....	86
Figure 7.17: Von-Mises Stresses for cantilever bending of the regular array .....	86
Figure 7.18: Von-Mises Stresses for cantilever bending of the regular cross array with added perturbations .....	87

Figure 7.19: Size effects for cantilever bending of the computer-generated models.....	88
Figure 7.20: Size effects for cantilever bending of the computer-generated models compared to the bovine samples .....	88
Figure 8.1: The enlarged 3D models that were printed together with plates at the ends .....	92
Figure 8.2: Material properties of Objet Vero .....	93
Figure 8.3: 3D printed bovine samples used for uniaxial torsion together with the added flanges to enable testing .....	94
Figure 8.4: The boundary conditions used for the experimental validation (a) not allowing surface warping ( $u_y, u_z=0$ ) and for the finite element simulations (b) allowing surface warping ( $u_y, u_z \neq 0$ ) ..	94
Figure 8.5: The boundary conditions used for finite element simulations (a) and for experimental validation (b) .....	95
Figure 8.6: Compression testing of samples using the Bose Electroforce 3200 .....	97
Figure 8.7: The Instron Electropuls E3000 .....	97
Figure 8.8: A graph of compressive load vs displacement for one of the samples .....	99
Figure 8.9: Results for compression of the bovine samples using the Bose Electroforce 3200 (different points indicate different samples with error bars indicating standard error for each sample).....	100
Figure 9.4: Fitting of a quadratic function to the in-silico data for compression testing .....	108
Figure 9.5: Fitting of a quadratic function to the in-silico data for cantilever bending.....	109
Figure 9.6: Fitting of a quadratic function to the in-silico data for torsion testing .....	109

## List of Tables

Table 5.1: Summary of 3D Morphometric Analysis in CTAn.....	47
Table 5.2: The number of bovine samples tested using finite element analysis (FEA) for each size	49
Table 8.1: The number of samples tested experimentally for each size .....	96

# 1 Introduction

## 1.1 – Background

Knee/hip replacement has become a popular treatment of osteoarthritis in musculoskeletal medicine. Osteoarthritis in joints such as the knee and hip has become a highly common problem especially in people aged over 60 years. (Dagenais et al., 2009; Davies et al., 2002; Felson et al., 1987; Quintana et al., 2008) Joint replacement surgery has been proven to be both successful and a cost-effective remedy for such diseases. However, there has been a higher prevalence of such cases especially in younger patients. (Grotle et al., 2008)

This means that implants are expected to be more durable and cause less problems for the patients in the long term. With the developments in implant research, wear related problems have been reduced to a point where implants are expected to last twenty years or possibly even more. However, one ensuing problem is the weakening of bone in the area immediately surrounding such implants. This weakening occurs because of a difference in material properties between trabecular bone and the implant material. The stiffness and strength of implants are usually higher than those of bone. This results in the implant being loaded to a higher degree than the bone immediately surrounding the implant area. In turn, the bone in the areas around the implant are subjected to a lower magnitude of stresses (also known as stress shielding). This causes resorption of bone due to increased osteoclast activity which in turn causes degradation of bone in the area immediately surrounding the implant and eventually leads to aseptic loosening. Aseptic loosening can in turn cause the formation of debris in the area immediately surrounding the implant. This can also cause the formation of osteolytic lesions. A better understanding of the stress and strain behaviour characterising trabecular bone is essential to minimise bone resorption and aseptic loosening due to stress shielding. Such an understanding would help in further optimising the design and material properties of implants and thus lead to a reduction in stress shielding together with the issues that this leads to.

## 1.2 – Periprosthetic stress

Stress shielding occurs around implants because of a difference in stiffness between the implant and bone; the stiffness of the implant is usually much higher than that of bone, which results in a higher load being transferred through the implant rather than through the bone. Because of this, bone is being loaded to a lower degree.

According to Wolff's law, bone adapts to the loads that are being applied to it by resorbing and reconstructing minerals such that the new structure can withstand the required loads. (Frost, 1994) This means that loads of lower magnitude cause osteocytes in bone to resorb bone minerals whilst osteoblasts are stimulated to reconstruct bone to a lesser degree. This results in an overall loss in bone volume density which also means that trabecular bone becomes weaker. The weakening of trabecular bone causes further problems at the interface between the implant and bone since this tends to cause loosening of the implant (aseptic loosening) which then results in the need for reconstructive/revision surgery. (Klein-Nulend et al., 2013)

It has been shown (Della Rocca et al., 2011) that 30% of total knee arthroplasty (TKA) failures occur due to aseptic loosening; which further indicates that a reduction in periprosthetic stresses is required for patients undergoing total knee arthroplasty or any other kind of arthroplasty. In order to reduce the effects that stress shielding has on the area immediately surrounding implants, it is essential to obtain a better understanding of the localized periprosthetic stress environment so that implants can be eventually designed in such a way that their mechanical properties match more closely with those of trabecular bone, and thus, stress shielding can be mitigated. It is important to note that in the design stage, implants and bone are normally modelled using continuum theories: microstructural effects of bone are rarely taken into consideration which may result in less than optimal implant designs. For this reason, a suitable theory that incorporates the effects of the microstructure should be used to model the mechanical behaviour of trabecular bone. (Della Rocca et al., 2011)

### 1.3 – Modelling of trabecular bone

Trabecular bone can be modelled on a multitude of scales; the nano-scale, the micro-scale and the macro-scale. In the nano-scale, the individual trabeculae are considered to have voids such as the lacunae and canaliculae. These properties of these nano-structures are then used to model the individual trabeculae. In the micro-scale, bone is considered to be made up of trabeculae which are modelled using a variety of material models ranging from homogenous linear elastic models to heterogenous non-linear material models (McPhee et al., JMBBM, 2023; Stefanek et al., JMBBM, 2023). These are then used to model bone on a microstructural level. In the macro-scale, bone is considered an elastic material with lower properties than those of the structures in the macro and nano scales due to the voids present in the structure. Within this thesis, the effects that

the micro-scale structure and properties have on the macro-scale behaviour of trabecular bone have been analysed and the together with the relationship between the micro-scale and macro-scale.

The micro-scale mechanical properties of trabecular bone can be said to depend on the mechanical properties of the individual trabeculae (i.e. the composition of such trabeculae), the relative bone density and the topology of trabecular architecture including but not limited to factors such as the trabecular thickness, trabecular length and trabecular cell shape. In the case of trabecular bone, it can be said that classical continuum theory loses its accuracy. The first reason for this is because in classical continuum theory that the properties of the material are assumed to be uniformly distributed throughout its volume. In the case of trabecular bone, this does is not the case since on a microstructural level one can observe that the structure is made up of voids that vary in size in such a way that the overall mechanical properties and material density are not uniformly distributed. Another reason for the loss in accuracy when using classical continuum theories is that in the case of bone, the loading conditions create strains that have a magnitude which is on the same scale as the microstructural cell size. As a direct consequence of this, one can observe the occurrence of size effects, which cannot be modelled using classical continuum theories. The term “size effect” refers to a change in mechanical behaviour as the macroscopic sample size changes in relation to the microstructural cell size.

In the past there have been various studies where size effects were observed in structures that are similar to trabecular bone such as soil, concrete, numerous metallic foams etc. One way of accounting for such size effects is by discretely modelling each wall/face of the microstructure in such a way that an accurate representation of the deformations on a microstructural level can be created and used to predict the macroscopic behaviour of the material. This has also been done in the case of trabecular bone by modelling trabecular bone on the microstructural level (micro-FE models) and characterising trabeculae using a variety of material models such as linear, homogenous, non-linear and heterogenous material models amongst others). The main disadvantage of doing this is that such a model requires a very large amount of time and computational power due to the complex nature and the sheer amount of elements used in such models. This occurs especially in the case of trabecular bone where the microstructure observes a very complex and apparently random pattern. Another approach is to use generalized non-continuum theory where the individual microstructural details are averaged out into a single characteristic length (the trabecular length in the case of trabecular bone). This characteristic length is then used within a micropolar material model so that the size effect behaviour of the material can

be described on the macro-scale without the need for modelling on the micro-scale. Thus, reducing the required time and computational power to characterise material behaviour. This thesis is the first step along such a path; the averaged out characteristic properties of bone was used to model the micro-scale behaviour and relate this to the macro-scale response.

#### 1.4 – Outline

In Chapter 1, a background for the whole setting of this thesis is given. This revolves around the reason why there is a need to better understand how modelling of trabecular bone can be made more accurate. The problem with periprosthetic stress and aseptic loosening is discussed together with the reason why microstructural effects should be included when modelling trabecular bone. Chapter 1 also includes a general overview of what has been done so far with the modelling of trabecular bone and how this thesis aims to improve on these models.

In Chapter 2, a literature search detailing the hierarchical model and mechanical properties of trabecular bone is presented together with various properties on the nano, macro, and micro scales. A background of micropolar theory is also presented together with the constitutive equations and derivations for loading in unconfined uniaxial compression, torsion and cantilever bending. This is done since micropolar theory is the theory that is used in this thesis and samples were loaded in these three loading modes. Chapter 2 also details some experiments that have been done on micropolar materials together with studies on considering trabecular bone as a micropolar material.

Chapter 3 details how the micro-scale structure and behavior of trabecular bone affects implants in terms of stress shielding and periprosthetic loosening and how this is related to the studies that have already been carried out. Chapter 3 also describes the importance of creating a model of bone using non-continuum theories such as micropolar theory to create a continuum model of trabecular bone, which leads to the defining the aims and objectives of this thesis.

Chapter 4 details a general overview of the experimentation phase. During this phase, a description of the three loading modes used in testing is given together with a derivation of the equations relating micropolar theory, elastic theory and these three different loading modes. A general overview of the finite element (FE) models used to carry out in silico testing is also given together with a description of all the models used, mesh sensitivity studies and the number of samples tested for each model.

In Chapter 5, the procedure for obtaining a micro-CT 3D image of bovine trabecular bone is described together with the various image manipulation techniques that were used up to the final phase where CDB files were generated. These can be used in ANSYS to apply loads to the 3D models. Various image manipulation techniques had to be used to modify the images within a reasonable range so that the models work in ANSYS. Such techniques included despeckling, thresholding, and smoothing amongst others.

Chapter 6 is a continuation of Chapter 5. In Chapter 6, the CDB files generated in Chapter 5 were loaded in ANSYS under 3 loading modes; unconfined uniaxial compression, uniaxial torsion and cantilever bending. The results from the finite element analysis of these models are also presented, analysed and discussed.

Chapter 7 goes on to detail the creation of various idealized models that are computer generated using an APDL script. These models were loaded in the same way as the CDB files used for finite element analysis in Chapter 6 and the results were analysed. The idealized models were created so that results from the bovine samples (CDB files) could be compared to these idealized models for any relation to micropolar theory (the observation of a size effect behaviour in this case).

Chapter 8 describes an experimental procedure that was used to validate the finite element models that were modelled and analysed in the previous chapters. This experiment consisted of carrying out unconfined uniaxial compression on two different machines. The samples used in this experiment were the same as the bovine samples. However, these were enlarged, and 3D printed. This was done so that it could be ensured that the microstructure of the samples was the same as that from the modelled samples.

Chapter 9 discusses the results that were obtained together with their accuracy. A description of the significance of these results and how they impact the knowledge about modelling of trabecular bone is also given together with any and potential sources of error. This section also summarises the main findings and conclusions of this study, while explaining the significance of these results, their relevance and impact in the context of lattice materials and in a biomedical setting.

## 2 Elasticity of Cancellous Bone

Wolff's law states that bone adapts itself to the loading conditions according to the direction of the principal stresses. (Frost, 1994) Hence, if the loading conditions change, the bone starts remodelling itself over time according to the new loading conditions. In the case of implants, there is a relatively lower stress in the bone because the implant material is normally stiffer. This means that stresses transferred to the bone are of lower magnitude resulting in stress shielding. In such cases bone adapts to the new loading conditions by osteolysis (break down of bone resulting in lower density and strength) in the area immediately surrounding the implant which is reflected in a phenomenon known as radiolucency. It has been shown that the amount of osteolysis due to stress shielding that occurs after implantation is dependent on two main factors; the type of implant, and the interface between the bone and implant. (Cristofolini et al., 2009; Gøthesen et al., 2013; Sathappan et al., 2009) It is also theorised that the size of the implant may be related to the potential mechanisms of failure. (Baggi et al., 2008) The most common failure mechanism in implants is caused by periprosthetic loosening, which in turn is caused by two main factors; implant particle wear that leads to the release of debris material that causes bone resorption/osteolysis, and micromotion of the implant itself due to inadequate/defective fixation. (Bauer & Schils, 1999) The nature of this micromotion suggests that a standard continuum material model may not be enough to accurately model trabecular bone. If a continuum model of cancellous bone can be created using micropolar theory, the micromotion of the implant can be modelled more accurately, thus, the behaviour of the implant may be better predicted in terms of failure mechanisms. This would eliminate the need for modelling trabecular bone on a microstructural level and including the structure individual trabeculae within the model. Thus, reducing the complexity of the model, whilst also reducing the need for more computational power and reducing the time needed for processing such complex models.

### 2.1 – Cancellous bone morphology

#### 2.1.1 – Hierarchical Model of Cancellous Bone

As discussed previously, the structure and properties of cancellous bone can be studied at a variety of scales; the macro-scale, the micro-scale and the nano-scale. This section aims to give an overview of properties on each scale with particular emphasis on the micro-scale. In this section, particular emphasis is put on the micro-scale. This because this study seeks to further understand the

behaviour of the microstructure of cancellous bone to reduce the effects of periprosthetic loosening and stress shielding.

Cancellous bone, also known as trabecular bone is a type of bone that is highly vascularised and porous. It can be found at the end of long bones, spinal vertebrae, ribs, the skull and in the bones of joints. On the macro-scale, cancellous bone is much softer than cortical bone on the macro-scale. The micro-scale consists of trabeculae arranged in a lattice that gives it a spongy appearance and enables it to contain bone marrow.

The trabeculae that make up cancellous bone can be observed in the nano-scale and they are made of osteocytes embedded in bone matrix within cavities called lacunae. Trabecular sizes have been shown to vary between 0.4mm to 0.9mm approximately while trabecular thickness has been shown to be in the range of 0.04mm to 0.14mm depending on anatomical region. (Bakar et al., 2019) The osteocytes can take on nutrients and expel waste through the canaliculi. On the surface of the trabeculae, one can also find osteoclasts (that have the capability of absorbing bone for restructuring purposes) and osteoblasts that have the capability of creating bone matrix so that eventually lamellae are created to form the individual trabeculae as shown in Figure 2.1.

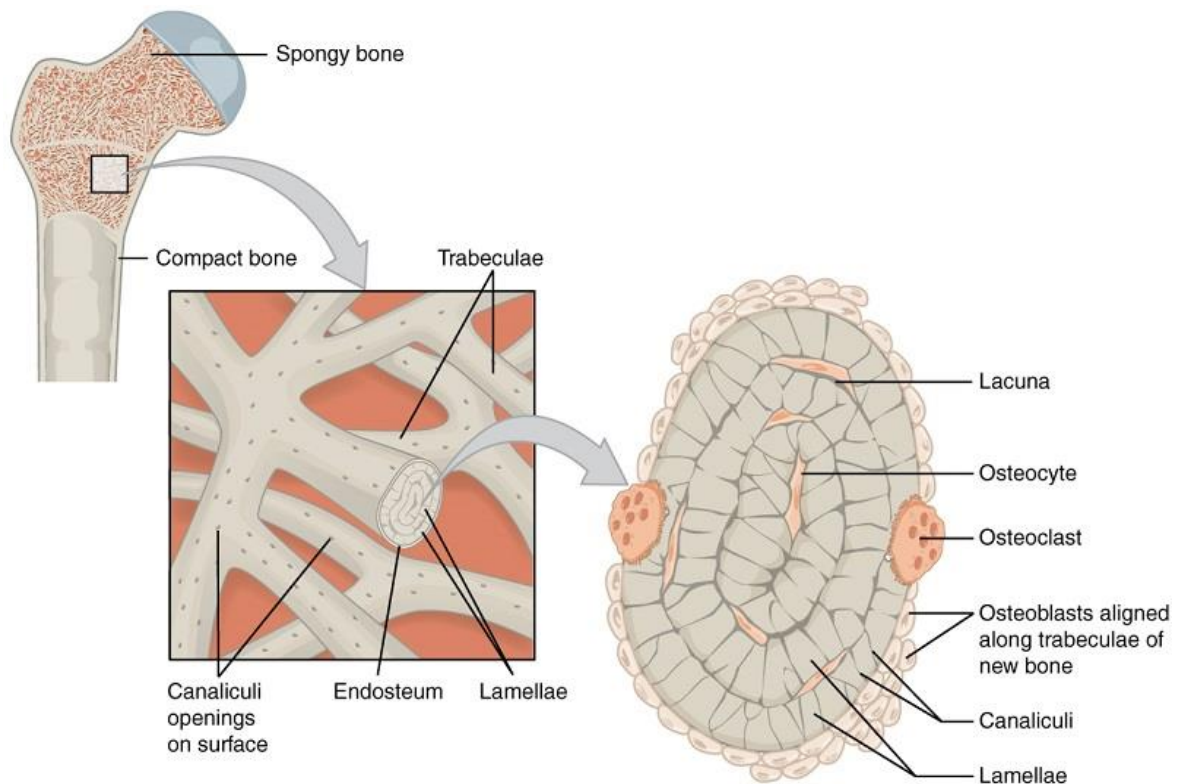


Figure 2.1: Hierarchical model of trabecular bone

The trabeculae in cancellous bone can have three main cellular structures; rod-rod, rod-plate, and plate-plate and they are aligned according to the principal stress directions in the bone. Trabecular thickness can range from 50 to 400µm in diameter. (Clarke, 2008)

The lamellae are made up of bone matrix with a thickness of 3 to 7µm and they are aligned according to the orientation of the trabeculae. The bone matrix consists of an organic phase and an inorganic phase. The inorganic phase is made up of mineral hydroxyapatite in the form of  $\text{Ca}_{10}[\text{PO}_4]_6[\text{OH}]_2$  that provides rigidity and strength to the structure. These crystals are relatively small, and they have two main functions; providing the ability to include various ions in the structure, and to provide structural rigidity to the organic phase. As the bone matures, the hydroxyapatite crystals fuse and undergo some changes in composition (calcification) that increases the density of bone. The organic phase is unmineralized in nature and around 90% of it consists of type 1 collagen whilst also having small traces of types 2,5, and 10 collagen in it. The rest is mostly made of noncollagenous proteins such as glycoproteins and proteoglycans. Collagen can mainly be found in the form of fibrils that provide elasticity and flexibility to the structure. These fibrils are arranged in a quarter-staggered structure having cross-links between the molecules as shown in Figure 2.2. Calcification of the

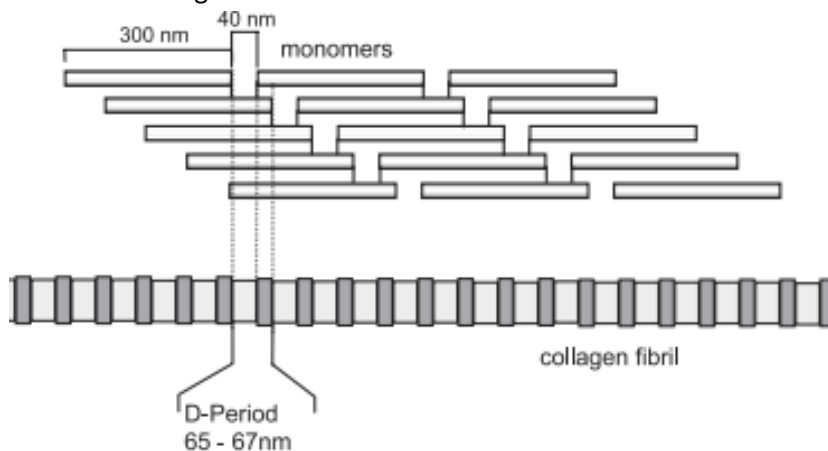


Figure 2.2: Quarter-staggered structure of collagen fibrils

inorganic phase occurs in the gaps between these cross-links causing the longitudinal axes of apatite crystals to be aligned with the collagen fibrils such that between the cross links, a layered structure of alternating organic and inorganic phases may be found within the matrix. (Clarke, 2008; Patterson-Kane & Firth, 2014)

### 2.1.2 – Mechanical Properties of Cancellous Bone

Cancellous bone is known to be highly porous, heterogenous and anisotropic on a macroscopic level. It has a lower ash fraction (around 33.9%), lower calcium content than cortical bone and is also

characterised by a lower density ( $1.8744\text{gcm}^{-3}$ ). These properties are required because it is more active in terms of being remodelled according to the principal stresses acting in the bone as stipulated by Wolff's law. (Frost, 1994) This remodelling causes the newly formed bone to have a lower mineral content than older bone.

Because of all these factors, the properties of cancellous bone are dependent on two main factors; the chemical composition of the individual trabeculae, and the microstructural architecture (referring to the density and orientation of the trabeculae at a particular location). (Dyson & Whitehouse, 1968; Gong et al., 1964) At the trabecular level (micro-scale), the elastic properties are mostly affected by collagen content and the mineral orientations. This because these are the main building blocks of trabeculae. It is important to note that both collagen content and mineral orientations are usually the same in all types of cancellous bone. The size, location and number of lacunae in the lamellae of a trabecula also affect the elastic properties on the micro-scale since they cause an increase in stress concentration in the longitudinal direction of the trabecula, which can cause damage on the trabecular level. (McNamara et al., 2006)

There have been many studies that have tried to obtain the elastic properties of cancellous bone on the macro-scale, however; due to the variation in properties at different location such studies give a wide range in which the Young's modulus can lie. For this reason, studies have been carried out to obtain the Young's modulus of individual trabeculae using various methods such as ultrasonic testing, mechanical testing and nanoindentation amongst others.

A method that was used in the past to determine the properties of individual trabeculae is buckling analysis. In 1975, Townsend et al, used this method to determine the elastic modulus of individual human trabeculae from a proximal tibia. They found that wet specimens exhibited ductile buckling while dry specimens exhibited brittle buckling. They also extrapolated the data they collected to ideal slenderness ratios and concluded that the Young's modulus was 11.38GPa for wet samples and 14.13GPa for dry samples. (Townsend et al., 1975)

In 1999, Turner et al carried out a study using two different techniques for obtaining the properties of human trabecular bone; ultrasonic testing and nano-indentation. They found that the Young's modulus was 17.5GPa and 18.14GPa for each technique respectively. They also compared these values to the longitudinal, transverse and average properties of cortical bone, concluding that the Young's modulus of trabecular bone falls between the average and transverse moduli for cortical

bone. They also conclude that nano-indentation can be used to determine both the Young's modulus and the degree of anisotropy of trabecular bone. (Turner et al., 1999)

A variety of studies have also been carried out using nano-indentation on trabecular bone of both human and porcine samples. The Young's modulus in each study was found to be in the range of 11.4-21.8GPa depending on the anatomical region from where the sample is taken. (Ko et al.; Rho et al., 1999; Roy et al., 1996; Turner et al., 1999; Zysset et al., 1999)

Rho et al. (1993) used ultrasonic testing and found that the Young's modulus of individual trabeculae was 14.8GPa when ultrasonic testing was used, whilst a value of 10.4GPa was obtained using mechanical testing. (Rho et al., 1993)

Zysset et al. (1999) went on to further confirm this range using nanoindentation. Using this method, it was found that the Young's modulus of individual trabeculae had a value of  $11.4 \pm 5.6$ GPa. Considering both of these studies, the elastic modulus of individual trabeculae was assumed to be 12GPa in the case of finite element models created in this study. (Zysset et al., 1999)

Further to the linear elastic properties on both the macro-scale and the micro-scale that have been discussed above. It is also well known that bone exhibits time dependent properties on the macro-scale. This means that poro-elasticity and visco-elasticity are also theories that could contribute to the accurate modelling of trabecular bone. Santino et al, in 2013 used micro-CT images to determine the macro-scale poro-elastic behaviour of bone by modelling the trabeculae together with bone marrow using finite element analysis. (Sandino et al.)

Lim and Hong in 2005 also devised a method to determine the macro-scale pore-elastic properties of trabecular bone through mechanical testing. (Lim & Hong, 2000) On the other hand, Bravo et al in 2019 concluded that trabecular bone also exhibits visco-elastic behaviour and that it is critical to include the effects of bone marrow to model such behaviour. (Bravo et al., 2019)

Apart from the efforts to characterise the properties of trabecular bone experimentally, some studies have also tried to do this by using a variety of techniques such as finite element modelling, and various scanning techniques. Dall'Ara et al. in 2011 concluded that quantitative CT scanning provided a significantly more accurate of vertebral strength in an in vitro environment when compared to X-ray absorpimetry, however, this would need to be validated for in vivo models (Dall'Ara et al., 2012). In 2013, Dall'Ara et al. also went on to use quantitative computed tomography (QCT) to create a non-linear homogenised volume finite element model of trabecular

bone. From this, it could be concluded that such models can accurately predict mechanical properties while also providing qualitative information about failure location (Dall'Ara et al., 2013). In 2013, Zysset et al. compares finite element models of trabecular bone obtained through quantitative CT scanning, to models obtained using densitometric standards and concludes that finite element models are more accurate in their prediction of experimental bone strength (Zysset et al., 2013). In 2017, Dall'Ara et al. also uses micro-CT scanning together with digital volume correlation to obtain the mechanical properties of trabecular bone (Dall'Ara et al., 2017). In 2021, Buccino et al. created models that were capable of localising fracture sites. (Buccino et al., 2021) This also gives insight into the prediction of trabecular bone behaviour and modelling on the micro-scale. In 2022, Guha et al. also used CT imaging to create a continuum model for mechanical modelling of trabecular bone. In this study, the bone mineral density was used in conjunction with voxel data to create a heterogenous continuum model. (Guha et al., 2022)

All these studies fail to take into account the size effect behaviour of trabecular bone. Apart from this, the creation of such models that also model the structure of trabecular bone on a microstructural level and include details on the trabecular level require a significant amount of processing to create the geometric model itself whilst also requiring a significant amount of computational power to run the finite element simulation. The main focus on this study was to characterise the size-effect behaviour of trabecular bone such that this can be incorporated into a non-continuum model on the macro-scale (micropolar theory) thus eliminating the need for modelling the microstructure of trabecular bone and reducing processing time together with computational power demands when creating models for implant design. Eventually such a model can be continuously improved by even incorporating non-linear, anisotropic and heterogenous material constitutive laws. In this study, the main focus was on the effect of the microstructure of trabecular bone and how this affects the macro-scale behaviour. This means that the macro-scale properties as obtained in other studies using poro-elasticity and visco-elasticity are not within the scope of this thesis, but rather, the micro-scale properties and how these relate to the behaviour of bone on the macro-scale.

## 2.2 – Micropolar Elasticity and higher order non-continuum theories

The previous section contains an analysis of what has been done in the past to model bone. This mostly consists of analysing the properties of trabecular bone on the macro-scale. Poro-elasticity, visco-elasticity and classical linear elasticity have been utilised to describe the behaviour of bone in

both the macro-scale and micro-scale. However, all of these theories are called continuum theories. This means that the sample is considered to be continuous without the presence of any voids. In this case, the aim is to analyse the behaviour of bone in the micro-scale. On this scale, there is the presence of a multitude of voids. This means that there is the need for a non-continuum theory to describe bone on such a scale. One such theory is a micro-continuum theory developed by A.C. Eringen in 1960.

### 2.2.1 – Micro-continuum theories

Micro-continuum theories were first introduced in the 1960s by A.C. Eringen (Eringen, 1966), and they are a group of theories for materials with a microstructure such as cellular solids. For the scope of this thesis, it can be noted that trabecular bone was considered a cellular solid. In classical elasticity, a material particle has a certain position that is irrespective of its orientation. In the case of micro-continuum theories, the orientation of such particles is also taken into account, which results in the addition of extra degrees of freedom for each material particle when compared to the classical continuum theories. This means that in micro-continuum theories an additional object called the “director” is added to each material particle and this defines the orientation of the material point. Hence, it can be noted that in classical continuum theories, the motion (macro-scale motion) of a material point/particle is fully defined by a deformation vector. On the other hand in micro-continuum theories, material particles can undergo an additional micro-motion, that corresponds to the deformation and rotation on the micro-scale (Pabst, 2005). There are various micro-continuum theories which consider the effect of this micro-motion such as micromorphic, microstretch, micropolar and couple stress theories. (Eringen, 1966),

In the case of micromorphic theory, each material point is considered to have three deformable directors on the micro-scale. This results in the introduction of nine additional degrees of freedom ( $\psi_{ij}$ ) which are dimensionless. These additional degrees of freedom include three micro-rotations and six micro-deformations. This can be thought of as a micro-element embedded in the continuum which can rotate and deform independently from the deformation of the macro-element. Eringen (Eringen, 1966) describes the micro-motion using a two-index variable (director) denoted by  $\chi_{kK}$  that represents an additional nine degrees of freedom (on the micro-scale). Three of these degrees of freedom are related to the micro-rotations while the other six are related to the deformations on the micro-scale. Micromorphic theory can be applied to practically all materials, however, its complexity limits its practical usefulness due to the amount of testing required to obtain material constants when applying such a theory. (Eringen, 1966),

In the case when the director ( $\chi_{kK}$ ) becomes orthogonal, the material can be said to exhibit isotropic expansion/contraction on the micro-scale in addition to the other three micro-rotations. This means that shear micro-deformations are no longer allowed and each material point is only left with four additional degrees of freedom on the micro-scale (one isotropic micro-deformation, and three micro-rotations). The isotropic expansion/contraction (micro-deformation) is also called stretch and is represented by  $\chi$ , while the three micro-rotations are represented by  $\phi_i$ . This special case of micromorphic theory is also called microstretch theory.

If an assumption is made that the directors are orthonormal and rigid, this would mean that the directors  $\chi_{kK}$  and  $\chi_{lK}$  have a relationship to the Kronecker Delta ( $\delta_{kl}$ ) such that:

$$\chi_{kK}\chi_{lK} = \delta_{kl}$$

*Equation 2.1*

The Kronecker Delta is defined as a diagonal square matrix consisting of ones and zeros such that:

$$\delta_{kl} = \begin{bmatrix} 1 & 0 & \dots \\ 0 & 1 & \dots \\ \dots & \dots & \dots \end{bmatrix}$$

This means that each material point does not have any stretch and only has three independent additional degrees of freedom on the micro-scale representing the rotation of each micro-element ( $\phi_i$ ). An assumption of this type results in the simplification of microstretch theory to what is defined as micropolar theory. A further simplification of micropolar theory occurs when the rotations of the micro-elements are assumed to be dependent on the deformations of the macro-element. This results in a special theory called couple-stress theory. (Eringen, 1966),

It is important to note that in all of the above three theories, the macro-motion is still given the usual deformation function that is used in classical continuum mechanics ( $\chi_k$ ).

This thesis puts particular emphasis on micropolar theory because it is the theory that is simplest and contains the least amount of variables. Couple stress theory could also be considered in this case but it could not be ascertained whether there is a relationship between the micro-rotations and macro-translations, so the next level of complexity to consider is micropolar theory. Future work could also assess the potential use of microstretch and/or micromorphic theory to describe the micro-scale behavior of trabecular bone despite the complexity and level of physical testing required to obtain material constants when using such theories. (Eringen, 1966),

### 2.2.2 – Constitutive equations of Micropolar Theory

Micropolar theory is described in full in a journal written by A.C. Eringen in 1966 (Eringen, 1966), this chapter summarises the theory to obtain the constitutive equations for linear micropolar elasticity.

In micropolar elasticity, the deformation function is defined as  $\chi_k$  and the director as  $\chi_{kK}$ . Then, the deformation gradient due to macro-motion can be defined as  $\chi_{k,K}$  which is a second-order tensor defined by:

$$\chi_{k,K} = \frac{\partial \chi_k(X_K, t)}{\partial X_K}$$

*Equation 2.2 (Pabst, 2005)*

Where  $X$  represents the position of any material point. After this, the micro-rotation gradient  $\chi_{kK,L}$  can also be defined and it is given by

$$\chi_{kK,L} = \frac{\partial \chi_{kK}(X_L, t)}{\partial X_L}$$

*Equation 2.3 (Pabst, 2005)*

It is important to note that the indices after a comma denote a partial derivative and that the determinant  $\det \chi_{kK}$  represents changes in the micro-volume. Since in the case of micropolar theory it is assumed that there are no changes in the micro-volume (because of stiff directors) it can be said that  $\det \chi_{kK} = 1$ .

For micropolar theory to work, two conditions with regards to the determinant of the director and the deformation gradient cause by macro-motions are needed. These specify that:

$$\det \chi_{k,K} > 0$$

*Equation 2.4 (Pabst, 2005)*

And

$$\det \chi_{kK} > 0$$

*Equation 2.5 (Pabst, 2005)*

In micropolar theory, two deformation tensors are of very high importance; The Cosserat tensor  $C_{KL}$  and the Wryness tensor  $W_{KL}$ . These are defined in relation to the gradients and directors mentioned above such that:

$$C_{KL} = \chi_{k,K} \chi_{kL}$$

Equation 2.6 (Pabst, 2005)

$$W_{KL} = \frac{1}{2} \varepsilon_{KMN} \chi_{kM,L} \chi_{kN}$$

Equation 2.7

Where  $\varepsilon_{KMN}$  is the Levi-Civita symbol. The Levi-Civita symbol is similar to the Kronecker Delta in that it is also a diagonal matrix consisting of ones and zeros. However, as indicated by its index notation, it is a three-dimensional matrix.

These deformation Cosserat tensor ( $C_{KL}$ ) and the Wryness tensor ( $W_{KL}$ ) are fundamental to the construction of the constitutive equations of micropolar solids.

It is also important to define the two second order tensors  $a_{kl}$  and  $b_{kl}$ , which are defined as:

$$a_{kl} = V_{k,l} + \varepsilon_{lkm} v_m$$

Equation 2.8 (Pabst, 2005)

$$b_{kl} = v_{k,l}$$

Equation 2.9 (Pabst, 2005)

Where  $V_{l,k}$  is the velocity gradient,  $v_m$  is the microgyration vector and  $v_{k,l}$  is its gradient.

In micropolar theory, the directors are assumed to be rigid, thus, the micromotion of the directors can be described as rigid body rotation having an angle of rotation  $\phi$  around an axis  $n_k$ . This means that a microrotation tensor can be defined in such a way that it is related to  $\phi$  through the relation:

$$\chi_{kl} = \chi_{kK} \delta_{KL} = \cos \phi \delta_{kl} - \sin \phi \varepsilon_{klm} n_m + (1 - \cos \phi) n_k n_l$$

Equation 2.10 (Pabst, 2005)

In this case  $\delta_{kl}$  denotes the cosine directors of the spatial and material frames. When these two frames are chosen to be the same  $\delta_{kl}$  becomes the Kronecker delta.

Similarly, the microgyration vector can be related to the time derivative of rotation (rate of rotation)  $\dot{\phi}$  by:

$$v_k = \dot{\phi}n_k + \sin \phi \dot{n}_k + (1 - \cos \phi)(\mathbf{n} \times \dot{\mathbf{n}})_k$$

*Equation 2.11 (Pabst, 2005)*

For very small angles  $\phi$ , the approximations  $\sin \phi \approx \phi$  and  $\cos \phi \approx 1$  can be used such that the microgyration vector ( $\dot{\phi}$ ) is approximately equal to the rotational velocity  $\dot{\phi}_k$  where  $\dot{\phi}_k = \overbrace{\dot{\phi}n_k}^{\dot{\phi}_k} = \dot{\phi}n_k + \phi \dot{n}_k$  such that:

$$\begin{aligned} v_k &= \dot{\phi}n_k + \sin \phi \dot{n}_k + (1 - \cos \phi)(\mathbf{n} \times \dot{\mathbf{n}})_k \\ v_k &= \dot{\phi}n_k + \phi \dot{n}_k + (1 - 1)(\mathbf{n} \times \dot{\mathbf{n}})_k \\ v_k &= \dot{\phi}n_k + \phi \dot{n}_k \\ v_k &= \overbrace{\dot{\phi}n_k}^{\dot{\phi}_k} \\ v_k &= \dot{\phi}_k \end{aligned}$$

*Equation 2.12 (Pabst, 2005)*

### *Balance Laws*

In Micropolar theory, there are various balance laws that need to be applied so that the constitutive equations for solids can be obtained. These are the laws of conservation of mass, conservation of linear momentum, balance of angular momentum and conservation of microinertia. All these laws are also used to obtain the constitutive equations for classical elasticity with the only exception of the conservation of microinertia (since the micro-scale is not considered in classical continuum elasticity). In cases where there is heat transfer through a micropolar solid, the balance of energy (first law of thermodynamics) and entropy inequality (Second law of thermodynamics) are also added to these laws. These laws are not relevant to the scope of this study and will thus be ignored since in this case no heat transfer through cancellous bone is being considered.

The law of conservation of mass states that the mass of the solid before and after deformation must be equal. This means that the density ( $\rho$ ) and the velocity vector ( $V_k$ ) can be related by :

$$\dot{\rho} = \rho V_{k,k}$$

*Equation 2.13(Pabst, 2005)*

By using the balance of linear momentum, a relationship between the stress tensor ( $T_{kl}$ ), velocity tensor ( $V_k$ ), density ( $\rho$ ), and the body force per unit mass ( $f_1$ ) can be established such that:

$$T_{kl,k} + \rho(f_l - \dot{V}_l) = 0$$

Equation 2.14 (Pabst, 2005)

Similarly, by using the balance of angular momentum, a relationship between the couple stress tensor ( $M_{kl}$ ), the body couple per unit mass ( $l_1$ ) and the micro-rotational micro-acceleration ( $\dot{\sigma}_l$ ) can be established such that:

$$M_{kl,k} + \varepsilon_{lmn} T_{mn} + \rho(l_l - \dot{\sigma}_l) = 0$$

Equation 2.15 (Pabst, 2005)

*Note: The micro-rotational micro-acceleration, is related to the micro-inertia ( $I_{kl}$ ) and micro-gyration ( $v_l$ ) through the equation:  $\dot{\sigma}_k = \dot{\widehat{I_{kl} v_l}}$ .*

If the conservation of microinertia is also applied in this case, the microinertia tensor ( $I_{kl}$ ) can be related to the micro-gyration vector ( $v_k$ ) using the equation:

$$\dot{I}_{kl} + (\varepsilon_{kpr} I_{lp} + \varepsilon_{lpr} I_{kp}) v_r = 0$$

Equation 2.16 (Pabst, 2005)

### *Micropolar Solids*

The nonlinear constitutive equations of micropolar solids can be obtained as a function of the free energy when considering no changes in temperatures. It can be said that the free energy ( $\Psi$ ) is a function of three variables, such that  $\Psi = \Psi(C_{KL}, W_{KL}, I_{kl})$ .

From this relation, equations for the stress tensor ( $T_{kl}$ ) and for the couple stress tensor ( $M_{kl}$ ) can be obtained that relate these tensor to the director and deformation gradient as defined in the previous sections. These relationships are described by:

$$T_{kl} = \rho \frac{\partial \Psi}{\partial C_{KL}} \chi_{k,K} \chi_{l,L}$$

Equation 2.17(Pabst, 2005)

$$M_{kl} = \rho \frac{\partial \Psi}{\partial W_{LK}} \chi_{k,K} \chi_{lL}$$

Equation 2.18 (Pabst, 2005)

Assuming that deformations and strain measurements are linear, the linear and rotational deformations can be introduced and defined as:

$$\varepsilon_{kl} = u_{l,k} + \varepsilon_{lkm} \phi_m$$

Equation 2.19 (Pabst, 2005)

$$\gamma_{kl} = \phi_{k,l}$$

Equation 2.20 (Pabst, 2005)

Where  $u_l$  is the displacement vector and  $\phi_m$  is the rotation vector given by  $\phi_m = \phi n_m$ .

Note that these rotation vectors do not represent physical characteristics within the model but are described as micro-rotations describing the position of an element within the continuum which affects the linear position of the material itself in terms of stiffness and an/isotropy.

This eventually leads to the relations:

$$T_{kl} = A_{klmn} \varepsilon_{mn} + C_{klmn} \gamma_{mn}$$

Equation 2.21 (Pabst, 2005)

$$M_{kl} = B_{lkmn} \gamma_{mn} + C_{mnlk} \varepsilon_{mn}$$

Equation 2.22 (Pabst, 2005)

In the case of linear elastic micropolar solids, the internal energy can be calculated by using a quadratic approximation similar to what is done in classical continuum mechanics. This means that the free energy becomes:

$$\Psi = \Psi_0 - \frac{1}{\rho} A_{kl} \varepsilon_{kl} - \frac{1}{\rho} B_{lk} \gamma_{lk} + \frac{1}{2\rho} A_{klmn} \varepsilon_{kl} \varepsilon_{mn} + \frac{1}{2\rho} B_{lkmn} \gamma_{lk} \gamma_{mn} + \frac{1}{2\rho} C_{klmn} \varepsilon_{kl} \gamma_{mn}$$

Equation 2.23 (Pabst, 2005)

Where:

- $A_{kl}, B_{kl}, C_{kl}$  are second order tensors
- $A_{klmn}, B_{klmn}$  and  $C_{klmn}$  are fourth order tensors that possess the symmetries  $A_{klmn} = A_{mnlk}$  and  $B_{klmn} = B_{mnlk}$

By doing this, we can obtain the following equations for the stress and moment tensors respectively:

$$T_{kl} = \rho \frac{\partial \Psi}{\partial \varepsilon_{kl}}$$

Equation 2.24 (Pabst, 2005)

$$M_{kl} = \rho \frac{\partial \Psi}{\partial \gamma_{lk}}$$

Equation 2.25 (Pabst, 2005)

In the case of linear, elastic isotropic solids, the fourth order tensors representing the material moduli can be simplified by:

$$A_{klmn} = \lambda \delta_{kl} \delta_{mn} + (\mu + \kappa) \delta_{km} \delta_{ln} + \mu \delta_{kn} \delta_{lm}$$

$$B_{klmn} = \alpha \delta_{kl} \delta_{mn} + \beta \delta_{kn} \delta_{lm} + \gamma \delta_{km} \delta_{ln}$$

$$C_{klmn} = 0$$

This means that the linear constitutive equations of isotropic micropolar solids can be simplified to equations relating

- The stress tensor to the strain tensor and material properties  $\lambda, \mu$  and  $\kappa$ .
- The moment tensor to the rotation vector and the material properties  $\alpha, \beta$  and  $\gamma$ .

$$T_{kl} = \lambda \varepsilon_{mm} \delta_{kl} + (\mu + \kappa) \varepsilon_{kl} + \mu \varepsilon_{lk}$$

Equation 2.26 (Pabst, 2005)

$$M_{kl} = \alpha \gamma_{mm} \delta_{kl} + \beta \gamma_{kl} + \gamma \gamma_{lk}$$

Equation 2.27 (Pabst, 2005)

This means that such solids are characterised by six elastic constants;  $\lambda, \mu, \kappa, \alpha, \beta, \gamma$ . These equations are only valid for homogenous solid (single phase). It is important to note that apart from these constants, the response of a micropolar continuum is also characterised by the microinertia tensor  $I_{kl}$ . In this case, this tensor is assumed to have only one single component such that the continuum is also isotropic on the micro-scale (micro-isotropic) and  $I_{kl} = I \delta_{kl}$ . This implies that the

law of balance of microinertia reduces to  $\dot{I} = 0$ . Certain conditions must also be met for the material to be thermodynamically stable (Pabst, 2005), these conditions are:

$$3\lambda + 2\mu + \kappa \geq 0$$

$$2\mu + \kappa \geq 0$$

$$\kappa \geq 0$$

$$3\alpha + \beta + \gamma \geq 0$$

$$\gamma + \beta \geq 0$$

$$\gamma - \beta \geq 0$$

### 2.2.3 – Experiments on micropolar materials

Obtaining micropolar elastic constants from the exhibited size effects in micropolar materials is a challenge that many people have tried to undertake. As one may note from the above equations for micropolar theory, the apparent stiffness of a material should be observed to decrease as the size of a sample increases. The change in stiffness of a material as the size of the sample changes is termed a size effect. Throughout the years there have been many attempts to characterise the micropolar constants from the size effects observed in materials.

Gauthier and Jahsman (1975) came up with a technique to quantify all the six micropolar elastic material constants by analysing the response of an idealised material with rigid inclusions using theoretical equations and experimentally under torsion and bending. The equations predicted stiffening as the size of the sample decreases (concurrent with the equations of micropolar theory). However, when they carried out experiments they could not come to any conclusions because some of the results exhibited negative size effects where stiffening of the sample was observed as the size increased. Bigoni et al. (2007) have since suggested that the main cause of observance of negative size effects was because the inclusions were stiffer than the matrix material. (Bertoldi et al., 2007; Gauthier & Jahsman, 1975)

There have been many attempts to characterise micropolar properties of different materials through experimental procedures by various authors. One of the most prolific authors is Lakes, he has carried out various studies on many materials to try and determine micropolar properties from experimental studies. In 1995 he provided a general overview of the experimental procedures to obtain micropolar material properties. This was followed by other studies on specific materials such as polyurethane foams, porous solids, cortical bone and even cancellous bone. However, such experimental methods have not been compared to numerical analyses to identify what is the cause of micropolar or anti-micropolar size effects. (Anderson & Lakes, 1994; Lakes, 1986; Lakes, 1983; Lakes, 1995; Yang & Lakes, 1982)

It has been noted that in some cases, the stiffness of the sample is observed to increase with size. (Anderson & Lakes, 1994; Brezny & Green, 1990) This is not predicted by analytical solutions and is referred to as an anti-micropolar size effect. Anderson and Lakes have suggested that the anti-micropolar size effects occur due to damage on the surface region of the specimens. They have suggested that due to the processes carried out when preparing the samples for testing, the surface region of the sample may be considered as a region of damage. This region of damage is postulated to mask the true micropolar material behaviour in such cases. (Anderson & Lakes, 1994) Brezny and Green have suggested that the exhibition of anti-micropolar size effects arises from an inadequate cell size to weight ratio. They postulate that there is a critical ratio that reduces the influence of any surface region to the true micropolar material properties. (Brezny & Green, 1990) The issues regarding surface effects are mentioned in both studies as one of the major problems with deriving micropolar material properties experimentally. It can be said that if the surface condition affects the results, micropolar size effects will not be observed in the material when tested experimentally. However, computational analyses of such samples would help in determining whether the size effect behaviour is dependent on surface condition whilst also giving indications about the effects of sample preparation on the mechanical behaviour of the samples.

It has been shown that micropolar size effects can be observed under three-point bending when testing a planar idealised heterogenous material both computationally and experimentally. In both cases the material consisted of a homogenous material matrix with an array of voids. (Beveridge, 2011; Beveridge et al., 2010; Beveridge et al., 2013; Waseem et al., 2013) It was concluded that the characteristic length in bending depends on the density of voids in the material and is of the order of the void size in terms of magnitude. A study by Forest, Barb et al. 2000, was also carried out to try and relate micropolar material properties to the microstructure of the material. In this study, a

simplified heterogeneous material was modelled by using discrete sections of different material properties. It was concluded that the observed size effect might be directly related to the microstructure when micropolar behaviour is observed. (Forest et al., 2000)

It has been suggested that micropolar size effects (positive) can be observed in cortical bone. (Buechner & Lakes, 2003; Lakes, 1995; Park & Lakes, 1986; Yang & Lakes, 1982) There have also been cases where negative size effects were observed in cortical bone (Choi et al., 1990; Wheel et al., 2015), however, the reason for the exhibition of negative size effects is still unknown and could be due to a multitude of factors such as cross-section specimen shape and surface finish amongst others. Cancellous bone has been assumed to exhibit similar behaviour but on a different length scale than cortical bone and there were various studies trying to create idealised homogenised models of trabecular bone to extract micropolar. (Ibrahim Goda et al., 2012; Goda et al., 2013a; Ramézani et al., 2012)

Daszkiewicz et al. also observed size effects in cancellous by using micro-CT scans to create finite element models under different loading conditions. This study consisted of analysing the effects that boundary conditions have on the size effect behaviour of cancellous bone and the conclusions were that kinetic uniform boundary conditions tend to decrease stiffness with growing size while periodicity-compatible mixed uniform boundary conditions tend to increase stiffness with growing size. This study was all carried out in silico and fails to analyse the behaviour in vitro/ in vivo. This means that it is still unknown how this change in stiffness affects the behaviour of cancellous bone when it comes to testing in vitro, and the effect that these size effects have on the overall performance of cancellous bone within the human body is still unknown. (Daszkiewicz et al., 2017)

Cancellous bone is much less dense than cortical bone and can be compared to materials of low densities such as polyurethane foams. These materials have been studied by Anderson & Lakes and they concluded that if the microstructure is on the scale of global geometry, the size effect observed is of a much higher magnitude. (Anderson & Lakes, 1994)

### 2.3 – Cancellous bone as a micropolar material

Cancellous bone has a very complex structure both in terms of its hierarchy and in terms of its microstructural geometry. This results in questioning whether classical elasticity is enough to describe this level of detail. Classical elasticity assumes that the material consists of a continuum model made of a specific material model which can range from homogenous isotropic linear elastic models to heterogeneous anisotropic non-linear models. However, this is not the case in cancellous

bone, especially at small length scales. Such an assumption may only be valid in cases where the size of the sample is extremely large, this because in these cases scale of the microstructure is much smaller than the macroscale where deformations are occurring, making the material essentially a non-continuum model.

Previous studies on cortical bone by Lakes and Choi respectively have shown that the scale of the specimen plays a crucial role in the exhibition of size effects. Lakes observed that in cases where the scale of the specimen is larger than the microstructural details, the specimens exhibit a positive size effect (i.e. conforming with micropolar theory). Choi, on the other hand observed negative size effects (i.e. the opposite of what micropolar theory predicts) in specimens whose size was on the level of microstructural details. (Choi et al., 1990; Park & Lakes, 1986) In the context of this thesis, this behaviour is also referred to as anti-micropolar behaviour. It is however still uncertain whether this difference in size effect behaviour occurs due to specimen size or surface preparation, despite the fact that in a more recent study by Wheel et al., it is theorised that such anti-micropolar behaviour could be caused by surface defects/preparation of the samples. (Wheel et al., 2015)

Not many experimental studies have been carried out on cancellous bone where size effect behaviour is concerned. Mostly due to the very small sample size requirements. It is however suspected that the large difference in apparent density between trabecular bone and cortical bone may be a cause for different size effect behaviour. There have been some studies on polyurethane foams, whose geometrical microstructure is similar to cancellous bone and as such a similar size effect behaviour can be expected in cancellous bone. This study demonstrated that polyurethane exhibit Cosserat material properties, leading to an exhibition of size effects where the stiffness increases with decreasing specimen size. It was also observed in this study that the surface conditions have a drastic effect on the size effect behaviour and that surface corrugations/imperfections during machining of the specimens leads to a decrease in stiffness as the specimen size decrease. (Anderson & Lakes, 1994; Wheel et al., 2015)

Ramezhani et al. has also carried out a study where micro-CT scans of cancellous bone are taken and modelled as micropolar materials. However, in this study, cancellous bone is only assumed to act as a micropolar behaviour and there is no investigation with regards to whether the size effects exhibited are micropolar in nature or anti-micropolar. (Ramézani et al., 2012)

The main focus when it comes to cancellous bone has been more on finite element modelling of idealised heterogenous models. This because it is much easier to load finite element models rather

than experimental models. Such studies can also help in providing a general idea of the stress and strain environment within the microstructure, thus providing a better understanding with regards to how cancellous bone is able to withstand loading. Boundary conditions for in vitro testing may also prove to be another challenge for implementation as theoretical boundary conditions can be much easier to implement in silico rather than in vitro. This issue can however be bypassed by validating in silico models using the boundary conditions used in vitro. Then, based on this validation, in silico models with theoretical boundary conditions can be created to ascertain whether cancellous bone truly exhibits micropolar behaviour or not in terms of size effect behaviour. Creating idealised heterogenous models also provides an opportunity to understand which structures mimics cancellous bone the best so that eventually cancellous bone can be modelled without the need for creating microstructural details in finite element models. This can be very helpful in the making the design of prosthetics much more accurate without increasing the computational time required.

## 3 Thesis rationale and objectives

### 3.1 – Rationale

The design of the interface between biological tissue and a non-biological object (prosthesis) is one of the main problems in the design of artificial joints. Prosthetic design is based on the correct load transfer between the prosthesis and the biological tissue (bone in this case). For this reason, an understanding of the stress and strain behaviour in actual bone is essential so that bone can be modelled, and the prosthesis can be designed accordingly. Implants and prosthetics both interact with the microstructure of cancellous bone during normal function. This is done either directly or through a cement interface. (Hogan, 1992) The mechanism of occurrence and the development of such an interaction is also important in determining the durability and lifecycle of prosthetics and implants. (Huiskes, 1990) Micropolar elasticity predicts that stress concentrators such as circular holes or rigid inclusions in a micropolar material give a lower overall stress magnitude when compared to classically elastic material. (Eringen, 1966; Gitman, 2012) If cancellous bone is found to exhibit micropolar behaviour, then it could be said that classical elasticity is not completely accurate. An implant may be regarded as a rigid inclusion in cancellous bone, this means that the stress and strain behaviour immediately surrounding the implant would be totally different than the behaviour predicted by classical elasticity. Hence, this would be a scenario where micropolar elasticity would be more appropriate to model the stress and strain behaviour in cancellous bone.

The main aim of the thesis is to determine whether a continuum model of cancellous bone can be created using existing continuum elasticity theories. In particular, micropolar theory will be assessed with regards to its applicability for cancellous bone. A secondary aim is to determine whether a regularised heterogeneous microstructure behaves mechanically similarly to cancellous bone, as this may also have modelling advantages. In achieving either of these two aims, such models could be implanted in finite element models of implants to better predict stress shielding within cancellous bone that is adjacent to the implant material without the need to model individual trabeculae. This may lead to the avoidance of radiolucency and thus a lower occurrence of periprosthetic loosening of implants would be observed.

These aims will be achieved using a combination of in-silico experiments of cancellous bone structures, which are validated by in vitro experiments of exactly the same structures of cancellous bone. In silico experiments of regularised heterogeneous materials will also be compared to the in-

silico results from cancellous bone. (Anderson & Lakes, 1994; Bioengineering Conference Big Sky, 1999; Ibrahim Goda et al., 2012; Goda et al., 2013a; Goda et al., 2013b; I. Goda et al., 2012; Ramézani et al., 2012) The novelty of this research lies in the fact that finite element models will be validated through experimental testing together with the fact that the applicability of micropolar theory to cancellous bone is assessed rather than assumed. By using micropolar theory, the accuracy of finite element modelling of trabecular bone may be increased while also decreasing the computational power demands of such simulations. This because the need to model individual trabeculae on a microstructural level would be avoided and replaced by incorporating the effects of such a microstructure into a micropolar material model.

### 3.2 – Objectives

To address the above aims, the objectives of the thesis are therefore:

1. To develop a mathematical understanding of the comparison of the behaviour of micropolar materials with conventional, Hookean, mechanical behaviour. This will identify the types of experiments required to ascertain the applicability of each theory to experimental results.
2. To create a high-resolution model of bovine trabecular bone.
3. To create a suite of in-silico experiments in compression, bending and torsion by multisampling of the created high-resolution model.
4. To repeat the in-silico suite of experiments on regularised microstructures of similar scale to cancellous bone and compare them to the equivalent cancellous bone model.
5. To manufacture cancellous bone samples of identical structure to the in-silico models and experimentally test them, in the same modes, to validate the numerical models.
6. To conclude whether trabecular bone exhibits sufficient size-effect behaviour to warrant further investigation of such a phenomenon in a periprosthetic setting.

## 4 A mathematical comparison of classical and micropolar elasticity in compression, torsion and bending

### 4.1 – Overview

In the previous sections, the objectives of this study have been established and background information relating micropolar theory to trabecular bone has been provided. This section will be providing the experimental setup for testing the various samples and models of trabecular bone and establishing whether the size-effect behaviour exhibited by cancellous bone is sufficient to warrant further investigation into whether micropolar theory (or any other non-continuum theory) can be used to create a continuum model of cancellous bone that predicts these size effects.

In the experimental phase, three loading modes are used; unconfined uniaxial compression, uniaxial torsion, and cantilever bending. Because of this, before starting the experimental setup, micropolar equations were derived within this chapter since these three loading modes are also used to predict material behaviour in each case.

### 4.2 – Loading of Micropolar materials

In this study, three loading conditions were used on all models; unconfined uniaxial compression, cantilever bending, and uniaxial torsion. As such, it was important to understand how micropolar materials behave under these loading conditions and which material dependent properties can be obtained from each tested loading conditions. The following sections indicate the theoretical approach and predicted response of micropolar materials when loaded in the above-mentioned loading conditions while also relating the material properties to the readings obtained from each test.

#### 4.2.1 – Unconfined Uniaxial Compression of Micropolar materials

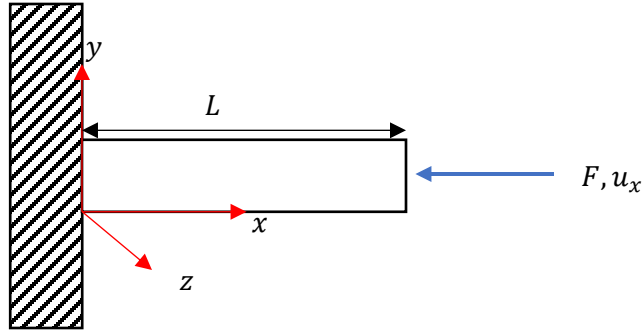


Figure 4.1: Schematic for unconfined compression

When a micropolar solid is loaded in unconfined uniaxial compression, the moment tensor  $M_{kl} = 0$  whilst the stress tensor is:

$$T_{kl} = \begin{bmatrix} T_{11} & T_{12} & T_{13} \\ T_{21} & T_{22} & T_{23} \\ T_{31} & T_{32} & T_{33} \end{bmatrix} = \begin{bmatrix} T_{11} & 0 & 0 \\ 0 & 0 & 0 \\ 0 & 0 & 0 \end{bmatrix}$$

From Equation 2.26, we know that:

$$T_{kl} = \lambda \varepsilon_{mm} \delta_{kl} + (\mu + \kappa) \varepsilon_{kl} + \mu \varepsilon_{lk}$$

$$T_{11} = \lambda \varepsilon_{11} \delta_{11} + (\mu + \kappa) \varepsilon_{11} + \mu \varepsilon_{11}$$

However, from Equation 2.19:

$$\varepsilon_{kl} = u_{l,k} + \varepsilon_{lkm} \phi_m$$

Note that  $\varepsilon_{lkm}$  is the Levi-Civita symbol.

This means that:

$$\varepsilon_{kl} = \varepsilon_{lk} = \varepsilon_{11} = \frac{\partial u_x}{\partial x} + \varepsilon_{113} \phi_3$$

$$T_{11} = \lambda \varepsilon_{11} \delta_{11} + (\mu + \kappa) \left( \frac{\partial u_x}{\partial x} + \varepsilon_{113} \phi_3 \right) + \mu \left( \frac{\partial u_x}{\partial x} + \varepsilon_{113} \phi_3 \right)$$

But in the case of uniaxial unconfined compression,  $\varepsilon_{113} = \phi_3 = 0$ ,  $\frac{\partial u_x}{\partial x} = \varepsilon_{11}$ , and  $\delta_{11} = 1$ . Thus;

$$T_{11} = \lambda \varepsilon_{11} + (2\mu + \kappa) \varepsilon_{11}$$

$$T_{11} = \varepsilon_{11} (\lambda + 2\mu + \kappa)$$

$$\frac{T_{11}}{\varepsilon_{11}} = \lambda + 2\mu + \kappa$$

Now, from classical elasticity,

$$F = kx$$

$$\frac{F}{L} = k\varepsilon_{11}$$

$$\frac{F}{AL} = \frac{k\varepsilon_{11}}{A},$$

$$\frac{T_{11}}{L} = \frac{k\varepsilon_{11}}{A}$$

$$T_{11} = \frac{kL\varepsilon_{11}}{A}$$

$$E = \frac{T_{11}}{\varepsilon_{11}} = \frac{kL}{A}$$

Where  $E$  is the Young's Modulus,  $F$  is the force applied,  $k$  is the stiffness,  $x$  is the extension,  $L$  is the length of the sample along the axis of compression,  $\varepsilon_{11}$  is the strain in the direction of the axis of compression,  $A$  is the cross-sectional area perpendicular to the axis of compression, and  $T_{11}$  represents the compressive stress in this case.

By comparison,

$$\frac{kL}{A} = \lambda + 2\mu + \kappa$$

In our case,  $A = d^2$  (where  $d$  is the cross-sectional edge length) since the samples were cut to have a square cross-section, and  $l = 2d$  where  $d$  is the cross-sectional edge length. Thus:

$$E = \frac{2kd}{d^2} = \lambda + 2\mu + \kappa$$

$$E = \frac{2k}{d} = \lambda + 2\mu + \kappa$$

$$\frac{E}{2} = \frac{k}{d}$$

$$E = \lambda + 2\mu + \kappa$$

$$\frac{E}{2} = \frac{k}{d} = \frac{(\lambda + 2\mu + \kappa)}{2}$$

Equation 4.1

From classical continuum theories:

$$\sigma = E\varepsilon, F = kx \text{ and } U = \frac{1}{2}kx^2$$

Where  $E$  is the apparent Young's Modulus, and  $U$  is the strain energy within the material.

This means that:

$$k = \frac{2U}{x^2}$$

Equation 4.2

In such a case, the energy from the results in finite element models can be obtained, and the extension is predetermined, this means that the apparent stiffness can be calculated.

Equation 4.1 shows that  $\frac{k}{d}$  is directly proportional to the Young's Modulus. This means that if the size of the geometry is varied without altering the aspect ratio, the variable  $\frac{k}{d}$  should remain the same and thus no size effects should be exhibited in uniaxial compression in this case according to Micropolar theory.

Upon further examination of Equation 4.1, it can be observed that the Young's Modulus ( $E$ ) is also directly proportional to  $\lambda + 2\mu + \kappa$ .  $\lambda$  and  $\mu$  are the Lamé parameters which are related to the Young's Modulus and Poisson's ratio through:

$$\lambda = \frac{Ev}{(1+v)(1-2v)}$$

$$\mu = G = \frac{E}{2(1+v)}$$

This means that the only material constant in Equation 4.1, that specifically relates to micropolar theory is the Cosserratt couple modulus  $\kappa$ . If we consider the situation where  $\kappa \rightarrow 0$ , the apparent stiffness  $\frac{k}{d} \rightarrow \frac{\lambda+2\mu}{2}$  which means that the apparent stiffness becomes  $\frac{k}{d} = \frac{E}{2}$ .

#### 4.2.2 – Torsion of Micropolar materials

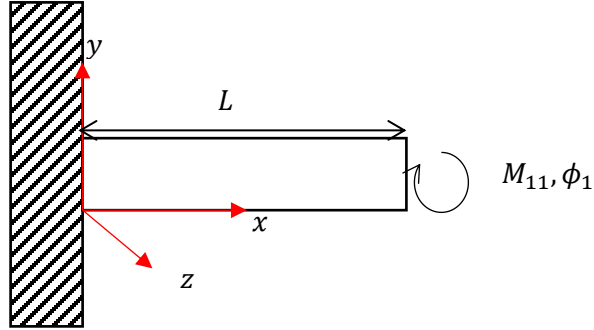


Figure 4.2: Schematic for uniaxial torsion

In the case of torsion, the moment tensor has the form:

$$M_{kl} = \begin{bmatrix} M_{11} & M_{12} & M_{13} \\ M_{21} & M_{22} & M_{23} \\ M_{31} & M_{32} & M_{33} \end{bmatrix} = \begin{bmatrix} M_{11} & 0 & 0 \\ 0 & 0 & 0 \\ 0 & 0 & 0 \end{bmatrix}$$

From Equation 2.27, we know that:

$$M_{kl} = \alpha \gamma_{mm} \delta_{kl} + \beta \gamma_{kl} + \gamma \gamma_{lk}$$

Also from Equation 2.20:

$$\gamma_{kl} = \phi_{k,l}$$

$$\gamma_{lk} = \phi_{l,k}$$

This means that:

$$M_{11} = \alpha \gamma_{11} \delta_{11} + \beta \phi_{1,1} + \gamma \phi_{1,1}$$

$$M_{11} = \alpha \gamma_{11} \delta_{11} + \beta \frac{\partial \phi_1}{\partial x} + \gamma \frac{\partial \phi_1}{\partial x}$$

But the variation of angle with  $x$  is given by:  $\phi_1(x) = \frac{M_{11}x}{JG} \Rightarrow \frac{\partial \phi_1}{\partial x} = \frac{M_{11}}{JG}$ , and  $\gamma_{11} = \phi_1$

$$M_{11} = \alpha \phi_1 + (\beta + \gamma) \left( \frac{M_{11}}{JG} \right)$$

Where  $G$  is the modulus of rigidity and  $J$  is the polar moment of area.

We know that:

$$G = \frac{k_\phi L}{J}$$
$$\Rightarrow JG = k_\phi L$$

Hence:

$$M_{11} = \alpha\phi_1 + (\beta + \gamma) \left( \frac{k_\phi \phi_1}{k_\phi L} \right)$$

$$M_{11} = \alpha\phi_1 + (\beta + \gamma) \left( \frac{\phi_1}{L} \right)$$

Now  $M_{11} = k_\phi \phi_1$

$$k_\phi \phi_1 = \phi_1 \left( \alpha + \frac{\beta + \gamma}{L} \right)$$

$$k_\phi = \left( \alpha + \frac{\beta + \gamma}{L} \right)$$

$$k_\phi = \alpha + \frac{\beta + \gamma}{L}$$

But in this case  $L = 2d$ :

$$k_\phi = \alpha + \frac{\beta + \gamma}{2d}$$

*Equation 4.3*

Equation 4.3 shows that as the size of the sample increases ( $d \rightarrow \infty$ ), the stiffness  $k_\phi \rightarrow \alpha$  which means that as the size of the sample increases, the exhibited stiffness becomes constant similar to the case of classical elasticity.

Considering a classical elastic continuum, the rotation of a section of material is described by:

$$\phi_1 = \frac{M_{11}L}{JG}$$

$$M_{11} = \frac{JG\phi_1}{L}$$

Where  $J$  is the polar moment of area of the cross-section, and  $G$  is the modulus of rigidity.

In this case  $J = \frac{d^4}{6}$ :

$$M_{11} = \frac{d^3 G \phi_1}{12}$$

Torque is also related to the torsional stiffness  $k_\phi$  by the equation  $M_{11} = k_\phi \phi_1$ . This means that in the case of classic elasticity we would have the relation:

$$k_\phi = \frac{d^3 G}{12}$$

If we substitute the above into Equation 4.3, for the case of infinitesimally large samples ( $\alpha = k_\phi$ ), we get:

$$k_\phi = \frac{d^3 G}{12} + \frac{\beta + \gamma}{2d}$$

*Equation 4.4*

This means that for micropolar samples, the torsional stiffness would be proportional to the shear modulus and then added to another variable dependent on the size of the material and the Cosserat twist moduli ( $\beta$  and  $\gamma$ ).

If Equation 4.4 is normalised to obtain a value for  $k_\phi$  that is independent of sample size and directly proportional to the shear modulus, we get:

$$\frac{k_\phi}{d^3} = \frac{G}{12} + \frac{\beta + \gamma}{2d^4}$$

*Equation 4.5*

Since  $\frac{k_\phi}{d^3}$  is also related to the geometry of the material ( $d$ ), it can also be noted that the apparent stiffness of the material is expected to change as the size of the sample is varied (even if the same aspect ratio is maintained). Thus the apparent shear stiffness is inversely related to the size of the sample meaning that as the sample grows smaller ( $d \rightarrow 0$ ), Micropolar theory predicts a stiffening effect in uniaxial torsion. On the other hand, as the sample size increases ( $d \rightarrow \infty$ ), Micropolar theory predicts a decrease in stiffness such that  $\frac{k_\phi}{d^3} \rightarrow \frac{G}{12}$ .

#### 4.2.3 – Cantilever Bending of Micropolar materials

In the case of bending, the stress tensor has the form:

$$T_{kl} = \begin{bmatrix} T_{11} & T_{12} & T_{13} \\ T_{21} & T_{22} & T_{23} \\ T_{31} & T_{32} & T_{33} \end{bmatrix} = \begin{bmatrix} 0 & 0 & 0 \\ 0 & 0 & 0 \\ 0 & 0 & T_{33} \end{bmatrix}$$

From Equation 2.26, we know that:

$$T_{kl} = \lambda \varepsilon_{mm} \delta_{kl} + (\mu + \kappa) \varepsilon_{kl} + \mu \varepsilon_{lk}$$

Thus:

$$T_{33} = \lambda \varepsilon_{33} \delta_{33} + (\mu + \kappa) \left( \frac{\partial u_z}{\partial z} + \varepsilon_{331} \phi_3 \right) + \mu \left( \frac{\partial u_z}{\partial z} + \varepsilon_{331} \phi_3 \right)$$

Since  $\varepsilon_{331} = 0$  and  $\frac{\partial u_z}{\partial z} = \varepsilon_{33}$ ;

$$T_{33} = \varepsilon_{33} (\lambda + 2\mu + \kappa)$$

But  $\varepsilon_{33} = \frac{y_A}{R}$  where R is the radius of curvature, and  $y_A$  is the distance from the neutral axis.

$$T_{33} = \frac{y_A (\lambda + 2\mu + \kappa)}{R}$$

The moment tensor becomes:

$$M_{kl} = \begin{bmatrix} M_{11} & M_{12} & M_{13} \\ M_{21} & M_{22} & M_{23} \\ M_{31} & M_{32} & M_{33} \end{bmatrix} = \begin{bmatrix} 0 & 0 & M_{13} \\ 0 & 0 & 0 \\ 0 & 0 & 0 \end{bmatrix}$$

From Equation 2.27, we know that:

$$M_{kl} = \alpha \gamma_{mm} \delta_{kl} + \beta \gamma_{kl} + \gamma \gamma_{lk}$$

This means that:

$$M_{13} = \alpha \gamma_{mm} \delta_{13} + \beta \gamma_{13} + \gamma \gamma_{31}$$

These are represented in Figure 4.3.

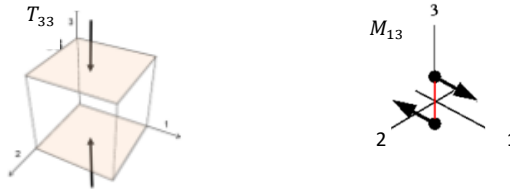


Figure 4.3: Graphical representation of  $T_{11}$  and  $M_{13}$

But:

$$\delta_{13} = 0$$

$$\gamma_{13} = \phi_{1,3} = \frac{\partial \phi_x}{\partial z} = 0$$

$$\gamma_{31} = \phi_{3,1} = \frac{\partial \phi_z}{\partial x} = \frac{1}{R} = -\frac{d^2 y_A}{dx^2}$$

Hence:

$$M_{13} = \frac{\gamma}{R}$$

Equating the internal moments to the external moments:

$$M = \int_A y_A T_{11} + M_{13} dA$$

$$M = \int_A y_A \frac{y_A(\lambda + 2\mu + \kappa)}{R} + \frac{\gamma}{R} dA$$

$$M = \frac{1}{R} \int_A y_A^2 (\lambda + 2\mu + \kappa) + \gamma A$$

$$M = \frac{1}{R} \left\{ (\lambda + 2\mu + \kappa) \int_A y_A^2 dA + \gamma \int_A dA \right\}$$

Now:

$$\int_A y_A^2 dA = I \text{ and } \int_A dA = A$$

$$M = \frac{I(\lambda + 2\mu + \kappa) + \gamma A}{R}$$

$$\frac{1}{R} = \frac{M}{I(\lambda + 2\mu + \kappa) + \gamma A}$$

$$\frac{d^2 y_A}{dx^2} = -\frac{M}{I(\lambda + 2\mu + \kappa) + \gamma A}$$

We can say that  $M(x) = F(L - x)$

$$\frac{d^2 y_A}{dx^2} = -\frac{F(L - x)}{I(\lambda + 2\mu + \kappa) + \gamma A}$$

$$\frac{dy_A}{dx} = -\frac{F}{I(\lambda + 2\mu + \kappa) + \gamma A} \int_0^L (L - x) dx$$

$$\frac{dy_A}{dx} = -\frac{F}{I(\lambda + 2\mu + \kappa) + \gamma A} \left[ -\frac{x^2}{2} + Lx \right]_0^L + C_1$$

but at  $x = 0$ ,  $\frac{dy_A}{dx} = 0$ . This means that  $C_1 = 0$

$$\frac{dy_A}{dx} = -\frac{F}{I(\lambda + 2\mu + \kappa) + \gamma A} \left[ -\frac{x^2}{2} + Lx \right]_0^L$$

$$y_A = -\frac{F}{I(\lambda + 2\mu + \kappa) + \gamma A} \left[ -\frac{x^3}{6} + \frac{Lx^2}{2} \right]_0^L + C_2$$

But at  $x = 0$ ,  $y_A = 0$ . This means that  $C_2 = 0$

$$y_A = -\frac{F}{I(\lambda + 2\mu + \kappa) + \gamma A} \left[ -\frac{x^3}{6} + \frac{Lx^2}{2} \right]_0^L$$

Thus at  $x = L$ :

$$y_A = -\frac{FL^3}{3\{I(\lambda + 2\mu + \kappa) + \gamma A\}}$$

$$F = y_A \frac{3\{I(\lambda + 2\mu + \kappa) + \gamma A\}}{L^3}$$

Comparing this to the equation for bending stiffness;  $F = ky_A$ :

$$k = \frac{3\{I(\lambda + 2\mu + \kappa) + \gamma A\}}{L^3}$$

Substituting  $I = \frac{d^4}{12}$ ,  $A = d^2$  and  $L = 2d$ :

$$k = \frac{3\{d^4(\lambda + 2\mu + \kappa)\}}{12 \times (2d)^3} + \frac{3\gamma d^2}{(2d)^3}$$

$$k = \frac{\{d^4(\lambda + 2\mu + \kappa)\}}{4 \times 8d^3} + \frac{3\gamma d^2}{8d^3}$$

$$k = \frac{(\lambda + 2\mu + \kappa)d}{32} + \frac{3\gamma}{8d}$$

$$\frac{k}{d} = \frac{(\lambda + 2\mu + \kappa)}{32} + \frac{3\gamma}{8d^2}$$

Equation 4.6

Where  $\gamma$  represents one of three Cosserat twist moduli ( $\alpha, \beta, \gamma$ ).

Consider the situation shown in Figure 4.4 below for a classical elastic normal cantilever beam:

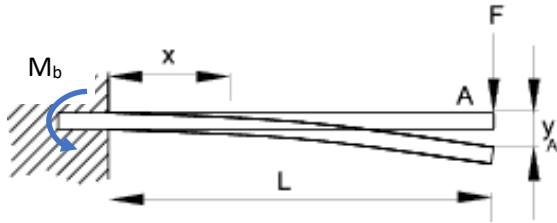


Figure 4.4: Cantilever bending

In this case, the shear force in the material ( $V$ ) is given by  $V = F$ , whilst the bending moment is:

$$M_b = M - Vx$$

$$M_b = FL - Vx$$

$$M_b = F(L - x)$$

The strain energy in the material in this case is given by:

$$U = \int \frac{M_b^2}{2EI} dx$$

Where  $I$  is the second moment of area of the cross-section.

$$U = \int_0^L \frac{[F(l - x)]^2}{2EI} dx$$

$$U = \frac{F^2}{2EI} \int_0^L (l - x)^2 dx$$

$$U = \frac{F^2}{2EI} \int_0^L x^2 - 2lx + l^2 dx$$

$$U = \frac{F^2}{2EI} \left[ \frac{x^3}{3} - \frac{2lx^2}{2} + l^2x \right]_0^L$$

$$U = \frac{F^2}{2EI} \left[ \frac{L^3}{3} \right]$$

$$U = \frac{F^2 L^3}{6EI}$$

We also know that the strain energy in the material must be equal to the energy exerted to bend the material. This means:

$$U = \frac{1}{2} F y_A = \frac{F^2 L^3}{6EI}$$

$$y_A = \frac{FL^3}{3EI}$$

$$E = \frac{FL^3}{3y_A I} \text{ but } F = \frac{2U}{y_A}$$

$$E = \frac{2UL^3}{3y_A^2 I}$$

Now the apparent stiffness in bending is given by  $k = \frac{F}{y_A} = \frac{2U}{y_A^2}$ , thus:

$$E = \frac{kL^3}{3I}$$

Now,  $L = 2d$  and  $I = \frac{d^4}{12}$

$$E = \frac{(8)(12)kd^3}{3d^4}$$

$$E = \frac{32k}{d}$$

$$\frac{k}{d} = \frac{E}{32}$$

*Equation 4.7*

This means that the apparent Young's modulus is directly proportional to  $\frac{k}{d}$ .

Since  $\frac{k}{d}$  is also related to the geometry of the material ( $d$ ), it can be noted that the apparent stiffness of the material is expected to change as the size of the sample is varied (even if the same aspect ratio is maintained). It can be noted that  $\frac{E}{32} = \frac{k}{d} = \frac{(\lambda+2\mu+\kappa)}{32} + \frac{3\gamma}{8d^2}$  in this case, thus the apparent stiffness is inversely related to the size of the sample meaning that as the sample grows smaller ( $d \rightarrow 0$ ), Micropolar theory predicts a stiffening effect. As the size of the sample gets larger ( $d \rightarrow \infty$ ), the sample would tend to exhibit a lower stiffness such that  $\frac{k}{d} \rightarrow \frac{(\lambda+2\mu+\kappa)}{32}$  meaning that as the sample grow larger, the stiffness would also tend towards a constant  $\left(\frac{E}{32}\right)$ .

### 4.3 – Summary

Within this section, a mathematical description of micropolar materials under three different loading conditions has been provided as specified in Section 4.2. These mathematical derivations also provide insight into the characterisation of size-effect behaviour in micropolar materials by relating the micro-scale properties to the macro-scale properties. This is done by comparison of classical elastic theory with micropolar theory so that the micro-scale behaviour can be depicted in terms of the macro-scale behaviour, eventually giving a complete description of the size effect behaviour in micropolar materials. It is also important to note that in the case of compression, no size effect behaviour is predicted and that the predicted stiffness is proportional to the Young's modulus. On the other hand, for bending and torsion, the stiffness predicted by micropolar theory is related to the material properties ( $E$  and  $G$ ) respectively together with the length scale parameter ( $d$ ). This means that the stiffness is always predicted to be higher than continuum theory. However, it can also be noticed that as the size of the sample becomes larger ( $d \rightarrow \infty$ ) micropolar theory predictions would converge toward continuum theories.

## 5 Obtaining a model of Bovine $\mu$ CT samples

### 5.1 – Introduction

Obtaining a 3D geometric model of cancellous bone was of critical importance in this study since finite element simulation of the trabeculae to characterise behaviour on the micro-scale cannot be done without first understanding how cancellous bone behaves on a microstructural level in terms of stress characterisation. The sample that was used in this study was obtained from a bovine cadaver by cutting through the distal epiphysis of the femur and this chapter provides an overview of the methods used to obtain the geometric model for finite element simulation.

### 5.2 - $\mu$ CT Scanning of a Bovine Distal Femur

#### 5.2.1 – Sample preparation

A bovine femur that had been stored in the laboratory freezer at  $-20^{\circ}\text{C}$  was taken out of storage and a section of the distal epiphysis was cut using a blade. The section cut was of dimensions 10mm x 10mm x 40mm. It was ensured that when cutting epiphyseal region, no sections of cortical bone or bone marrow were obtained. This was done by first, cutting two transverse sections from the whole bone that were 40mm apart and exposing both the cortical bone sections and the bone marrow. Consequently, a section of dimensions 10mmx10mm was cut from the sample while taking care to avoid the cortical bone and bone marrow regions. The excised sample (now having dimensions of 10mm x 10mm x 40mm) was stored again at  $-20^{\circ}\text{C}$  for a period of 24 hours since the required scanner was unavailable for use on the day.

#### 5.2.2 - $\mu$ CT Scanning

The  $\mu$ CT scanner used in this study was a Skyscan 1172 scanner by Bruker. The system works using an X-ray source and receiver. It is capable of using the shadow transmission images of an object that is a set distance away from the X-ray source and receiver (in this case cancellous bone). The scanner obtains the shadow transmission images of the object from different angles since the object rotates during while the scan is taking place. The obtained shadow transmission images are then converted into a slice-by-slice reconstruction of cross-sectional images of the sample by using a Feldkamp cone-beam algorithm. After further processing, these cross-sectional images can then be converted into a full 3D model of the sample, thus obtaining a full 3D geometrical model of the sample's microstructure.

The excised sample was taken out of storage and placed securely in the scanner. After the scanner was closed, the scanning parameters were set. The scanner was set to rotate the sample by only half a revolution (180°) rather than a full revolution (360°). This decision was made because cancellous bone is very porous, and the X-rays emitted by the X-ray source have the capability of penetrating through the whole sample and can also be detected by the receiver after doing so. This means that the geometry of the whole cross-section can be obtained by only rotating half a revolution. In turn, by scanning through a whole revolution of the sample, the amount of data that needs to be processed would be essentially doubled for without having any extra benefit in terms of accuracy. Thus, a need for more computational power would arise during further processing of the image to obtain the 3D model. Another disadvantage of carrying out a full evolution scan in this case would also be that the sample is exposed to double the amount of X-ray radiation and such an exposure might in turn damage the microstructure of the sample thus also affecting accuracy of the 3D model representation in this case.

The resolution of the obtained image was set to 2.09µm and the camera used had a voxel size (pixel size) of 8.99µm. Since the scanner is not capable of obtaining such high resolution through using hardware alone, this low resolution was obtained by using the zoom feature that the scanner is capable of utilising. It is important to note that various studies dealing with µCT scanning of trabecular bone have been done prior to this study and within such studies a resolution of 14µm is normally used. Such a resolution has been repeatedly shown to provide an accurate enough dataset of the 3D morphological parameters of trabecular bone. (Müller et al., 1997; Peyrin et al., 1998) In this case, a lower resolution was used because the orientation and structure of each individual trabecula in cancellous bone is of interest in terms of stress response and may have an impact on the size effect behaviour on the macro-scale. As such, obtaining a more accurate representation of the geometrical structure of each trabecula within the volume of interest was deemed to have higher importance when scanning, rather than merely obtaining 3D morphological parameters. It has been further shown that using a lower resolution does not adversely impact the accuracy of morphological analysis while in turn also causing a requirement for more computational power. (Peyrin et al., 1998)

Compensation of difference in the offset of images was also set to active since the sample was rotating (not static) in the µCT scanner. Compensation difference was activated as this helps in getting an image of the full revolution a with enhanced image clarity, which in turn would be useful in determining the geometric structure of the individual trabeculae within the sample/.

An Al+Cu filter was used to reduce the exposure of the sample to excess X-ray radiation that may have caused damage to the microstructure of the sample. Such a filter also helps in reducing beam hardening artefacts and eventually helps with obtaining images of better quality. Beam hardening correction was set to 70% so that any X-rays that may have been too intense for the sample would be automatically compensated for by the scanner itself. After the sample was scanned, a complete shadow image of the microstructure was obtained, together with a series of cross-sectional images. These cross-sectional images were further processed using the software provided with the system (*NRecon* and *CTAn*) so that a 3D model could be generated.

### 5.3 – Reconstruction

Reconstruction of the previously obtained shadow transmission images was carried out by using NRecon. This a software that is provided by Bruker together with the  $\mu$ CT scanner and can be used

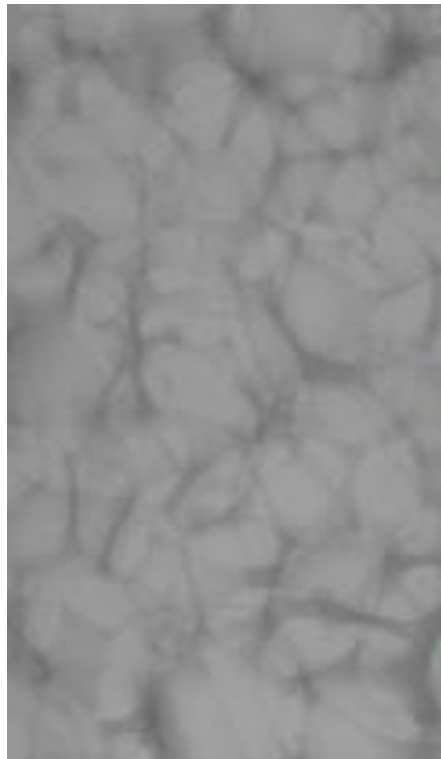


*Figure 5.1: Shadow Transmission Images obtained from the scan*

to obtain images of better quality. Reconstruction was carried out by opening the shadow transmission images (shown in Figure 5.1) obtained during the scan using NRecon and setting the reconstruction parameters as specified in the following sections.

### 5.3.1 – Region of Interest

After opening the shadow transmission images in NRecon, the first reconstruction parameter that was set was the region of interest. The region of interest can be defined as the region within the whole scan that is to be analysed. In this case, the region of interest was set to encompass the maximum range allowable within the software so that the largest possible volume is set to be available for further processing and for more sampling possibilities from the single large sample that was taken.

### 5.3.2 – Smoothing

The level of smoothing was set to the maximum as this would eventually help in creating a viable mesh that would lead to convergence in the finite element modelling phase due to negative Jacobians when loading the model. In such computations, if the image is not smooth enough convergence may not be reached or a mesh may not be capable of being created in the first place. On the other hand, this may lead to overly smoothing the model and thus some stress concentrations that occur within the model can be overlooked. This was however a necessary step to obtain a 3D mesh that could eventually be loaded with forced and boundary conditions.

### 5.3.3 – Misalignment Compensation

Since the object was rotating within the scanner during the scan. The object needs to be geometrically aligned with the machine spatial axes and with the rotation axis. When scanning at such a high resolution (on the micro-scale), any slight misalignment in axes, the X-ray source or the X-ray detector may cause defects that cause continuous lines to be interrupted and/or displaced. Misalignment compensation is capable of fixing such defects within the model. In the case of this scan, misalignment compensation was set to 11. This value was obtained by trying different values and visually inspecting the model using the preview feature (Figure 6.1) within NRecon to establish which setting would be the ideal value. The optimal value is the value that provides boundaries that are in focus (i.e. minimal amount of displaced or non-continuous edges) within the preview image.



Figure 5.2: Image preview used for setting the level of misalignment

#### 5.3.4 – Ring Artefact Reduction

Ring artefacts in the model can arise from two main causes: singular isolated defects or calibration issues in the X-ray detector elements. Ring artefacts cause concentric circles to appear in the reconstructed image slices. Ring artefacts can be reduced in NRecon using the ring artefact reduction function. However, they cannot be corrected completely. Thus, even after ring artifact reduction, these artifacts can have an effect in further post-processing.

The settings for ring artefact reduction were set to the maximum as these would give the most accurate and defect-free representation of the reconstructed image slices.

#### 5.3.5 – Beam Hardening Correction

Another artefact that can appear during a  $\mu$ CT scan is beam hardening. This artefact causes a shift of the energy spectrum of the X-rays introduced by the scanned sample. Beam hardening appears as an area that is lighter than the rest of the sample and it appear to have a stronger effect for denser sample materials. Beam hardening can be defined as a decrease of grey values inside a homogeneous phase. A low source voltage can also lead to high beam hardening artefacts. Such artefacts can be corrected in NRecon. However, such corrections have the effect of flattening the grey value profile of the image slices. In this study, the individual grey values are not of high interest since obtaining a high contrast image is more helpful in in obtaining a geometrical model that is of higher accuracy. The grey value data is not being used in any way in this study, so the flattening of the grey value profile does not affect any data that is relevant to the study itself. For this reason, the setting for beam hardening correction was set to the maximum possible in NRecon as this would provide the most contrast within the image and thus would result in the most geometrically clean and accurate representation of the sample as a 3D model.

After the settings for reconstruction were set, these were tested using the *preview* function in the *start* tab. This was done to ensure that an image of highest possible quality is obtained. By using this function, a single slice reconstructed with the selected settings is displayed and image quality can be ascertained. Upon confirmation that the image quality was good enough, reconstruction was started from within the *start* tab.

Reconstruction of the whole model is highly dependent on the image processing capability of the hardware being used. For this reason, a dedicated system was used that is found in the Technology and Innovation Centre at the University of Strathclyde. Reconstruction of the  $\mu$ CT scan took around a week.

## 5.4 – Image Processing and Analysis

Upon completion of the reconstruction process, the reconstructed image slices were processed using another dedicated software by Bruker called CTAn. The main functions of this software were to process and analyse the  $\mu$ CT scan while obtaining critical data; to further enhance image quality and reduce image size for faster processing. This was important for the creation of a 3D model that could be further processed for importing into finite element software and used for finite element analysis (FEA).

### 5.4.1 – Thresholding

The thresholding plug-in was used to generate a binary image from a set of grayscale image values that are obtained from the scan. This plug-in works by setting thresholds at which the grayscale values are considered solid (white) or voids (black). The plug-in was set to use the Ridler-Calvard method (default at the global level), and the threshold levels were set to 35 and 255 for the low and high values respectively. These values were obtained by using the binary thresholding view in the program and optimising the upper and lower thresholds until an image with a minimal number of floating spots/particles could be observed. It was assumed that these particles are noise that was captured in the image although it cannot be ascertained what the exact geometry of the sample was. These floating spots/particles had to be removed for the purpose of obtaining a viable mesh that could also be used for finite element analysis.

### 5.4.2 – Despeckling

Despeckling of the 2D binarized images is a step that is needed to remove unwanted particles that may have been detected during the scan and are not part of the model. This processing step was split into two phases; first stage despeckling, and second stage despeckling. The first stage of despeckling was carried out so that any black speckles in the solid areas of the image are removed and replaced by white areas. This means that any voids in the individual trabeculae that are captured due to image artefacts and/or noise are removed using this operation. However, there is a possibility that these points may actually be present in the structure, and it cannot be ascertained whether these points exist or not. As in previous cases, this operation was once again deemed essential so that a viable mesh could be obtained from the model. This stage was carried out by using the despeckle plug-in in CTAn and this operation was carried out as an algorithm acting on a 3D space rather than a 2D space as in the case of thresholding. This was done since carrying out

despeckling operations as a 3D operation is more accurate in terms of image processing. The only downside to this kind of setting is the increase in computational power required. However, in this case, dedicated hardware was available and thus such an operation could be carried out efficiently. The plug-in was set so that any voids in the trabecular region that are smaller than ten voxels in size are automatically removed and replaced by white areas that also represent a solid in the binary image. The first stage of despeckling returned an image with no voids in the individual trabeculae, however, there were also cases where white speckles (interpreted as solids) were captured due to artefacts and noise. Such artefacts were removed by carrying out another despeckling function which in this case is referred to as the second stage of despeckling. In this case the same plug-in was set to remove any white speckles that do not form part of the main body of the trabeculae. This was done by carrying out a 3D sweep despeckling operation which removes all objects that do not form part of the largest object.

#### 5.4.3 – Morphometric Analysis

After pre-processing the images, 3D morphometric analysis was carried out using CTAn. This type of analysis provided information on bone parameters such as the trabecular thickness, trabecular length and bone volume fraction amongst others and was carried out using an integrated plugin within CTAn; the 3D morphometric Analysis plugin. This plugin works by using a sphere fitting algorithm to the 3D model that is imported in CTAn. Based on the dimensions of these spheres it is then capable of calculating mean values for critical parameters together with providing statistic information about such parameters such as the standard deviation. A summary of this data is found in Table 5.1 together with the distributions for trabecular thickness and trabecular separation in Figure 5.3 and Figure 5.4 respectively.

<u>Description</u>	<u>Abbreviation</u>	<u>Value</u>	<u>Unit</u>
Tissue volume	TV	4.91895E+12	$\mu m^3$
Bone volume	BV	5.72838E+11	$\mu m^3$
Percent bone volume	BV/TV	0.1164553	
Tissue surface	TS	1748638839	$\mu m^2$
Bone surface	BS	17088629941	$\mu m^2$
Bone surface / volume ratio	BS/BV	0.029831343	$\mu m^{-1}$
Bone surface density	BS/TV	0.003474003	$\mu m^{-1}$
Trabecular pattern factor	Tb.Pf	0.021487306	$\mu m^{-1}$

Trabecular thickness	Tb.Th	158.8720338	$\mu m$
Trabecular number	Tb.N	0.000733198	$\mu m^{-1}$
Trabecular separation	Tb.Sp	1353.44745	$\mu m$

Table 5.1: Summary of 3D Morphometric Analysis in CTAn

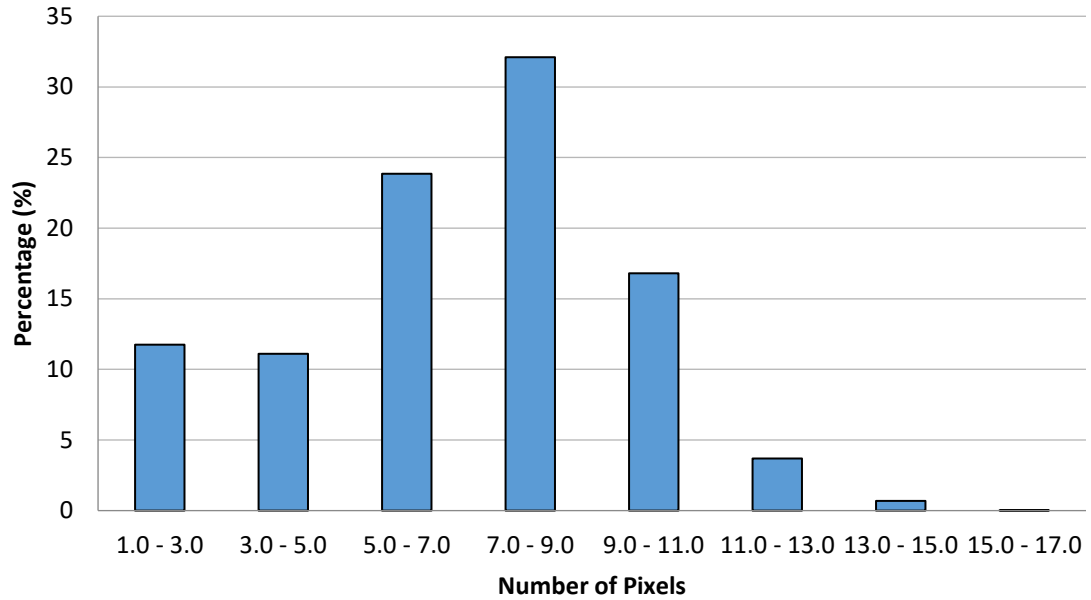


Figure 5.3: Distribution of Trabecular Thickness within the scanned sample

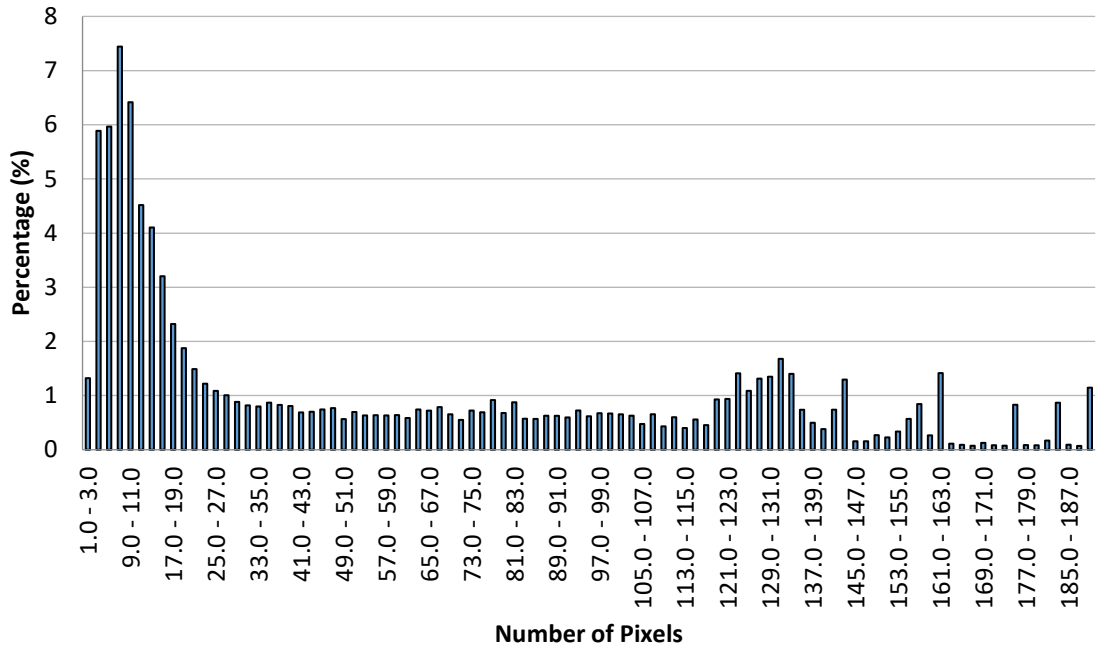


Figure 5.4: Distribution of Trabecular Separation within the scanned sample

It is important to note that in many cases, the use of such a sphere fitting algorithm may not be very accurate in obtaining morphological information of trabecular bone since there are cases where trabecular bone is modelled using rod and plate models. In this case, the trabecular separation and trabecular thickness are the most critical parameters as these, together with the bone volume fraction will be used to create computer-generated models of trabecular bone. It has been shown that only minor differences were found between two types of software; CTAn and IPL by Scanco Medical in terms of BV/TV, Tb.Sp, and Tb.Th and as such, this sphere fitting method was deemed as accurate enough in this case. The reason for this is because IPL by Scanco Medical generates the 3D morphological parameters by calculating local values rather than a sphere fitting algorithm and only minor differences were found in the mentioned parameters between both softwares used. (Mys et al., 2021)

#### 5.4.4 – 3D model generation

After pre-processing the images, the final step was to generate a 3D image from the different slices that were obtained from the scan and modified. This was done by once again using an internal plug-in CTAn. The plug-in was set to generate a 3D file in STL format using adaptive rendering with a locality

of 5, tolerance of 0.05 and with active smoothing. The units were also set to mm as this would make processing in other software simpler.

The adaptive rendering algorithm is an algorithm developed by Bruker and was designed to create 3D models that have highly realistic and smooth surfaces. Since this 3D model will eventually be imported into finite element software, it was decided that this algorithm would be the optimal one to be chosen. The locality, and tolerance settings were left as default and smoothing was turned on so that surfaces would be further smoothed. This reduces the possibility of unrealistic stress concentrations when modelling using finite element software. The files were exported in STL, ASCII format as this is one of the most common file formats and most finite element software and CAD software is compatible with such formats.

### 5.5 – 3D model manipulation

After the 3D model of the whole bovine sample was obtained in STL format, the model was to split into various smaller samples with sizes based on the trabecular length of the sample as specified earlier. Table 5.2 below gives an indication of the sample sizes in terms of the trabecular length ( $d$ ) that were used together with the number of samples taken for each size. The trabecular length and trabecular thickness were obtained from the 3D morphometric analysis that was done in the prior step. It was found that the bovine sample had a trabecular length ( $D$ ) of  $1353.45\mu\text{m}$  and a trabecular thickness of  $158.87\mu\text{m}$ . These values are on the same scale as those found in literature. Although these values are not in the same range described in literature, one must take into account that the samples in this study are bovine samples rather than human samples. As such, knowing that the scale of these parameters is on the same level is enough to provide an indication that the scan was relatively accurate. (Bakar et al., 2019)

Size	Number of samples
$2D \times 2D \times 4D$	10
$3D \times 3D \times 6D$	10
$4D \times 4D \times 8D$	10
$5D \times 5D \times 10D$	10

Table 5.2: The number of bovine samples tested using finite element analysis (FEA) for each size

The program 3-Matic by Mimics was used to split the large image obtained into smaller samples according to the trabecular length. This was done by creating cuboids of different sizes, at different locations according to the dimensions specified in Table 5.2 and using Boolean

operations to intersect the 3D model of bone with the created cuboids. This led to the creation of 40 3D models of trabecular bone having different morphologies due to the different location of each created cuboid and different sizes according to Table 5.2.

It is important to note that despite having been processed in CTAn during the preprocessing stage, the images exported from 3-Matic in the previous step were still unsuitable for use in finite element analysis (FEA) software. This because there existed some small particles that had been captured during the scanning process but were not eliminated during the filtering and despeckling processes in CTAn. Such particles prevent the running of finite element simulations to proceed smoothly as they are registered as unattached bodies which would eventually prevent convergence of the finite element simulation. To eliminate these small particles, an open-source software; FreeCAD was used together with the 'Remove Components' function. This provided various STL files of different sizes that all consisted of one body. However, STL files are considered to be a surface mesh, and a further processing was needed to convert the surface meshes into solid meshes that could be used for Finite Element Analysis.

The conversion from a surface mesh to a solid mesh was done using 3-Matic. This was done importing each model and carrying out an 'Auto-Remesh' for each. After this, the 'Fix Wizard' was used to repair any defects within the mesh such as holes and flipped normal amongst others. After this, sharp triangles, small edges, and small shells were filtered out of the model and a smoothing operation was also carried out. All these steps were done to reduce model size and the eventual number of solid elements that would be generated as this also affects the demand for computational power. After carrying out all these operations, a volume mesh was created using 3-Matic and it was set to use the 'Init and Refine'. This algorithm automatically creates a volume mesh of the geometry and uses local mesh refinement based on the complexity of the structure. The mesh was also set to have an Aspect Ratio of 30. This value was selected so that no elements that produce errors in ANSYS would be created. The maximum edge length was also set to 0.05mm so that element size would be kept to a relatively small size. This edge length was chosen in this case because 3-Matic is capable of generating only single order solid elements and as such a relatively small element size was chosen to compensate for the fact that a second order solid element could not be used to further improve accuracy of the simulation and reduce stress concentrators.

It is important to note that the mesh created by 3-Matic in this case, had elements with an average aspect ratio below 30. However, there were always some elements that would exceed this

threshold in terms of aspect ratio. Such elements would create warnings in some cases errors in ANSYS. In the case of warnings, the analysis would still run and have a good level of accuracy since the number of warning elements would be low when compared to the total number of elements. In the case of error elements, no analysis could be run. Thus, the remeshing process would have to be restarted in 3-Matic by using the “Remesh” and “Fix Wizard” functions.

After generating the volume mesh, this was then exported to CDB format so that it could be imported into ANSYS for finite element analysis simulation.

## 6 FEA of Bovine samples

### 6.1 - Introduction

Following the generation of a 3D volume mesh, the models created had to be loaded so that the stress distribution within the model could be analysed and compared to the other models that are being tested within this thesis; mainly the computer-generated idealised models of trabecular bone. By doing this, the size effect behaviour of these models could be analysed and also compared to the computer-generated idealised models and to the experimental testing of the enlarged 3D printed samples.

### 6.2 – Methodology (ANSYS)

After the processing of the bovine samples described previously, the 3-D models in CDB format were imported into ANSYS using ANSYS Mechanical APDL. This consisted of a total of 40 models of a cuboidal shape, with constant aspect ratio and with size based on the trabecular edge length ( $d$ ) such that the sizes of the models were  $2d \times 2d \times 4d$  (10 samples),  $3d \times 3d \times 6d$  (10 samples),  $4d \times 4d \times 8d$  (10 samples), and  $5d \times 5d \times 10d$  (10 samples) as described in Section 5.7.2. All models were set to have elastic isotropic properties with Young's modulus ( $E_t$ ) 12GPa and Poisson's ration ( $\nu_t$ ) 0.3 as described by Goda et al. (2013). This was done because the elements in this case are not modelling trabecular bone as a continuum, but rather the individual trabeculae encompassing the microarchitecture of trabecular bone. Despite the fact that trabecular bone exhibits anisotropy on a macrostructural scale, on a microstructural scale it can be represented by an elastic isotropic material model to a relatively accurate degree, especially when considering that the displacements being exerted on the model are on an even smaller scale than the microstructure itself. Models were loaded in three different loading modes:

- Unconfined uniaxial compression with 0.1% maximum strain.
- Uniaxial torsion along the longitudinal axis with a maximum torsion angle of  $0.05^\circ$ .
- Cantilever bending with a maximum displacement of 0.01mm.

For each case, the overall exhibited stiffness was then calculated and different sample sizes could be compared to determine whether these samples exhibit micropolar behaviour.

For each loading mode, an APDL script was created as a TXT file and subsequently read in ANSYS so that the analysis would be carried out automatically. Each analysis was further carried out sequentially in an automatic fashion by using a batch file.

### 6.2.1 – Compression

The code that was used to load the models in unconfined uniaxial compression with a 0.1% maximum strain is shown in **APPENDIX 1** together with descriptions of the commands added as comments.

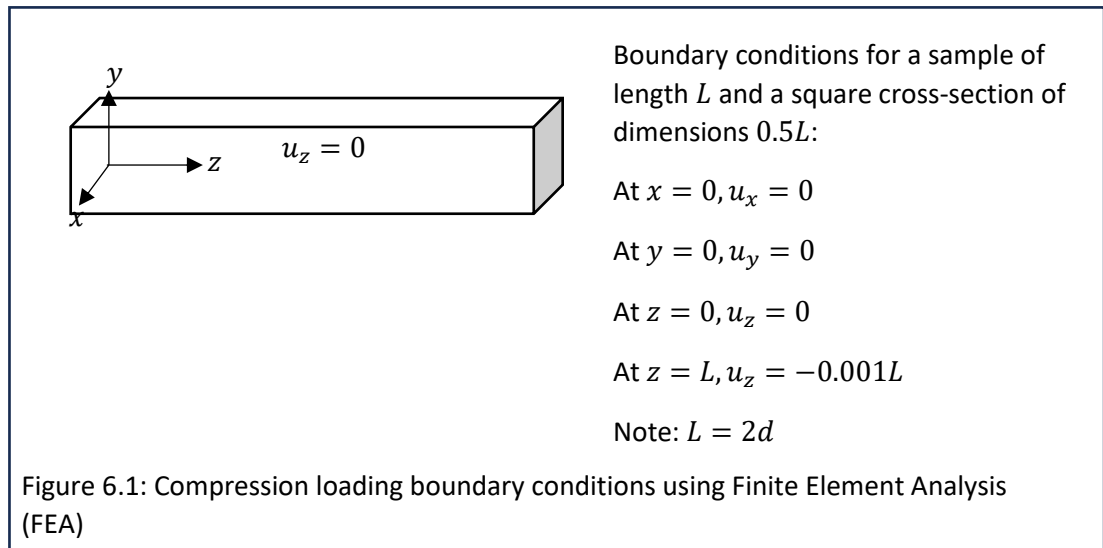
The process of loading the 3D mesh in compression was as follows:

First, the 3D mesh was imported to ANSYS Mechanical APDL and the pre-processing stage is entered. After this, the total length of the model is defined as a constant and the maximal/minimal positions in the three axial locations are found. These are then stored as named variables as they will be used to define node selections by location for the application of boundary conditions. Further to this, the highest node number was also obtained and stored as a named variable. This was done so that nodes that need to be created further on for the creation of loads and boundary conditions can be numbered cumulatively according to this number.

Any material properties that might have been imported with the mesh (these are defined as the default values assigned by CTAn upon mesh creation and need to be deleted so that new material models and properties can be assigned) were then deleted and a linear isotropic elastic material having a Young's modulus of 12GPa and a Poisson's ratio of 0.3 was assigned (Note: The Young's modulus defined within these material properties is the Young's modulus of each individual trabecula ( $E_{trab}$ ) and not the overall exhibited Young's modulus on the macroscopic scale).

After this, the nodes at one side of the model were selected using the maximal/minimal position obtained earlier and boundary conditions were set to prevent motion in the axial direction perpendicular to the face. The nodes on the opposite face of the model were then selected and a displacement resulting in 0.1% compressive strain.

Nodes on one of either of the other sides of the model were also constrained so that they could not move in the direction perpendicular to the face so that the model would be fixed in place and no sliding could occur. This resulted in the model being loaded as shown in Figure 6.1 below.



The simulation was run and a solution was subsequently obtained. After this, the strain energy in each element within every model was obtained and the sum of these was computed for every finite element simulation. By using this method, the total strain energy in each model was obtained. This was then used to calculate the overall exhibited stiffness in the model and correlate it to the overall exhibited Young's modulus of the sample as described in Chapter 4. Average results for each extracted model are shown in Figure 6.5 (section 6.3.1). With error bars indicating the standard error.

### 6.2.2 – Bending

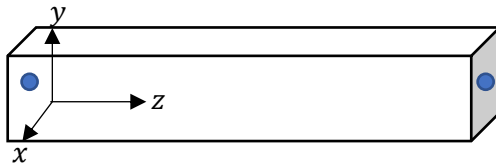
The code that was used to load the models in cantilever bending was also similar to the code used for the unconfined compression and uniaxial torsion described above as can be noted in **APPENDIX 2**.

Importation of the geometry into ANSYS and assignment of the material properties was carried out in the same method used for compression in Chapter 6.2.1.

A mass element was then defined in the simulation so that this could be used as a master node to apply boundary conditions. Subsequently two master nodes were created at the centre of the fixed and loaded faces respectively.

After this, the nodes at the fixed side of the model were selected using the maximal/minimal position obtained earlier and constraint equations were created to the mass element on this same face (acting as a master node. In this case, the  $x$ -,  $y$ -, and  $z$ -displacements were tied to those of the master node. The displacements and rotations of the master node were eventually all set to zero when applying boundary conditions to the model since this is the fixed face.

The nodes at the loaded side of the model were selected using the maximal/minimal position obtained earlier and constraint equations were created to the mass element on this same face (acting as a master node. In this case, only the  $y$ -displacements were tied to those of the master node whilst the other degrees of freedom are left free. This because when applying cantilever bending, the nodes should be allowed to move freely in the  $x$ - and  $z$ - directions when a fixed  $y$ -displacement is applied as described in Figure 6.2. A displacement in the  $y$ -direction was then applied to the master node. This means that the model will be subjected to cantilever bending as described by Figure 6.2.



Boundary conditions for a sample of length  $L$  and a square cross-section of dimensions  $0.5L$ :

At  $z = 0$ ;

- Master node at coordinates  $(0.25L, 0.25L, 0)$  linking  $u_x, u_y, u_z$  to slave nodes at  $z = 0$
- $u_x, u_y, u_z(\text{master node}) = 0\text{mm}$

At  $z = L$ ;

- Master node node at coordinates  $(0.25L, 0.25L, L)$  linking  $u_y$  to slave nodes at  $z = L$

Figure 6.2: Cantilever bending boundary conditions using Finite Element Analysis (FEA). (Boundary conditions in blue represent the master nodes while those in black represent the slave nodes).

Similarly to Chapter 6.2.1, the simulation was run and a solution was obtained. The strain energy within the whole model was obtained and the overall exhibited stiffness was calculated as described

in Chapter 4. Average results for each extracted model are shown in Figure 6.7 (section 6.3.3). With error bars indicating the standard error.

### 6.2.3 – Torsion

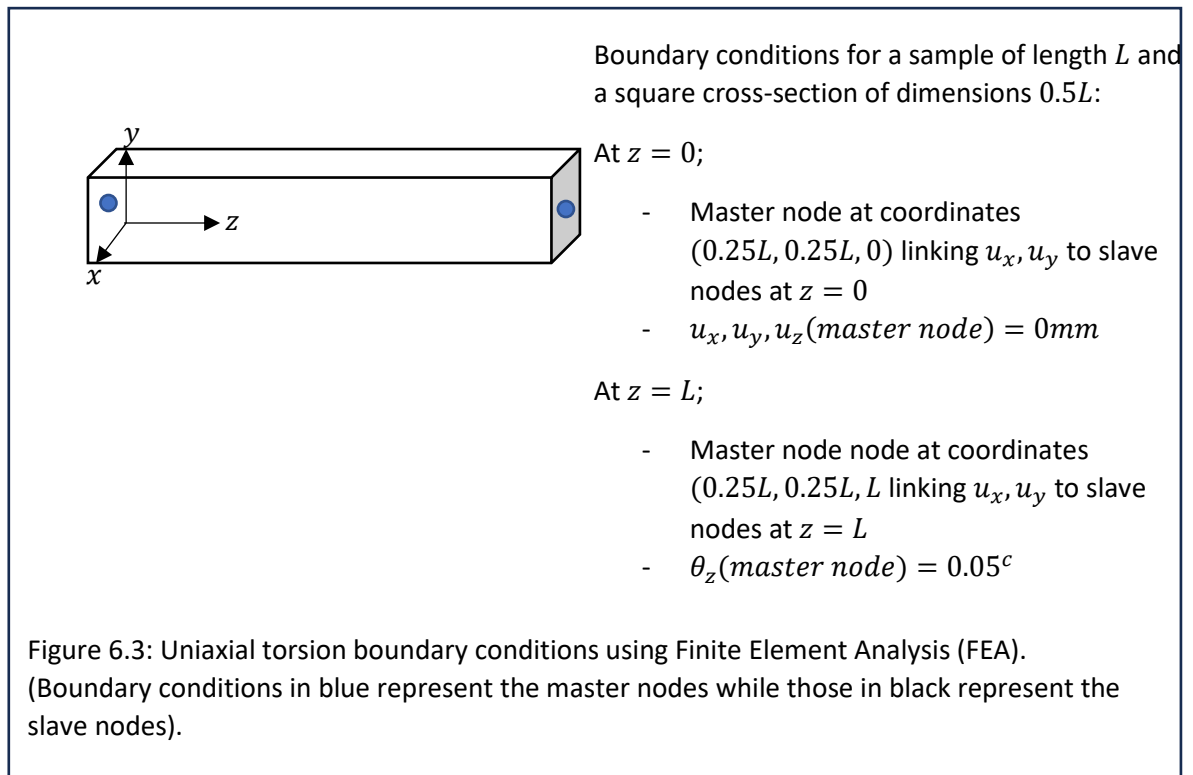
The code that was used to load the models in uniaxial torsion along the longitudinal axis with a maximum torsion angle of  $0.05^\circ$  was similar to the code used for the unconfined compression described above as can be noted in **APPENDIX 3**.

Importation of the geometry into ANSYS and assignment of the material properties was carried out in the same method used for compression and bending in Chapter 6.2.1 and Chapter 6.2.2.

A mass element was defined in the simulation so that this could be used as a master node to apply boundary conditions. Subsequently two master nodes were created at the centre of the fixed and loaded faces respectively.

After this, the nodes at the fixed side of the model were selected using the maximal/minimal position obtained earlier and constraint equations were created to the mass element on this same face (acting as a master node). In this case, only the x- and y- displacements were tied to those of the master node whilst the z-displacement is left free (so that face warping can occur). This means that the x- and y- displacements of the slave nodes will be applied such that each node within the loaded face will have a rotating motion with respect to the master node to that has been previously defined. The displacements and rotations of the master node were eventually all set to zero when applying boundary conditions to the model since this is the fixed face. This means that the face is not allowed to displace in the x- and y- directions (since these degrees of freedom are tied to the master node), whilst the face can displace in the z-direction so that warping of the face can occur.

The nodes at the loaded side of the model were selected using the maximal/minimal position obtained earlier and constraint equations were created to the mass element on this same face (acting as a master node. In this case, only the x- and y- displacements were tied to those of the master node whilst the z-displacement is left free. A rotation around the z-axis was then applied to the master node. This means that the x- and y- displacements of the slave nodes will be applied such that they create a rotation around the z-axis of the master node. Thus, the model will be twisted around its longitudinal axis, simulating the application of torque. This created the loading mode shown in Figure 6.3.



Similarly to Section 6.2.1 and Section 6.2.2, the simulation was run and a solution was obtained. The strain energy within the whole model was obtained and the overall exhibited stiffness was calculated as described in Chapter 4. Average results for each extracted model are show in Figure 6.9 With error bars indicating the standard error.

### 6.3 – Results and Discussion

#### *Normalisation of the Young's Modulus for theoretical predictions*

It is important to note that the overall exhibited Young's Modulus ( $E$ ) for the theoretical predictions was normalised by taking into account the bone volume fraction of the bone as obtained from

morphometric analysis of the scanned sample. This was done since trabecular bone has a very low bone volume fraction ratio and all theories (continuum and non-continuum) do not take this into consideration. As such, normalisation would account for the presence of voids within the microstructure of trabecular bone.

The bone volume fraction ratio (BV/TV) was found to be 11.65%. This property is also known as the ratio of bone volume to total volume. This means that the theoretical predictions for Linear Elastic, and Micropolar theory would need to be multiplied by 11.65% so that they become equivalent in terms of bone volume fraction ratio and area fraction ratio.

#### *Strain Energy calculations*

It was observed that the close proximity of elements to the edges of the model (where boundary conditions were applied) may have led to inaccuracies in the calculation of total strain energy (since the strain energy within the whole model is calculated). This because applied boundary conditions tend to create stress concentrations at the constrained elements and the area immediately surrounding the elements. The ideal scenario in this case would have been to calculate the total strain energy within a predefined central volume of each model so as to avoid areas with stress concentrations due to applied boundary conditions. However, it was also noticed that in this case, the relative number of affected elements was very low and as such, the effect that such inaccuracies would have on the overall result would be minimal.

#### *Calculation of normalised stiffness from FE results*

The finite element results provided a reading for the total strain energy calculation within the model. For each loading mode, the stiffness can be calculated using the formulae for compression, bending and torsion as described below:

$$\text{Compression: } U = \frac{1}{2}kx^2 \quad \text{Equation 6.1}$$

$$\text{Bending: } U = \frac{1}{2}ky_A^2 \quad \text{Equation 6.2}$$

$$\text{Torsion: } U = \frac{1}{2}k\phi^2 \quad \text{Equation 6.3}$$

For each case, the stiffness  $k$  was calculated and subsequently normalized to obtain values that are independent of sample dimensions as described in Section 4.2.

### 6.3.1 – Compression

Figure 6.4 depicts the stresses in the smallest analysed bovine sample. It could be noted that the larger samples all had a similar stress distribution to this. Stresses can be said to be distributed through most of the structure. Upon further examination, it can be seen that the thicker trabeculae tend to carry less stresses whilst stress concentrations occur at sharp bends within the trabeculae or within the especially thin trabeculae. This means that the thicker and smoother trabeculae within the bone tends to deform less, whilst the thinner trabeculae together with those having sharp bends

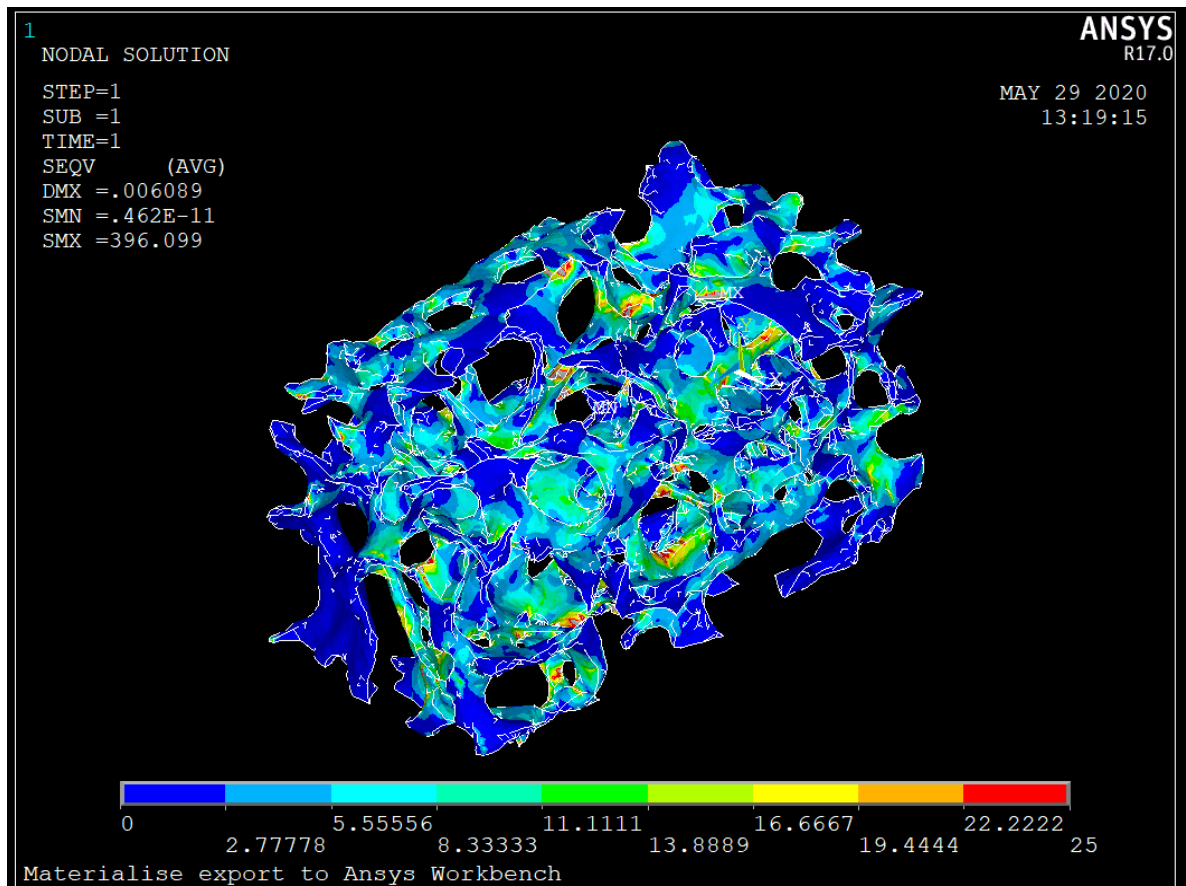


Figure 6.4: Von-Mises equivalent stresses in the smallest analysed bovine samples under compression

would tend to deform more, thus having a higher potential to yield under load. The distribution of stresses within the microstructure of trabecular bone in this case agrees with literature where compression testing of similar models have been carried out and similar patterns have been observed where local yielding occurs in the thinner trabeculae even at small strains, leading to micro-damage of the trabeculae. (Guillen et al., 2011; Sabet et al., 2017)

Results for testing of the micro-CT scanned samples in compression can be seen in Figure 6.5. The normalised stiffness  $\frac{k}{d}$  represents the stiffness  $k$  normalised by the cross-sectional edge length  $d$  and is directly proportional to the overall exhibited Young's Modulus ( $E$ ) as shown in Chapter 4. The graph shows the normalised stiffness plotted as a function of the cross-sectional edge length with error bars representing the standard error and the data points representing the average for each size of sample.

Figure 6.5 also shows the predicted behaviour from micropolar theory and classical elasticity. This prediction is based on the calculations in Section 4.2.1 Equation 4.1 such that the normalised stiffness  $\frac{k}{d}$  should be equal to a constant value of  $\frac{E}{2}$  with no predicted size effect behaviour as predicted by Micropolar theory.

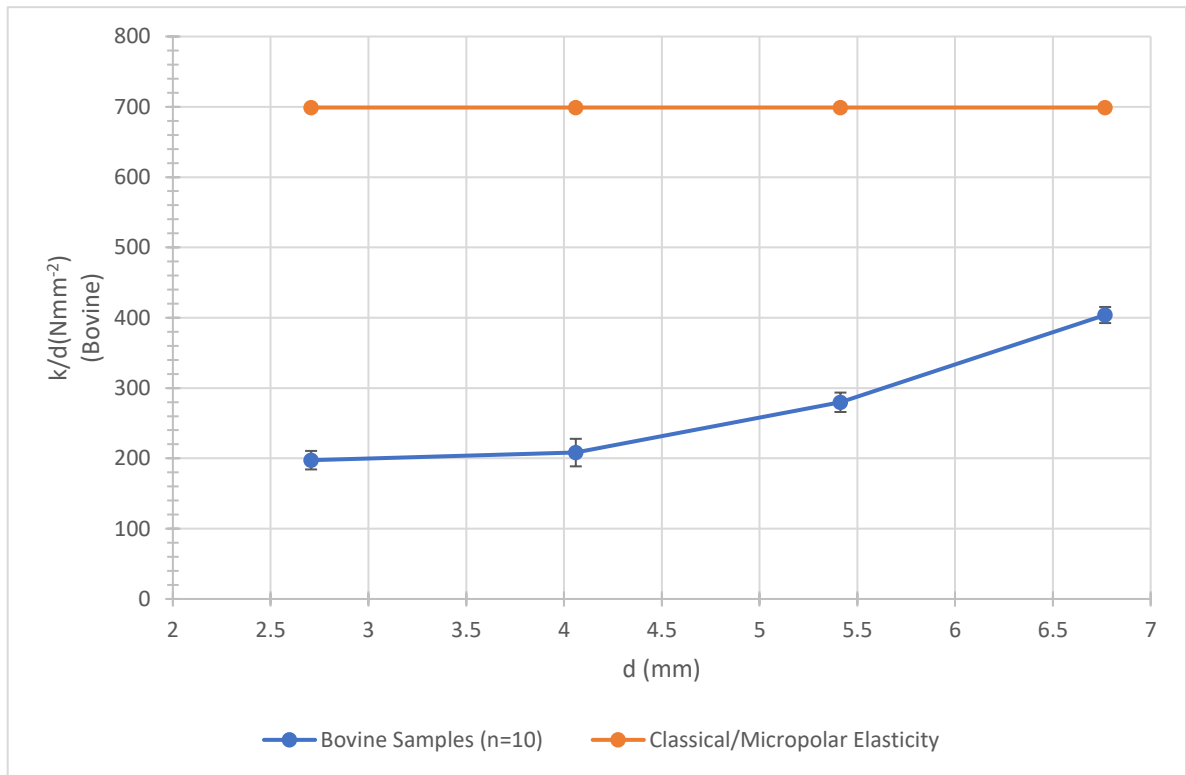


Figure 6.5: Size-effect behaviour of bovine cancellous bone under compression

Micropolar theory indicates that no size effect should be observed as the size of the sample is increased and/or decreased. As can be clearly seen from the data for finite element simulation of the scanned samples, a size effect can be observed when the samples are loaded in unconfined uniaxial compression. This size effect exhibits an increase in normalised stiffness with increasing

size of the sample. It can also be noticed that the exhibited normalised stiffness of the bovine samples is much lower than that predicted by theory. A possibility for this reduction in normalised stiffness is due to the size effect behaviour that is exhibited by trabecular bone as indicated in Figure 6.5. In fact, in this thesis, the possibility that the exhibited size effect behaviour of the sample converges towards classical elasticity as the size of the sample increases is being explored (in Chapter 9). Further to this possibility, there is also the chance that the varying trabecular thickness within the sample (bone heterogeneity) may affect the exhibited normalised stiffness together with the percentage surface area that is being loaded at the boundary conditions. Despite these two options being a possible factor affecting the size-effect behaviour of trabecular bone, Figure 6.4 does not show any evidence that the loaded percentage surface area affects the stress distribution within the material, and thus this may not be a factor that affects the exhibited normalised stiffness of the sample. On the other hand, Figure 6.4 also indicates that the thinner trabeculae tend to sustain more stress within the model and thus there is a higher possibility of yielding and micro-motions within these trabeculae. This contributes to the size-effect behaviour and exhibited normalised stiffness of the sample.

The size effect behaviour of cancellous bone exhibited in Figure 6.5 indicates that the trabecular density within the microstructure of cancellous bone affects the size effect behaviour as shown in Figure 6.5. This occurs together with the stress distribution along the trabeculae in compression as shown in Figure 6.4. As the thinner trabeculae experience more yield under compressive load, the trabecular density within the sample increases as the trabeculae are compressed in a tighter lattice within the microstructure. This subsequently leads to the stiffening effect exhibited by the bovine samples in Figure 6.4. A factor that was not taken into account when building such a model is that the material model chosen did not include the modelling of yield within the material. This may lead to inaccuracies within the model. If a material model that includes yielding had been selected, it is predicted that the micro-motions predicted by the model would be larger in magnitude (due to yielding). This would lead to an exacerbation of size-effects, making the increase in normalised stiffness increase even more as the size of the sample increases.

Micropolar and classical elasticity predict that no size effect behaviour should be observed under compressive loading. However, the yielding of the individual trabeculae leads to an exhibition of size effect behaviour which would in turn be completely unrelated to micropolar theory. As the size of the sample increases, the normalised stiffness of the sample continues to increase until the yielding of individual trabeculae no longer impacts the overall behaviour to such a large degree. This

means that if the size of the sample is increased further, there might be potential convergence towards classical/micropolar elastic theory when the bovine samples. However, further research into this would need to be carried out as in this case, the study is limited to only one large sample which was then further split into sub-samples which had very close proximity to each other within the main sample being tested. Further work would also need to be carried out to investigate the use of non-linear material models in such models to evaluate the degree to which they affect accuracy of stress field modelling and the eventual effects on size effect behaviour.

It was further noticed after analysis of these results and further inspection of simulation settings, that the boundary conditions did not accurately represent an unconfined compression test. This because the constraining of two of the longitudinal faces within the cuboidal model created a symmetric condition where a cuboid having four times the cross-sectional area was actually being modelled under unconfined compression. Such boundary conditions may also be used to simulate an interpretation of the combination of confined and unconfined compression into one model. Despite all of this, after further analysis, to determine the effect of boundary conditions on the model, it was further determine that a change in boundary conditions within the model affected the strain energy reading to a degree that is <1% of the total strain energy that was observed and in this case, it was deemed unnecessary to rerun the simulation as this would still yield similar results in terms of size effect behaviour (since the degree of difference in boundary conditions affected the results to a very minimal degree).

### 6.3.2 – Bending

Figure 6.6 depicts the stresses in the smallest analysed bovine sample. It could be noted that the larger samples all had a similar stress distribution to this. Stresses can be said to be distributed through most of the structure. Upon further examination, it can be seen that the thicker trabeculae tend to carry less stresses whilst stress concentrations occur at sharp bends within the trabeculae or within the especially thin trabeculae, similarly to what was observed in compression. This means that stress concentrations will also still tend to occur on the thinner trabeculae in the same way as

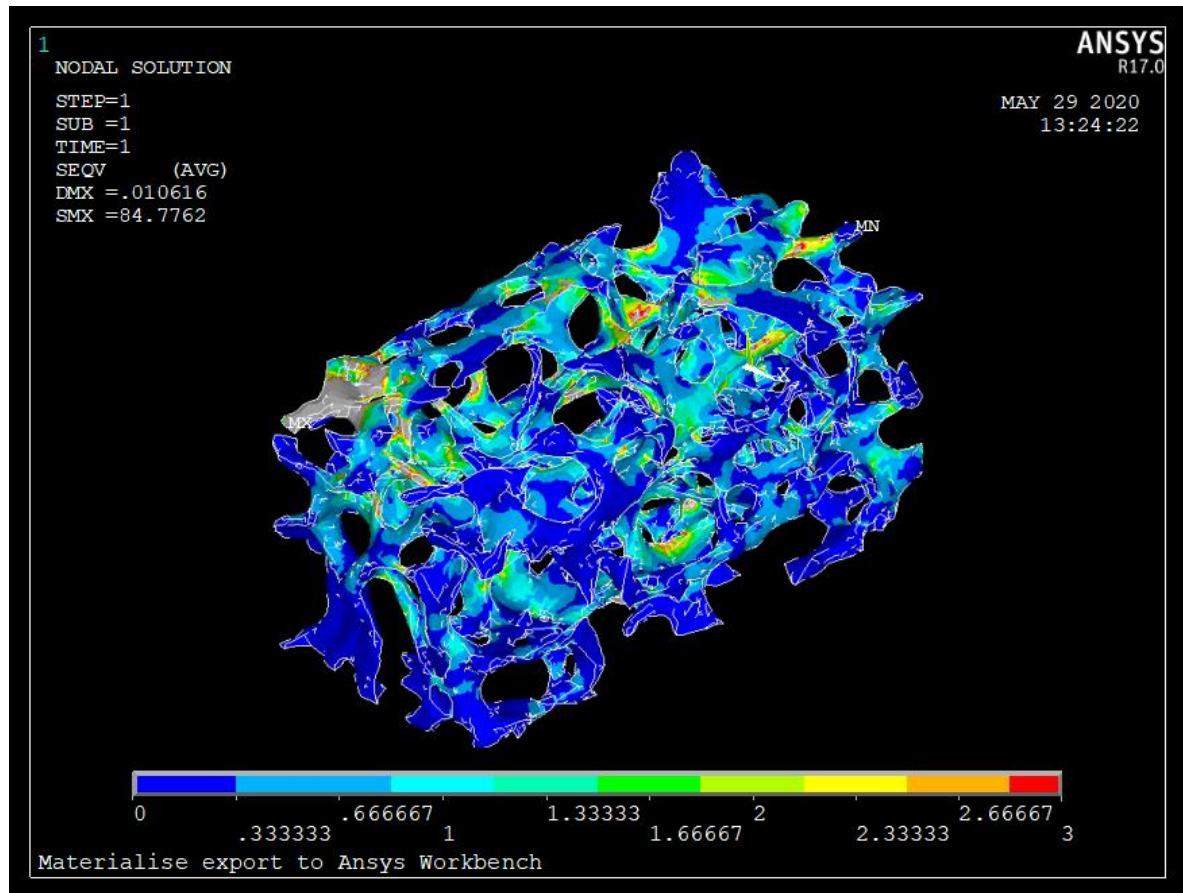


Figure 6.6: Von-Mises equivalent stresses in the smallest analysed bovine samples under cantilever bending

when the sample was loaded in compression, although they are smaller in magnitude and in some instances the locations of stress concentrations also vary from those in compression. The distribution of stresses within the microstructure of trabecular bone indicates that similarly to compression, local yielding may occur in the thinner trabeculae even at small strains, leading to micro-damage of the trabeculae. (Guillen et al., 2011; Sabet et al., 2017)

Results for testing of the micro-CT scanned samples in cantilever bending can be seen in Figure 6.7. Similarly to Section 6.3.1, the normalised stiffness  $\frac{k}{d}$  represents the stiffness  $k$  normalised by the cross-sectional edge length  $d$  and is directly proportional to the overall exhibited Young's Modulus ( $E$ ) as shown in Chapter 4. Error bars for the bovine samples represent the standard error and the data points plotted are for the mean values for each size of sample ( $n=10$ ).

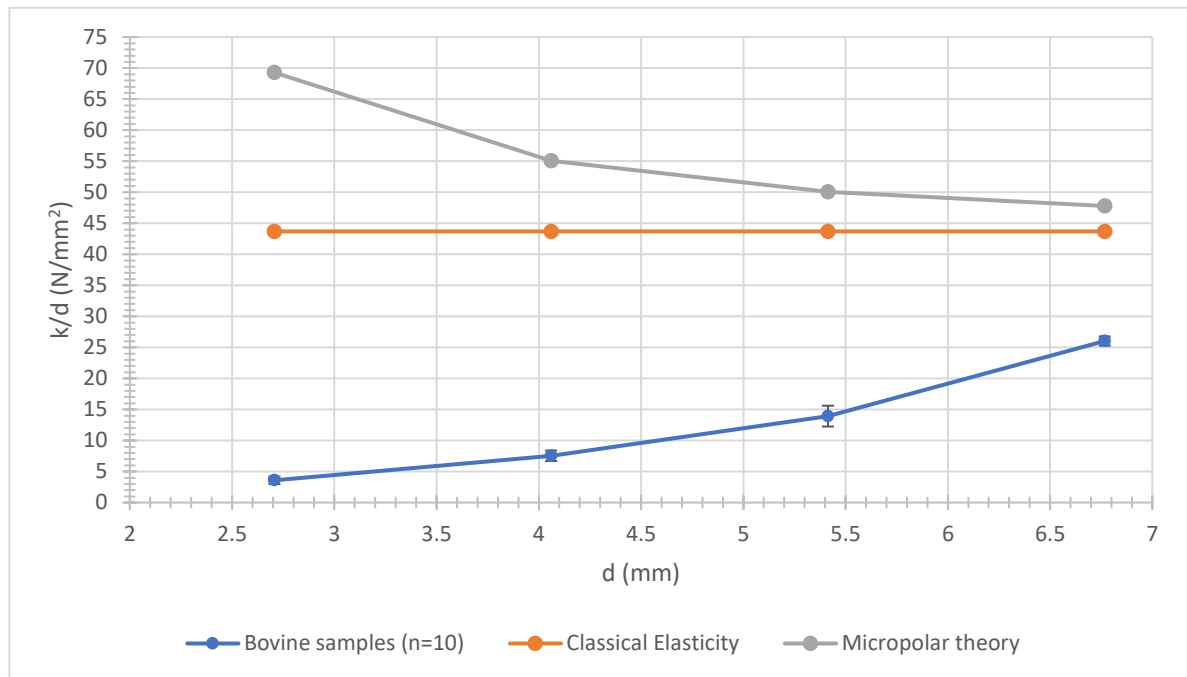


Figure 6.7: Size-effect behaviour of bovine cancellous bone under cantilever bending

Figure 6.7 also shows the predicted behaviours from micropolar theory using Equation 4.6 from Section 4.2.3 and classical elasticity. Classical elasticity indicates that no size effect should be observed as the size of the sample is increased and/or decreased. As also determined in Section 4.2.3, the normalised stiffness is specified at a value of  $\frac{k}{d} = \frac{E}{32}$ . It is important to note that this equation refers to the macro-scale material properties and not to the material properties that have been used to define characteristics of the individual trabeculae on the micro-scale to carry out finite element simulation.

On the other hand, micropolar theory indicates that the normalised stiffness should decrease as the size of the sample increases. As also determined in Section 4.2.2, the normalised stiffness converges towards classical elasticity as the size of the sample increases since it has already been shown that  $E = \lambda + 2\mu + \kappa$  for cantilever bending. The slope of the graph is determined by the Cosserat twist

modulus  $\gamma$ . For the sake of comparative reasons, the value of this modulus is not important as this graph is being used to compare the overall trend in size effect behaviour of the bovine samples with those predicted from theory. In this case, the value of the Cosserat twist modulus was given an arbitrary value of  $500\text{N/mm}^2$ . In this case, an arbitrary value was chosen since the magnitude of the Cosserat twist modulus does not affect the convergence point (asymptote value) and this only affects the slope of the curve and the overall theoretical trend in size effect behavior was of higher interest rather than the exact values in terms of material properties. Since the behavior observed by the bovine samples was completely different in terms of size effects, these values could not be determined as a material property of trabecular bone. If a similar size effect behaviour had been observed, the magnitude of the Cosserat twist modulus could have been determined for cancellous bone by using an optimisation process that minimises the sum of squared differences between the predicted behavior and the behavior analysed in real life.

As can be clearly seen from the data for finite element simulation of the scanned samples, a size effect behaviour can be observed when the samples are loaded in uniaxial torsion. This size effect exhibits an increase in normalised stiffness with increasing size of the sample. This contradicts both the predictions from classical elasticity and micropolar theory. Similar to the case of uniaxial unconfined compression, it can be said that these size effects are unrelated to micropolar behaviour and that these are observed due to the yielding together with micro-damage within the trabeculae that eventually leads to an increase in trabecular density within the sample as the trabeculae are compressed in a tighter lattice, thus leading to the size effect behaviour exhibited by the bovine samples in Figure 6.7. It can also be noticed that the rate of increase in normalised stiffness is of lower magnitude for samples that are loaded in cantilever bending when compared to the samples that are loaded in uniaxial torsion. This slower increase in stiffening rate can be attributed to a lower amount of trabeculae experiencing yield or micro-motions. This is also demonstrated in the stress magnitudes observed in Figure 6.6; such stresses are of much smaller magnitude when compared to those observed in torsion, which would in turn result in less yielding and thus a smaller exhibition of size-effect behaviour. This in turn results in a slower rate of stiffening as the size of the sample increases.

It is thus being theorised that as the size of the sample increases, a size effect behaviour similar to that observed in torsion is predicted where the normalised stiffness of the sample continues to increase until the yielding of individual trabeculae no longer impacts the overall behaviour to such a large degree. Subsequently, micropolar behaviour would start being observed within the material

which would eventually lead to a convergence of normalised stiffness towards that predicted by Classical Elasticity.

### 6.3.3 – Torsion

Figure 6.8 depicts the stresses in the smallest analysed bovine sample. It could be noted that the larger samples all had a similar stress distribution to this. Stresses can be said to be distributed through most of the structure in a similar way to compression and bending. Similarly to the other loading modes, further examination indicates that the thicker trabeculae tend to carry less stresses whilst stress concentrations occur at sharp bends within the trabeculae or within the especially thin

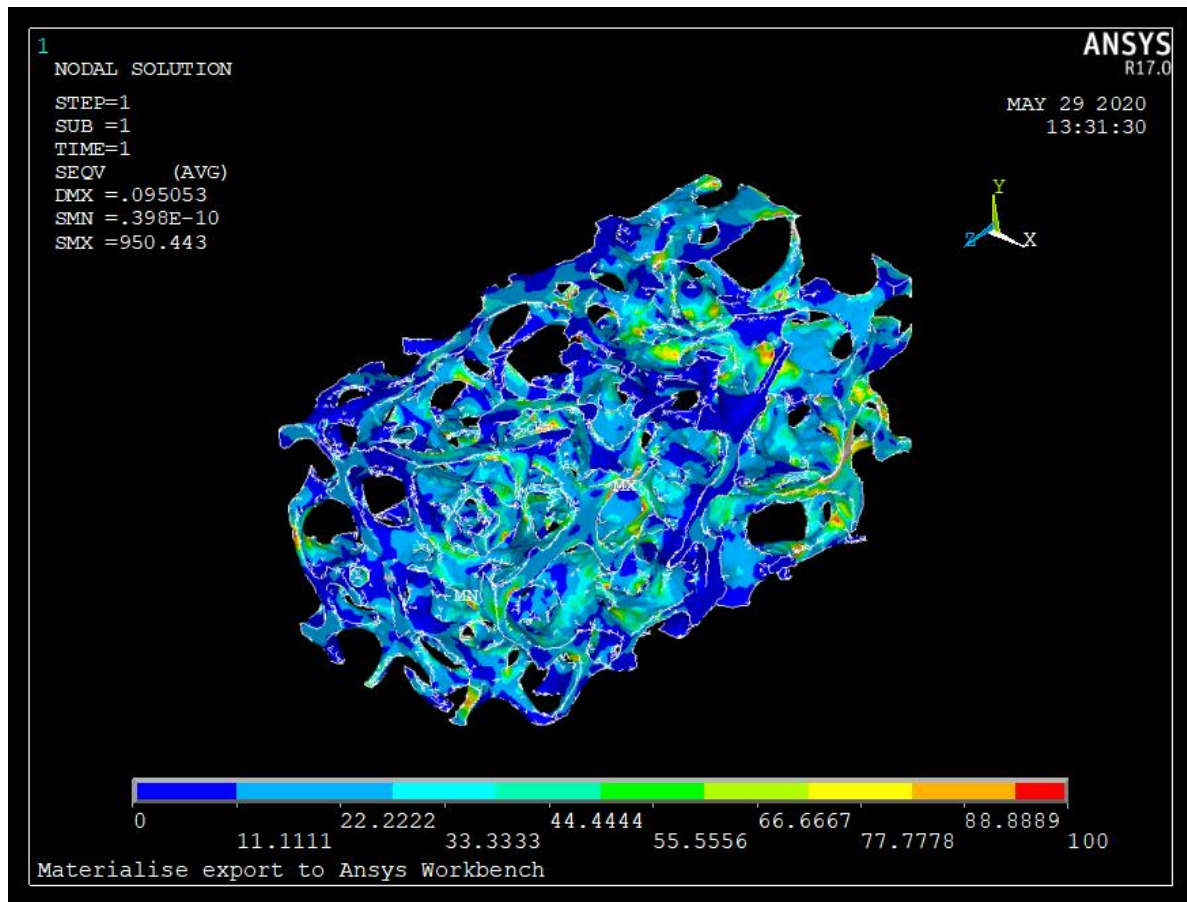


Figure 6.8: Von-Mises equivalent stresses in the smallest analysed bovine samples under torsion trabeculae.

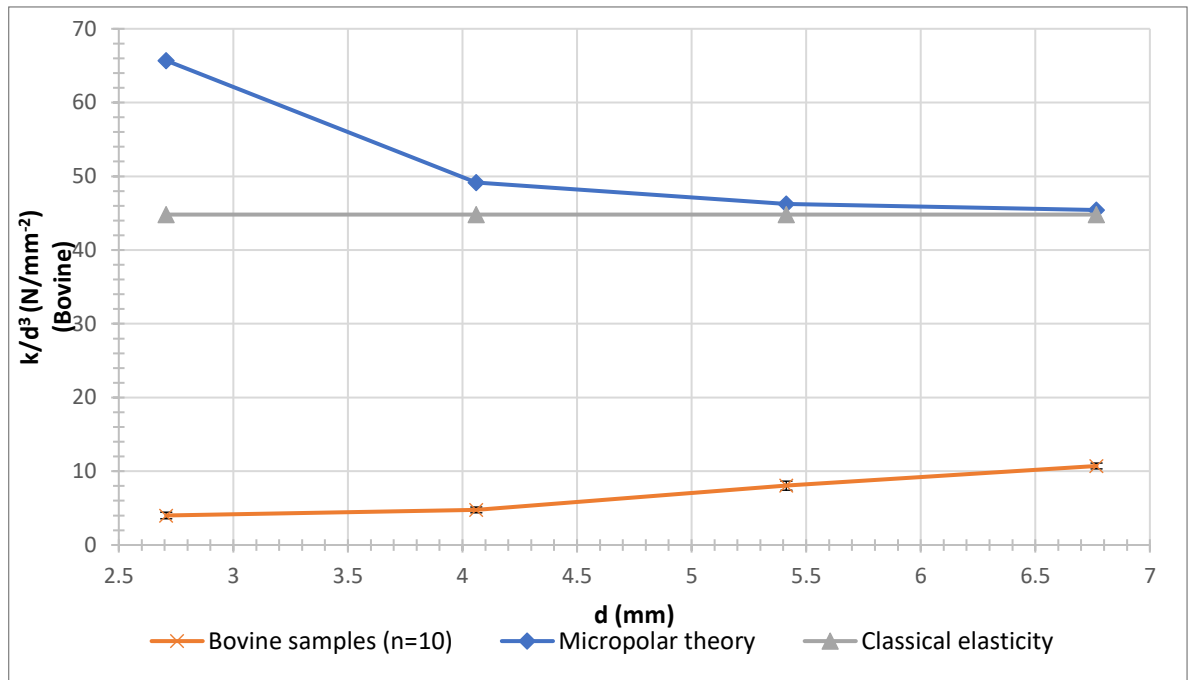


Figure 6.9: Size-effect behaviour of bovine cancellous bone under torsion

Results for testing of the micro-CT scanned samples in uniaxial torsion along the longitudinal axis can be seen in Figure 6.9. The normalised stiffness  $\frac{k_\phi}{d^3}$  represents the stiffness  $k_\phi$  normalised by the cross-sectional edge length  $d$ . The graph shows the normalised stiffness plotted as a function of the cross-sectional edge length with error bars representing the standard error and the data points representing the average for each size of sample (n=10).

Figure 6.9 also shows the predicted behaviours from micropolar theory using Equation 4.3 from Section 4.2.2 and classical elasticity. Classical elasticity indicates that no size effect should be observed as the size of the sample is increased and/or decreased. As also determined in Section 4.2.3, the normalised stiffness is specified at a value of  $\frac{k}{d^3} = \frac{G}{12}$ . Similarly to the case of loading in cantilever bending, this equation also refers to the macro-scale material properties and not to the micro-scale material properties that have been defined to carry out finite element simulation.

On the other hand, micropolar theory indicates that the normalised stiffness should decrease as the size of the sample increases. As also determined in Section 4.2.3, the normalised stiffness converges towards classical elasticity as the size of the sample increases since it has already been shown that  $\alpha = \frac{G}{12}$ . The slope of the graph is determined by the variables  $\beta$  and  $\gamma$ . For the sake of comparative reasons, these variables are not important as this graph is being used to compare the overall trend in size effect behaviour of the bovine samples with those predicted from theory. In this case, the

value of  $\beta$  and  $\gamma$  were given arbitrary values of  $1000\text{N/mm}^2$ . In this case, arbitrary values were chosen since the magnitude of these material properties does not affect the convergence point (asymptote value) and they only affect the slope of the curve and the overall theoretical trend in size effect behavior was of higher interest at this point rather than the exact values in terms of material properties. Since the behavior observed by the bovine samples was completely different in terms of size effects, these values could not be determined as a material property of trabecular bone. If a similar size effect behavior had been observed, the magnitude of the  $\beta$  and  $\gamma$  could have been determined for cancellous bone using an optimisation process that minimises the sum of squared differences between the predicted behaviour and the behaviour analysed in real life.

As can be clearly seen from the data for finite element simulation of the scanned samples, a size effect can be observed when the samples are loaded in uniaxial torsion. This size effect exhibits an increase in normalised stiffness with increasing size of the sample. This contradicts both the predictions from classical elasticity and micropolar theory. As also observed in the cases of uniaxial unconfined compression and cantilever bending, it can be said that these size effects are unrelated to micropolar behaviour and that these are observed due to the yielding together with micro-damage within the trabeculae. The increase in trabecular density caused by these effects thus lead to the stiffening effect exhibited by the bovine samples in Figure 6.9. There is the possibility that as the normalised stiffness of the sample continues to increase, yielding and micro-motions of the individual trabeculae no longer impact the overall behaviour to such a large degree. Hence, it can be postulated that at this point, micropolar behaviour would start being observed as the predominant behaviour within the material. This would be caused by size effects that are not related to yielding (which are anti-micropolar) but size-effects that are related to micropolar theory itself and are in fact predicted by such theory. Hence, a convergence of normalised stiffness towards micropolar theory and eventually towards a constant normalised stiffness as predicted by Classical Elasticity.

It is important to note that in the case of torsion, having a cuboidal sample creates stress concentrations at the edges of the cuboid. The sample shape is not ideal for analysis in torsion. In this case, this was done because the initial plan was to analyse the samples in compression and bending only. In compression, no size effect behaviour should have been observed, whilst in bending, a micropolar size effect should have been observed according to theory. However, this was not the case in both loading modes and such an observation warranted the need to test in a different loading mode to ascertain whether such size effect behaviour was consistently capable of

being observed. Since it was priorly observed (in the case of compression) that stress concentrators do not seem to affect the model to a high degree when the number of affected elements is relatively low, the same 3D models were used to test the samples under torsion too.

#### 6.4 – Summary

Within this section, the procedure for loading a 3D volume mesh in ANSYS from a direct scan of trabecular bone has been provided. This procedure is important because it gives insight into the loads and boundary conditions that were used for the loading of such models, and these can eventually be related and compared to the boundary conditions that were applied during the experimental validation phase. Furthermore, using such a model for carrying out finite element analysis provided the opportunity to gain information about the stress distribution within the microstructure of trabecular bone while concurrently yielding data related to the size effect behaviour for each loading mode analysed.

All the samples exhibited similar size effect behaviour under the three different loading modes (unconfined uniaxial compression, uniaxial torsion and cantilever bending). This contradicts what micropolar theory predicts and it also puts a certain level of doubt on literature that uses micropolar theory to model the size effect behaviour of cancellous bone. When this data is further supplemented with the stress distribution within the microstructure of cancellous bone under the three different loading modes, it can be theorised that the localised yielding and micro-damage within the trabeculae may be the cause of the increase in normalised stiffness that is observed within the bovine samples (which contrasts to the predictions obtained from Micropolar theory). This localised yielding and micro-damage is evidenced by the presence of stress concentrations on the thinner trabeculae, and eventually leads to the trabeculae being compressed into a tighter lattice within the microstructure. Despite the material model used not being capable of accounting for plasticity and/or damage, such an effect is still capable of being observed and it can be said that the inclusion of plasticity and damage would exacerbate the exhibition of this size effect behaviour as the tightening of the microstructural trabeculae would be observed to a higher degree in such a case. The tightening of this microstructural lattice leads to the exhibition of a stiffening effect within the bovine samples in all the three different loading modes even though such tightening is limited by the material model used within the simulation. It can be said that the observed stiffening effect is unrelated to micropolar theory. Further to this, micropolar theory is based on the assumption that the characteristic length and thickness of the model being analysed is uniform within the whole

specimen. In the case of trabecular bone, this is not the case as the trabecular thickness is variable along the length of every single trabecula and the trabecular length can vary within the model as also evidenced by Figure 5.3 and Figure 5.4.

## 7 Idealised models

### 7.1 – Introduction

In the previous sections, the image processing techniques used to obtain volume meshes of the bovine sample used were described. These volume meshes were used in this section to create finite element models of the bovine samples being loaded in the three different loading modes described earlier (compression, torsion and bending). In this section, idealised heterogenous models are created and analysed in these same loading modes using finite element software to observe whether similar behaviour to the bovine samples can be observed. This is done so that the micro-scale stress distribution together with size effect behaviour can be analysed and compared to the models created in Chapter 6 whilst also giving insight into the relationship between the micro-scale stress distribution and the size-effect behaviour of such structures on the macro-scale.

The significance of these models arises from the need to reduce the efforts in modelling periprosthetic stress in cancellous bone. If any of these models is found to be representative of cancellous bone in terms of size effect behaviour, this would mean that the microstructure of cancellous bone does not need to be accurately modelled but such a computer-generated model would be used instead. Thus, eliminating the efforts needed to obtain very high resolution images using  $\mu$ CT scans so that the microstructure can be obtained. Such models would also simplify the process of understanding the micro-mechanics of cancellous bone through finite element modelling and eventually creating a material model that incorporates the micro-mechanical stress distribution in trabecular bone. This would in turn mean that stress shielding in trabecular bone can be modelled more accurately and aseptic loosening could eventually be mitigated.

### 7.2 - Models used

The idealised models that were compared to the bovine samples consisted of unit cells made up of rods. Each unit cell had the same length as the trabecular length obtained from morphometric analysis of the bovine sample. The radius of the rods was then varied such that the bone percentage volume in the sample and in the idealised models remained the same (11.65%). The idealised models used are described below:

- Regular cross array

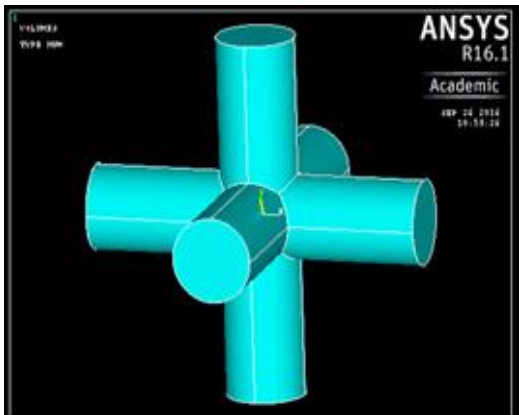


Figure 7.1: Unit cell of the regular cross array

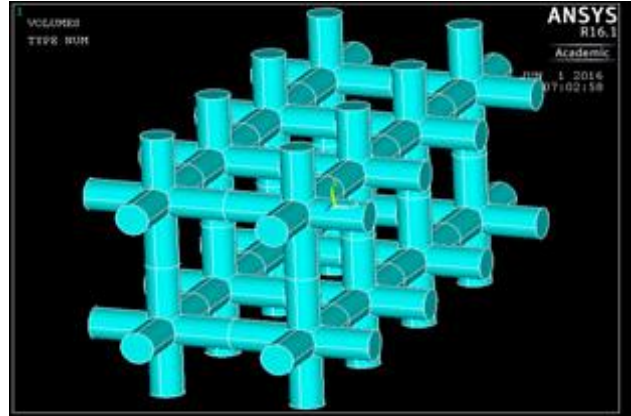


Figure 7.2: The regular cross array with multiple unit cells

This array had the unit cell shown in Figure 7.1, which was then replicated in the three axial directions as shown in Figure 7.2 to create models that were the same overall size of the scanned samples.

This was the most basic model used to represent trabecular bone. The rod length selected for this model was based on the trabecular length whilst the trabecular thickness was calculated such that the ratio of bone volume to total volume (BV/TV) is equivalent to that of the  $\mu$ CT scanned trabecular bone.

- Perturbed array

This array had the same base formulation as the regular cross array; however, randomised perturbations of different degrees were added to the intersection points as shown in Figure 7.3. The randomised perturbations were added by creating an array with random numbers representing the displacements and then applying these displacements to each intersection within the model. After applying these displacements, the geometry was then updated to the deformed state and any pre-stress conditions were cleared. Further to this, displacements were scaled by 0.05 to reduce the magnitude of displacements. This effectively also removed any defective elements that may have been caused due to excessive displacements of some elements.



Figure 7.3: The perturbed array

This array was considered as a slightly more accurate representation of trabecular bone since random perturbations are added to the intersection nodes. Rod length and thickness used for this model were kept the same as the regular cross array.

- Cubic array

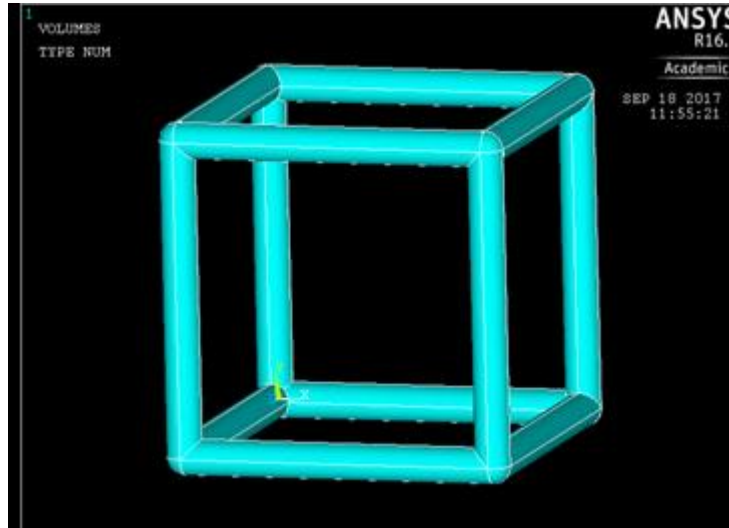


Figure 7.4: Unit cell of the cubic array

This array had the unit cell shown in Figure 7.4, which was then replicated in the three axial directions to create models that were the same overall size of the scanned samples.

The aim of this array was to create a representation of bone similar to the regular cross array but having less surface discontinuities. Rod length was once again based on the trabecular length whilst rod thickness was calculated in such a way that the ratio of bone volume to total volume (BV/TV) would be equivalent to that of the  $\mu$ CT scanned trabecular bone.

- Cubic array with diagonal intersections

This array had the unit cell shown in Figure 7.5, which was then replicated in the three axial directions to create models that were the same overall size of the scanned samples.

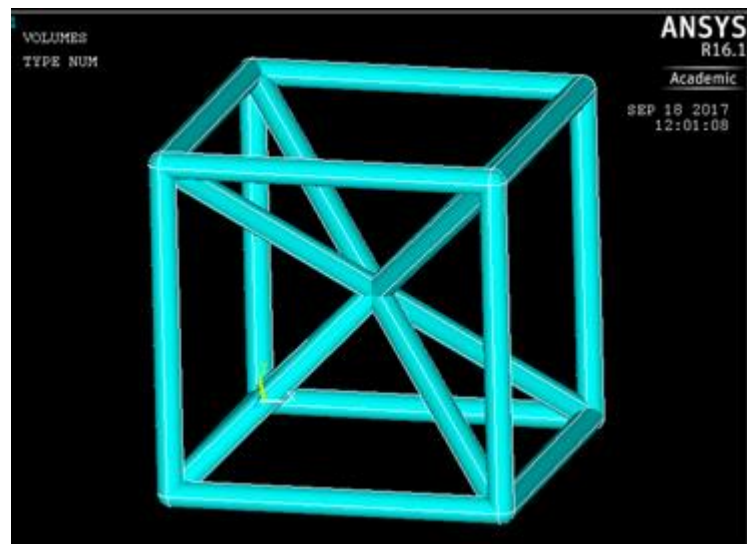


Figure 7.5: Unit cell of the cubic array with diagonal intersections

The aim of this array was to create a representation of bone similar to the cubic array but having intersecting rods that should increase the stiffness of the model. These rods were added to analyse whether this model would be a more accurate representation of trabecular bone as well as to analyse whether the added rods would increase the overall stiffness on the macro-scale. Length of the unit cell was once again based on the trabecular length whilst rod thickness was calculated in such a way that the ratio of bone volume to total volume (BV/TV) would be equivalent to that of the  $\mu$ CT scanned trabecular bone.

All these models were tested in the same loading modes using the same boundary conditions as those that were used for the bovine samples (i.e. unconfined uniaxial compression, cantilever bending, uniaxial torsion).

### 7.3 - Mesh sensitivity

The elements used for meshing the models described above were the SOLID185 elements (single order solid elements). These are tetrahedral elements which have three degrees of freedom (displacements in the x, y, and z directions). Mesh sensitivity studies were carried out for all models within this study except the cubic model with diagonal intersections (the number of elements for these structures when using very small elements exceeded the allowable maximum number of

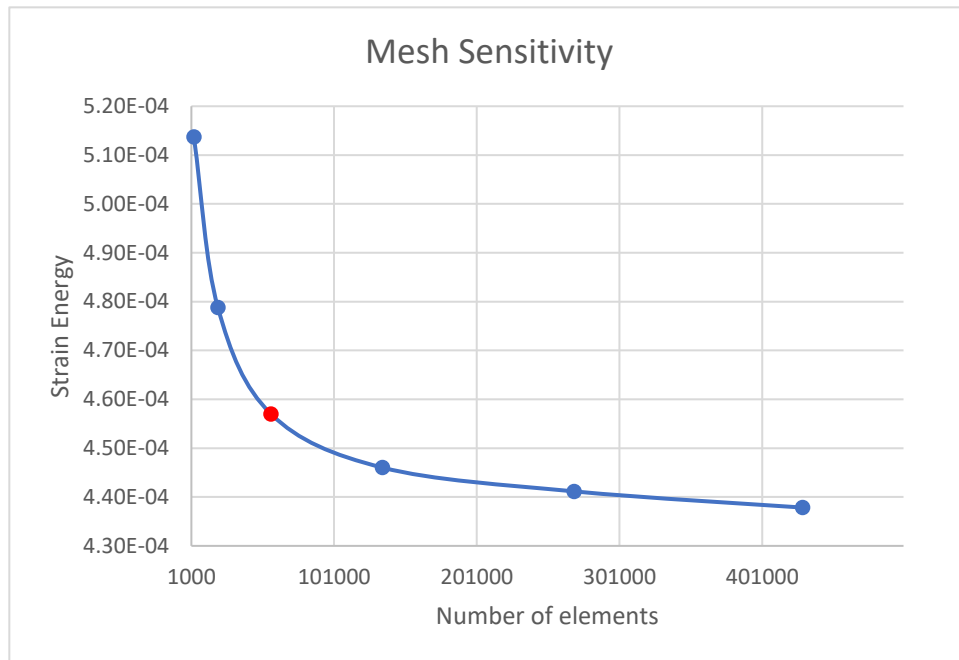


Figure 7.6: Results of the mesh sensitivity studies

elements that an academic license allows). Mesh sensitivity studies analysed the total strain energy and yielded results indicated in Figure 7.6. In this case a mesh size of  $\frac{r_h}{3}$  was deemed as the ideal mesh size for the models (shown in red on Figure 7.6). This because a larger mesh size would result in a relatively large variation in the accuracy of results whilst a finer mesh would only increase the accuracy by a smaller degree at the expense of a large demand on computational power as can be seen in Figure 7.6. It was also noticed that at an element size that was larger than the selected ( $\frac{r_h}{3}$ ), the number of elements within the larger models increased to a number that was beyond the allowable limit for an academic license of the software being used. This meant that apart from a limitation on computational power needs, there was also a limitation on the amount of elements that could be used in a any singular simulation, and in this case, the maximum number of elements for the larger models was at the selected mesh size indicated in Figure 7.6.

## 7.4 – Results

### 7.4.1 – Compression

As shown in Figure 7.7-Figure 7.10, both the cubic array and the regular array indicate that the load is mostly taken on the trusses that are parallel to the loading direction. This means that in this case no size effects should be observed and any differences in exhibited normalised stiffness can be attributed to inaccuracies during the meshing and solving processes during finite element simulation. In the case of the regular array with added small perturbations, the loading pattern is very similar to the unperturbed array as the perturbations are on a very small scale. It can be noticed that the random perturbations aid in distributing some of the load to the trusses that are perpendicular to the loading direction while these also seem contribute to the exhibition of stress concentrations at the intersection of trusses. This means that a slight size effect behaviour should be observed in such a case. As was observed in Figure 7.9, in the case of the perturbed array, a small size effect behaviour could be observed, but this was very minimal when compared to that observed from the bovine samples. Also, this model exhibits a slight decrease in stiffness with an increase in sample size, further indicating that any size effects would result in different size effects

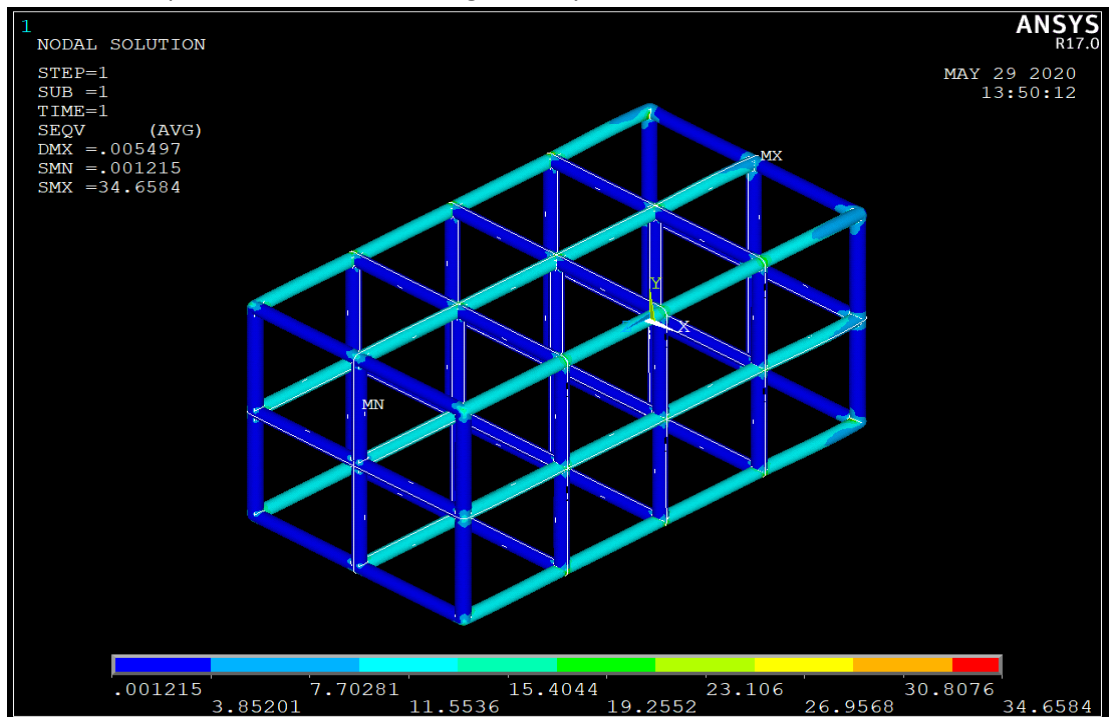


Figure 7.7: Von-Mises Stresses for compression of the cubic array that were observed from the bovine samples.

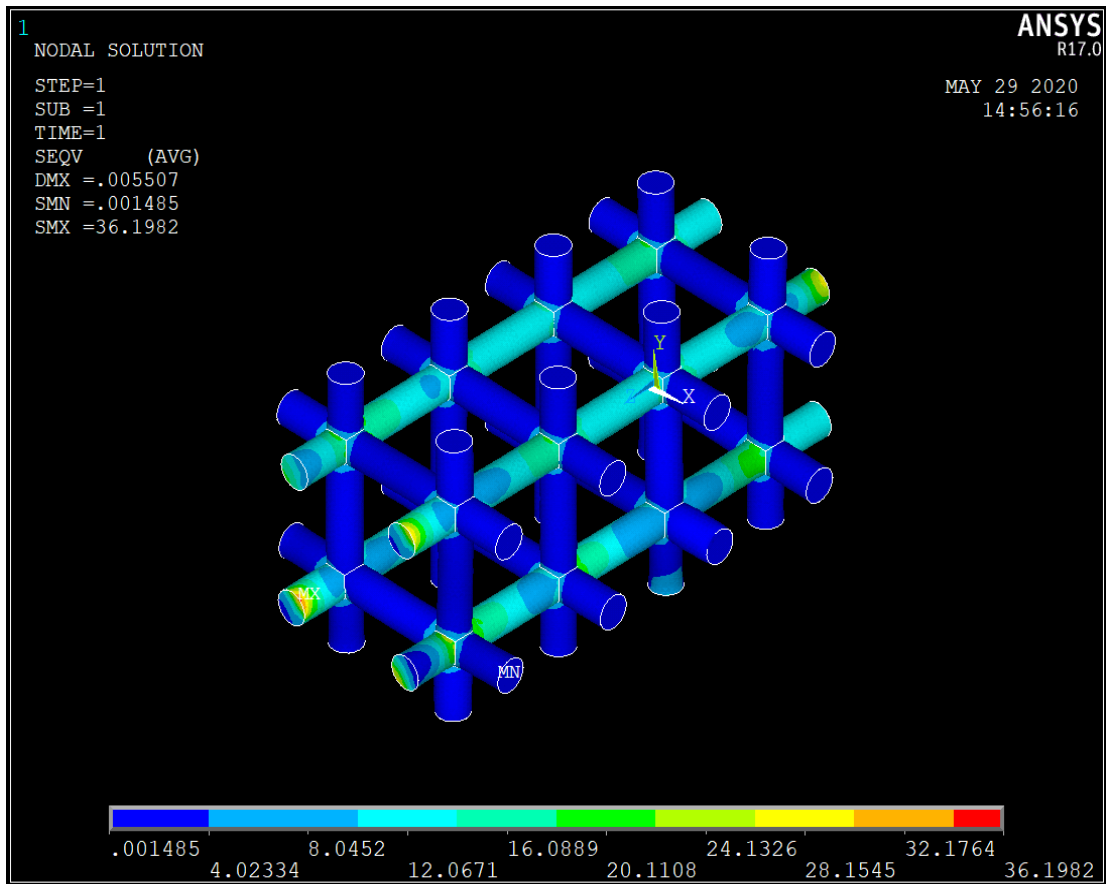


Figure 7.8: Von-Mises Stresses for compression of the regular cross array

As can be seen in Figure 7.8, in the case of the regular cross array, no size effect was observed. There was only a slight variation in normalised stiffness between different sizes of samples. This could be attributed to the effects of meshing accuracy. It can also be observed that only 50% of the struts are loaded and that these struts are all oriented in a direction that is parallel to the loading direction. This means that in this case, half of the model is made redundant and does not contribute to any load-bearing activity. This in turn leads to an exhibited stiffness that is smaller than that predicted by classical and/or micropolar theory.

The perturbed cross array exhibited similar behaviour to the regular cross (Figure 7.10), however; the normalised stiffness was slightly lower than that of the regular cross array. This can largely be attributed to the accuracy of the meshing process due to the perturbations. One would expect the to observe a certain degree of size effect behaviour due to the perturbations that were introduced

in this model. However, this is not in turn exhibited in this model as the magnitude of the introduced perturbations was so small that it only affected the stress distribution to a very minimal degree.

Both cubic arrays exhibited a size effect behaviour. The array without added diagonals exhibited a slight increase in stiffness as the size of the samples increased, while the stress distribution within the model was very similar to the regular cross array and the perturbed cross array. Similarly to the other models, this means that only the struts oriented in a direction that is parallel to the loading direction are being loaded. Hence, we can also conclude that the observed variation in normalised stiffness does not occur due to any size-effect behaviour within the material but due to any inaccuracies during the meshing process. The stiffness of the cubic array is higher than the regular cross array and the perturbed cross array. This can be attributed to the fact that within the latter two arrays only four struts are parallel to the loading direction. However, within the cubic array the load is being distributed between nine struts. Although these struts have a smaller diameter so that the average trabecular density is kept consistent between models, the addition of more struts for load distribution provides an opportunity for the model to exhibit a higher stiffness.

In terms of load distribution, the cubic array with added diagonals was highly similar to the cubic array in that only struts that are parallel to the loading direction are being used for load bearing purposes. The slight decrease in normalised stiffness can also be attributed to small error within the meshing process similarly to the cubic array. In this case, it can also be noticed that the addition of diagonal struts to the model contributed to a decrease in average stiffness compared to all the other models. This occurs because similarly to the cubic array model, nine struts are being loaded within this model. However, the diameter of these struts was once again reduced so that the average trabecular density remains consistent between models. Thus, the decrease in normalised stiffness can be attributed to the relatively large decrease in diameter of the struts due to the addition of an extra four diagonal struts which do not contribute to any load bearing activity.

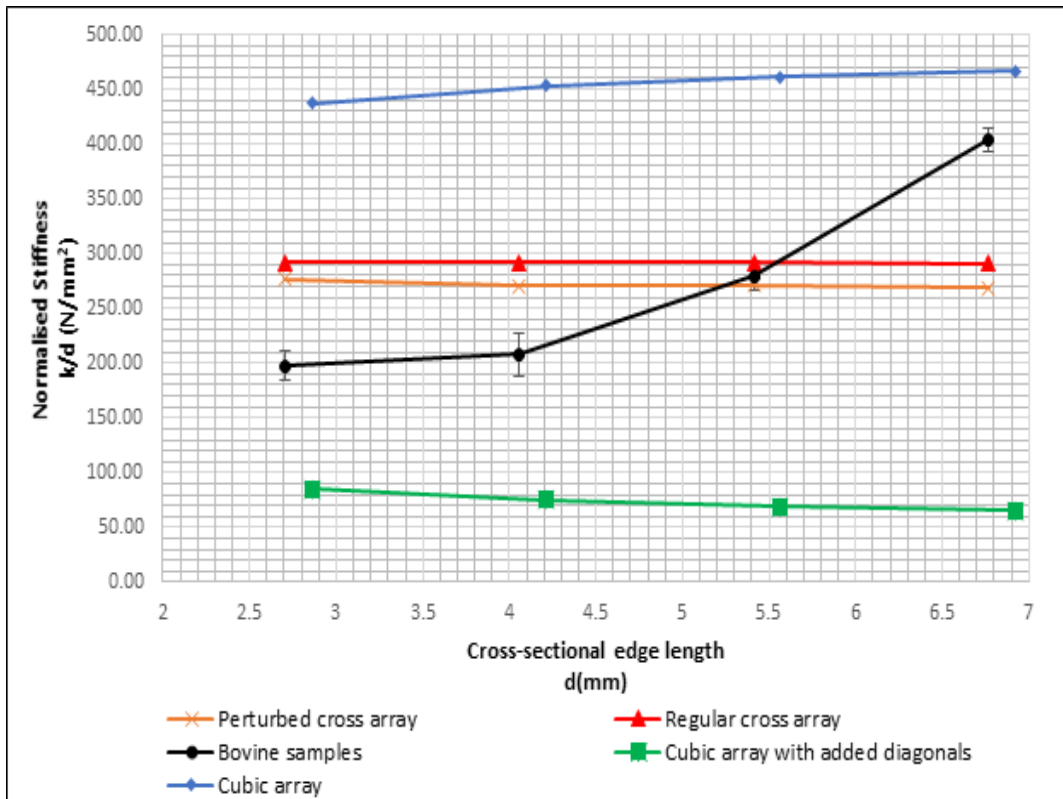


Figure 7.9: Size-effect behavior of computer-generated models under compression

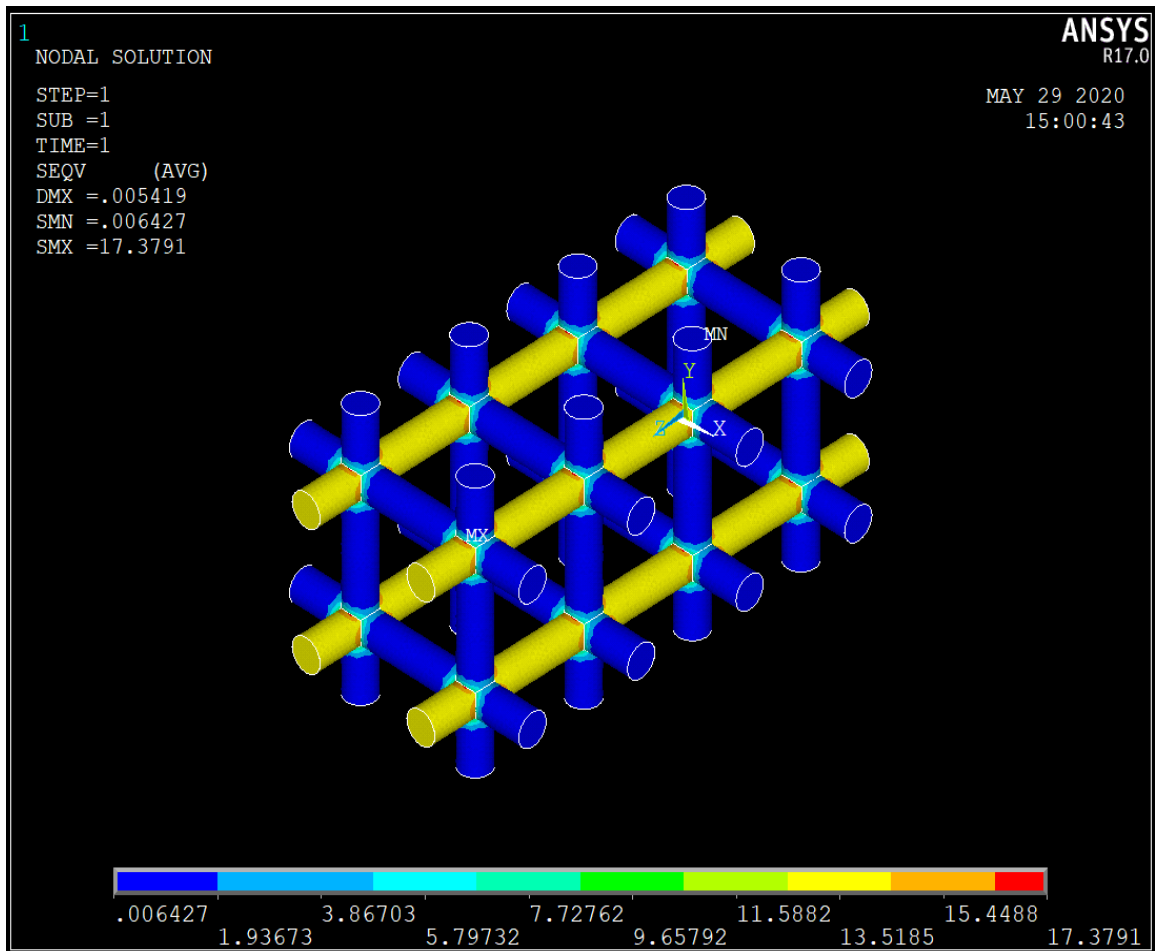


Figure 7.10: Von-Mises Stresses for the regular cross array with perturbations

### 7.4.2 – Torsion

As shown in Figure 7.11-Figure 7.12 within the bovine samples load is distributed through the whole microstructure. any stress concentrations can be assumed to occur due to inaccuracies during the meshing process resulting in sharp edges. In the cubic array (Figure 7.11), load is mostly taken on the trusses that are at the surface. The trusses that are parallel to the axis of torsion seem to take more load than the trusses that are orthogonal to the axis of torsion. Stresses also seem to aggregate at the points of intersections causing slight stress concentrations. All these factors can be said to contribute towards the micropolar size-effect behaviour indicated by such a structure. The perturbed and regular arrays (Figure 7.13 and Figure 7.12) behave in a very similar fashion in that there seems to be no difference in loading between the trusses parallel to the torsion axis and those orthogonal to it. Once again, stress concentrations appear at the intersection points. However, the uniform loading within trusses seems to contribute to an anti-micropolar size effect as also described by (Wheel et al., 2015).

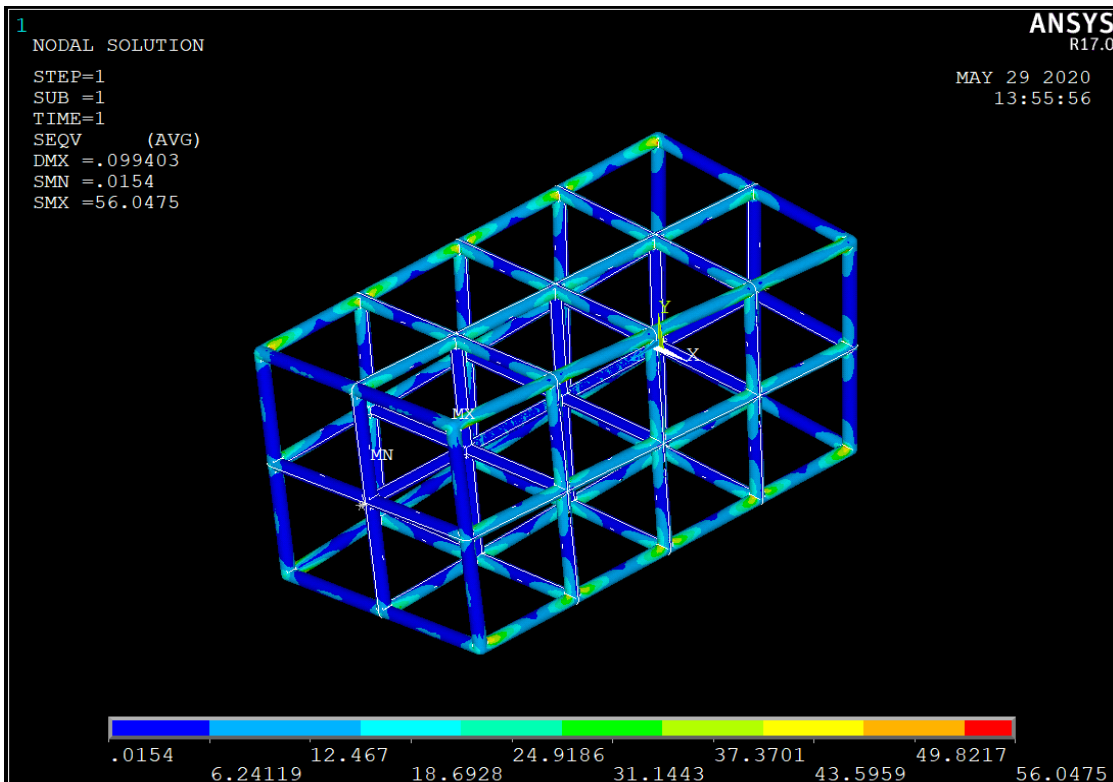


Figure 7.11: Von-Mises Stresses for torsion of the cubic array

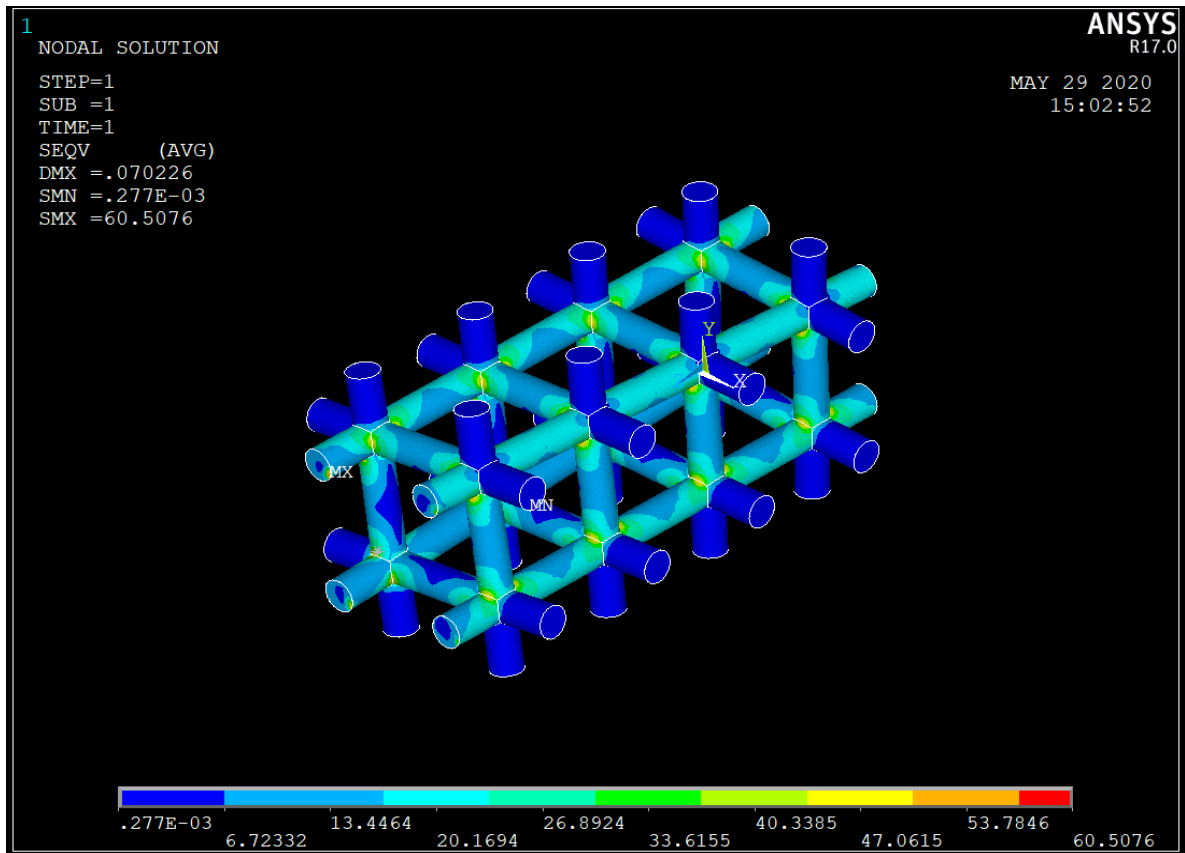


Figure 7.12: Von-Mises Stresses for torsion of the regular cross array

As can be seen in Figure 7.14 and Figure 7.15, in the case of the regular cross array, a size effect of small magnitude was observed with a trend of increasing normalised stiffness with size of the samples. This normalised stiffness seems to converge towards a constant value as the sample grows larger in size. The perturbed cross array exhibited similar behaviour, however; the normalised stiffness was slightly higher than that of the regular cross array whilst the magnitude of the size effect was reduced.

Both cubic arrays exhibited a size effect behaviour with a decrease in stiffness as the size of the samples increased. It can also be observed that the cubic array with added diagonals exhibited a lower stiffness in torsion than the array without added diagonals since the diameter of the struts for the latter model is smaller to keep a consistent trabecular density between models.

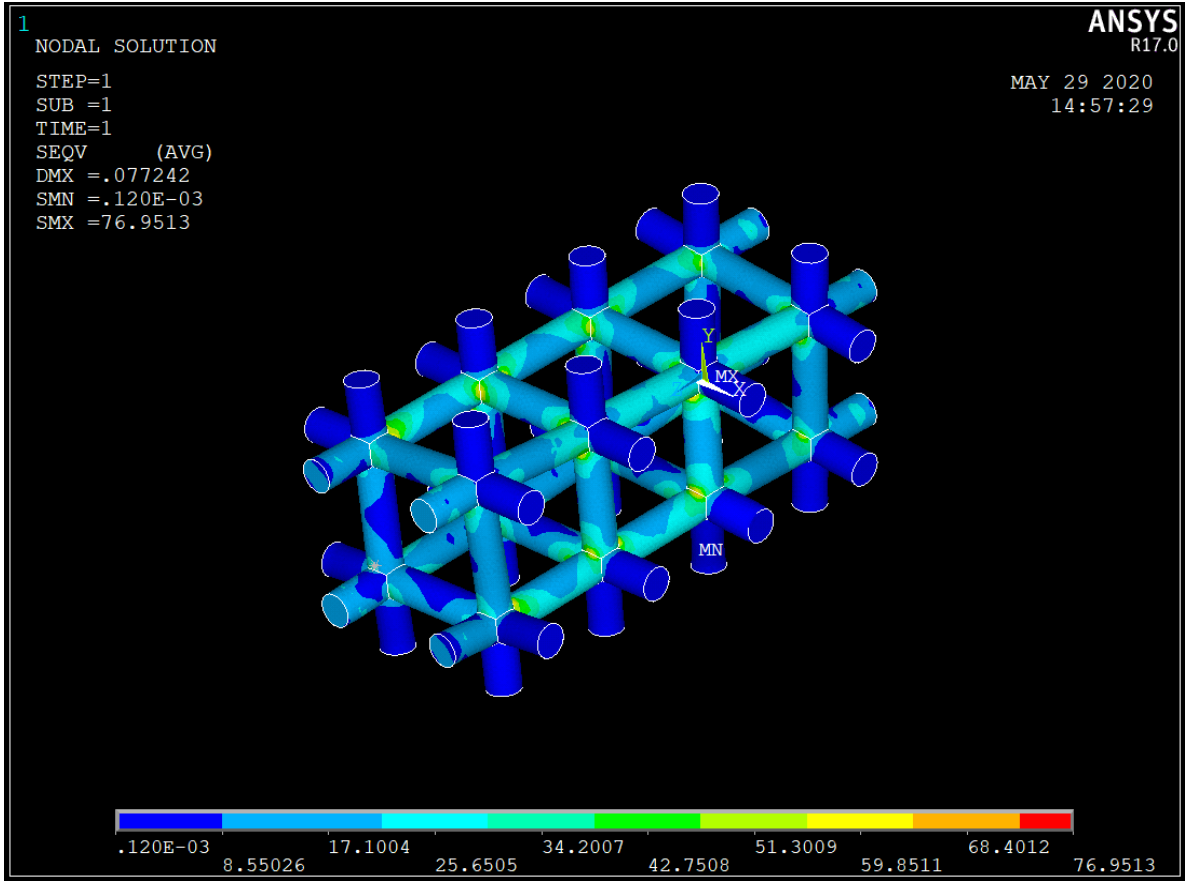


Figure 7.13: Von-Mises Stresses from the regular cross array with added perturbations

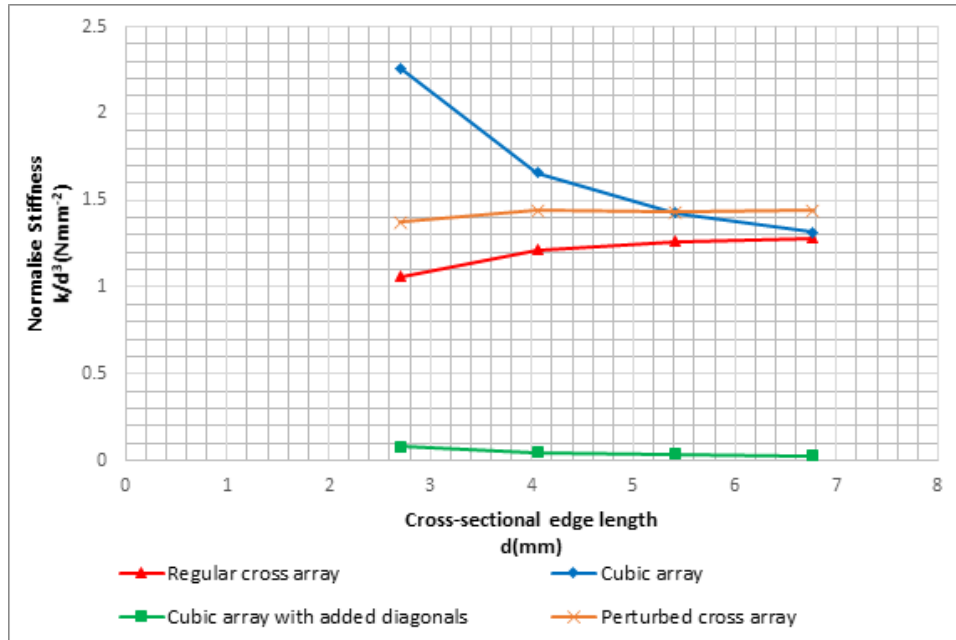


Figure 7.15: Size effect behaviour of the computer-generated models

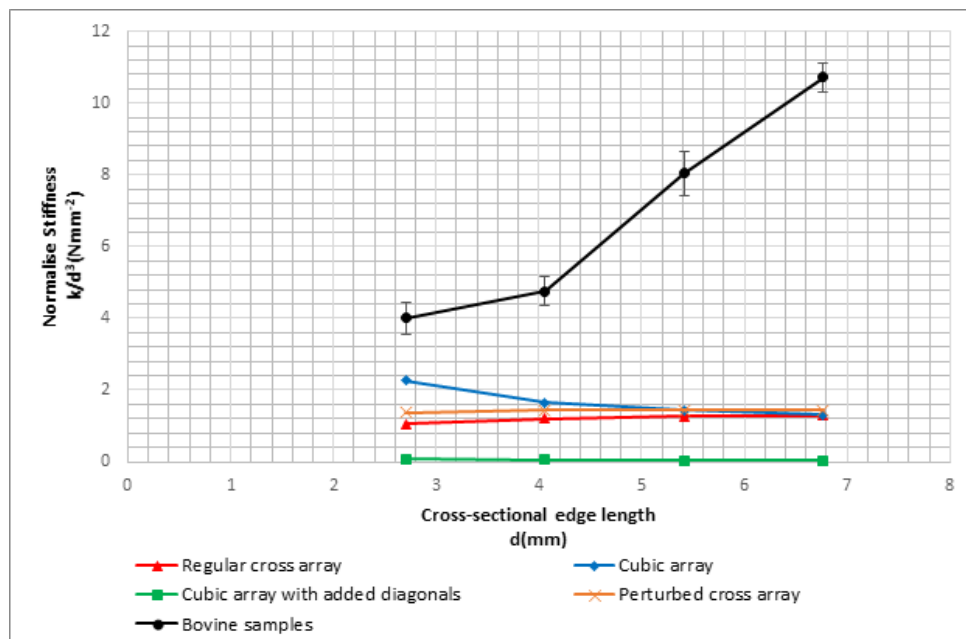


Figure 7.14: Size effect behaviour of computer-generated models compared to the bovine samples

### 7.4.3 – Bending

As can be seen in Figure 7.20 and Figure 7.19, the computer-generated arrays behave in a completely different manner when compared to both the bovine samples and the computer-generated arrays. The cubic array exhibits micropolar size-effects. On the other hand, the regular and perturbed arrays exhibit an increase in stiffness with an increase in sample size. This difference in behaviour can be attributed to the differences at the surfaces of the array where the cubic array and the cubic array with diagonals have continuous edges at the surfaces of the array whilst the other two arrays do not have continuous edges at the surfaces of the array. This difference in continuity at the surface has been proven to affect the micropolar and anti-micropolar size effects exhibited by arrays as described in (Wheel et al., 2015).

If the stress distribution within the model is analysed, one can also note a very similar loading pattern in the trusses that are parallel/perpendicular to the loading axis (Figure 7.16-Figure 7.18). This means that any difference in size effect behaviour is unlikely to be caused by the stress distribution with the model in the case of regular arrays. One may also note that the cross array with perturbations (Figure 7.18) aids in reducing stress concentrations at the intersections in this case. This also causes it to exhibit a marginally lower stiffness than the regular cross array.

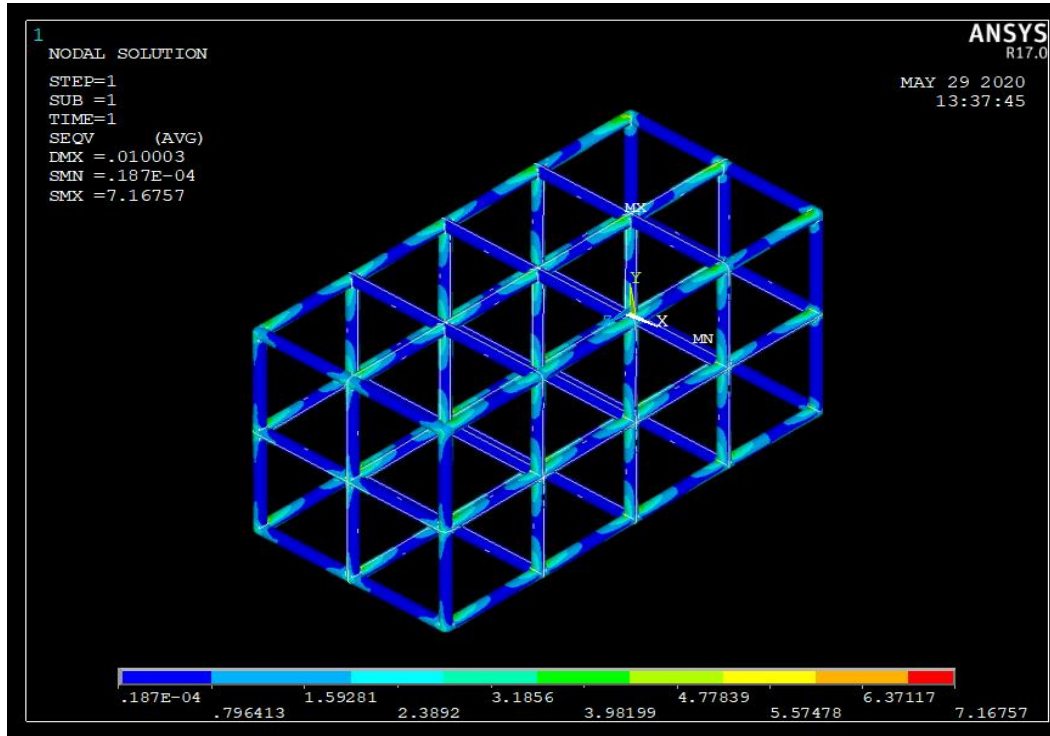


Figure 7.16: Von-Mises Stresses for cantilever bending of the cubic array

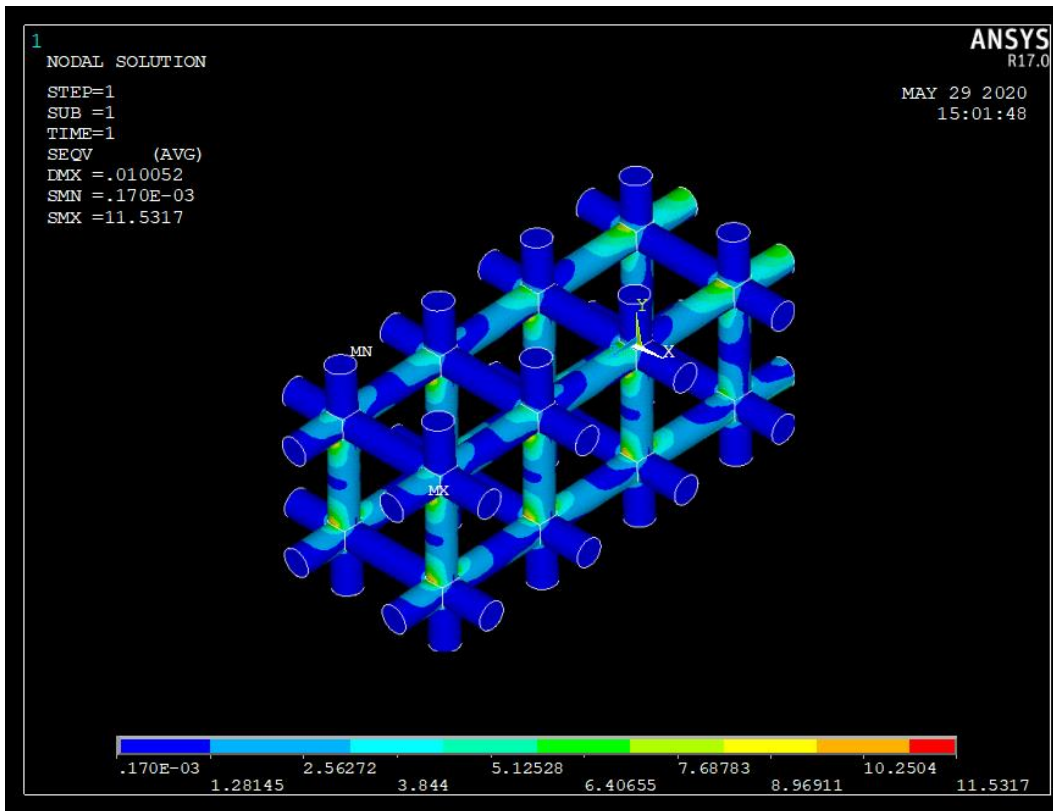


Figure 7.17: Von-Mises Stresses for cantilever bending of the regular array

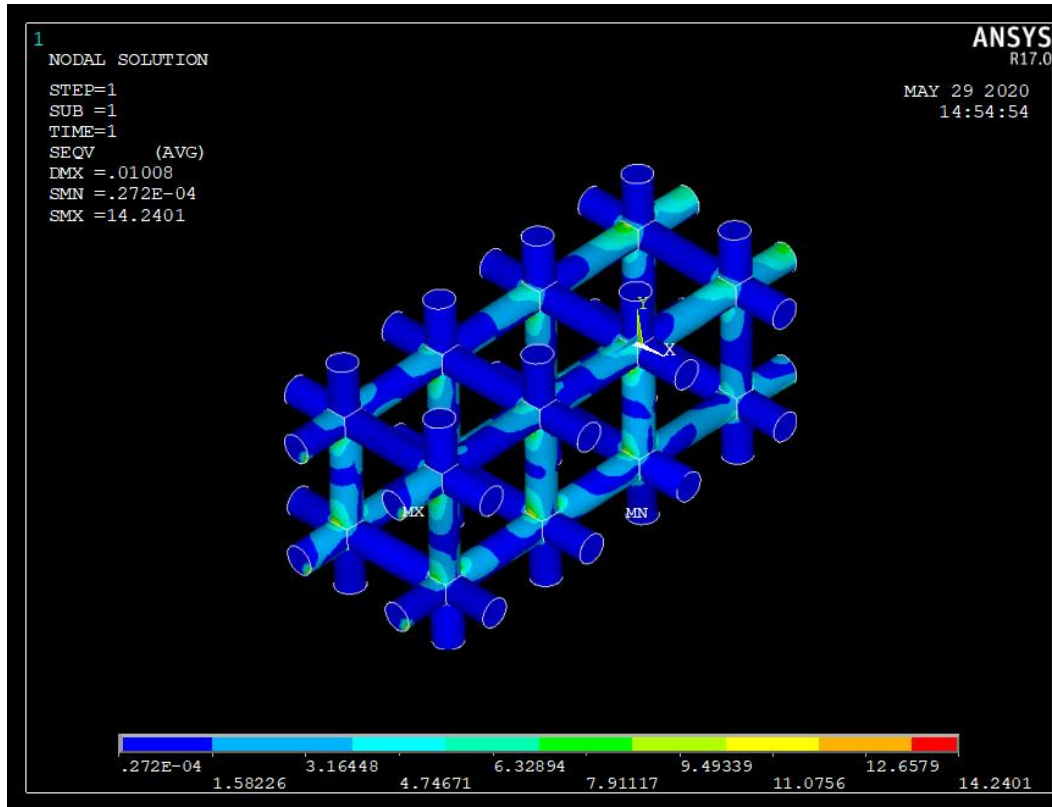


Figure 7.18: Von-Mises Stresses for cantilever bending of the regular cross array with added perturbations

As can be seen in Figure 7.20 and Figure 7.19, in the case of the regular cross array, a size effect of small magnitude was observed with a trend of increasing normalised stiffness with size of the samples. This normalised stiffness seems to converge towards a constant value as the sample grows larger in size. The perturbed cross array exhibited similar behaviour, however; the normalised stiffness was slightly higher than that of the regular cross array whilst the magnitude of the size effect was reduced. The effect of perturbations appears to be negligible with smaller samples, however; the effect of perturbations seems to affect the normalised stiffness more when the samples are larger in size. This results in a higher normalised stiffness in the cross arrays with perturbations that were of larger size.

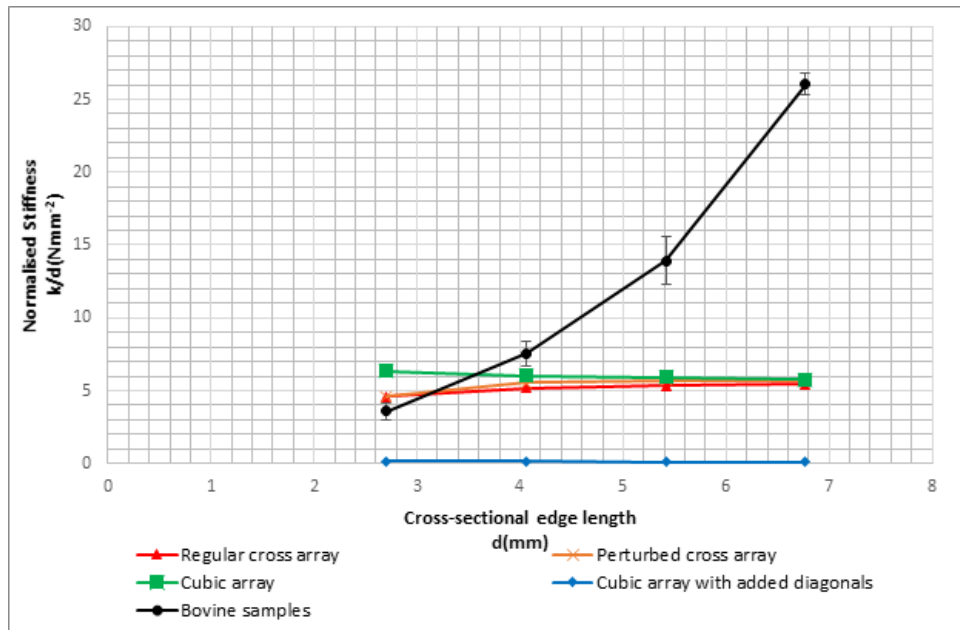


Figure 7.20: Size effects for cantilever bending of the computer-generated models compared to the bovine samples

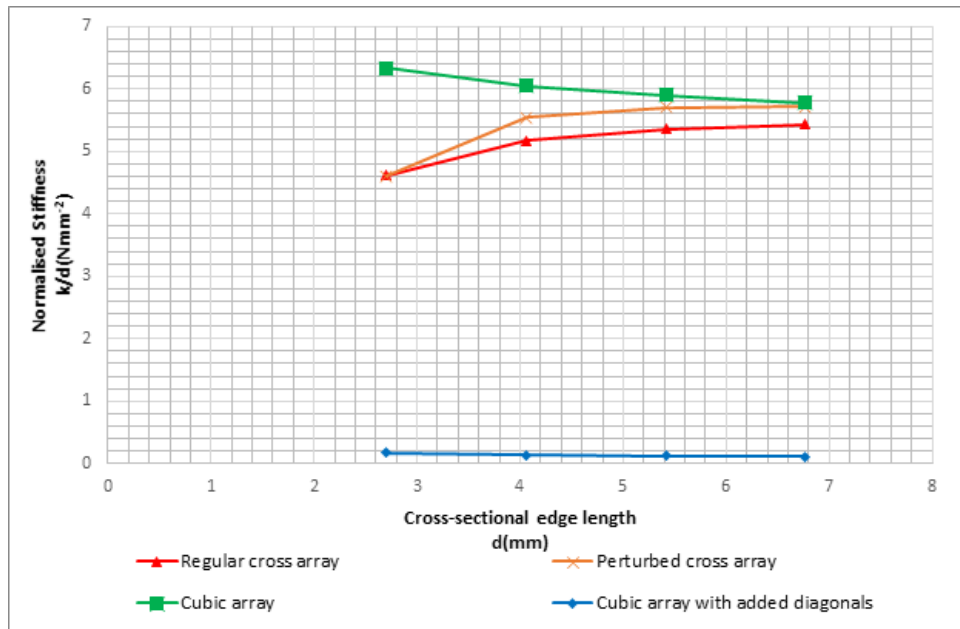


Figure 7.19: Size effects for cantilever bending of the computer-generated

Both cubic arrays exhibited a size effect behaviour indicating a decrease in stiffness as the size of the samples increased. It can also be observed that the cubic array with added diagonals exhibited

a lower stiffness in torsion than the array without added diagonals since the diameter of the struts for the latter model is smaller to keep a consistent trabecular density between models.

## 7.5 – Discussion

When the results from the computer-generated models are compared to the results from the bovine micro-CT scan, it can be observed that the overall trend in size effect behaviour is different to that obtained from the computer-generated models. This arises since the localised stresses at the thinner struts within the bovine samples result in localised yielding and micro-damage to the individual trabeculae. Such an environment arises from the variation in trabecular thickness along the struts and the randomised nature of the bovine samples. This leads to an increase in normalised stiffness due to an increase in trabecular density when the bovine samples are under load. With the regular nature of the computer-generated model, such localised yielding and micro-damage does not occur, thus there is no opportunity for an increase in trabecular density when the model is under load. This means that any size-effects observed within the computer-generated models are generated due to micropolar effects whereas size-effects within the bovine samples are generated through the variation in trabecular density as the model is loaded, rather than due to micropolar effects. When the results from the computer-generated models are compared to the results from the bovine micro-CT scan, it can be noted that the size effect behaviour from the bovine scans is much more evident. It can also be observed that the overall trend in size effect behaviour is different to that obtained from the computer-generated models. This arises since the localised stresses at the thinner struts within the bovine samples result in localised yielding and micro-damage to the individual trabeculae. Such an environment arises from the variation in trabecular thickness along the struts and the randomised nature of the bovine samples. This leads to an increase in normalised stiffness due to an increase in trabecular density when the bovine samples are under load. With the regular nature of the computer-generated model, such localised yielding and micro-damage does not occur, thus there is no opportunity for an increase in trabecular density when the model is under load. This means that any size-effects within the computer-generated models are generated due to micropolar effects whereas size-effects within the bovine samples are generated through the variation in trabecular density as the model is loaded, rather than due to micropolar effects. The stiffness of the scanned samples in torsion and bending is also much higher than that exhibited by the computer-generated models due to this same phenomenon.

## 7.6 – Summary

Within this section, the procedure for creating and loading various idealised computer-generated arrays that were used as a representation of the trabecular bone models modelled in FEA of Bovine samples. This procedure is important because it gives insight into the loads and boundary conditions that were used for the loading of such models, and these can eventually be related and compared to the boundary conditions that were applied during the experimental validation phase in Chapter 8. Furthermore, using such models for carrying out finite element analysis provided the opportunity to gain information about the stress distribution within the microstructure of trabecular bone while concurrently yielding data related to the size effect behaviour for each loading mode analysed. This data was correlated to the data from FEA of Bovine samples. It was further concluded that size effects exhibited by the computer-generated models conformed to micropolar theory whilst the size effects exhibited by the bovine samples occur due to a totally different mechanism. This mechanism refers to the micro-damage caused by localised yielding within the microstructure that eventually leads to an increase in trabecular density while the model is under load. Such data will also be correlated to results obtained within Chapter 6 and Chapter 8 in order to establish whether such models can truly be used as an accurate representation of trabecular bone, and which model would provide the most accurate representation.

## 8 Experimental Validation

### 8.1 – Background

In the previous chapter, results from Finite Element simulation of bovine samples and computer-generated models were obtained. In order to give a holistic approach to this study, it was decided that the results obtained from finite element modelling would be validated against results from experimental testing. This was done mainly because the results between computer generated models and the results from bovine samples exhibit different size effect behaviour.

The main problem when carrying out experiments is the issue of size. This because in this case, the samples are so small that no machine had the capability of handling samples with sizes within our range. For this reason, it was decided that such a problem would be solved by:

- Using the machines with the smallest load cells so that they could detect any small fluctuations in stiffness.
- 3D printing two samples of each size from the samples tested using finite element software and enlarging them by five times so that the samples can be handled in the available machines.
- Testing the samples under compression and torsion.

By doing so, the handling problems are eliminated. However, this gives rise to some discrepancies in boundary conditions and in material properties between the finite element models and the 3D printed samples. The discrepancies in boundary conditions were addressed and analysed by using finite element simulation to implement boundary conditions that are equivalent to those for experimental loading. Material properties for the 3D printed samples were assumed to be linear elastic. This means that the same constitutive model that was used for FE simulation is also used and consistency between models is maintained. The strains and displacements in the finite element mode were observed to be on a very small scale and as such, a linear model was used since the risk of loading beyond the yield point of the material is relatively small. Especially when taking into consideration the fact that very small displacements are applied to the models being tested within this section. The material properties are different in real life but the aim of this thesis was to analyse the trend in size effect behaviour and by using this assumption for material properties the general trend in size effect behaviour could be analysed without compromising the accuracy of the model to a large degree.

One shortcoming of assuming that the 3D printed material is linear elastic is that it is actually a non-linear material at high strains. As indicated in Section 6, there are regions within the microstructure that experience high strains. This means that such an assumption could have reduced the accuracy of the data. However, it could also be noted that the regions of high strain are relatively small in surface area and in number. This means that the degree to which such an assumption would affect the results would be minimal and it should not be enough to offset the general trend in size-effect behaviour of the macro-scale model.

## 8.2 – 3D Printing

As previously mentioned, the samples obtained from  $\mu$ CT scanning were converted to STL format so that they could be further processed and eventually converted from a surface mesh to a volume mesh. This format (STL) is also compatible with 3D printing software. This means that the exact same structure obtained from  $\mu$ CT scans could be 3D printed. Due to hardware limitations (printer resolution, nozzle size, etc.), the 3D models were printed at a scale of 1:5, however the trabecular architecture is identical to the samples tested using finite element software. This means that the

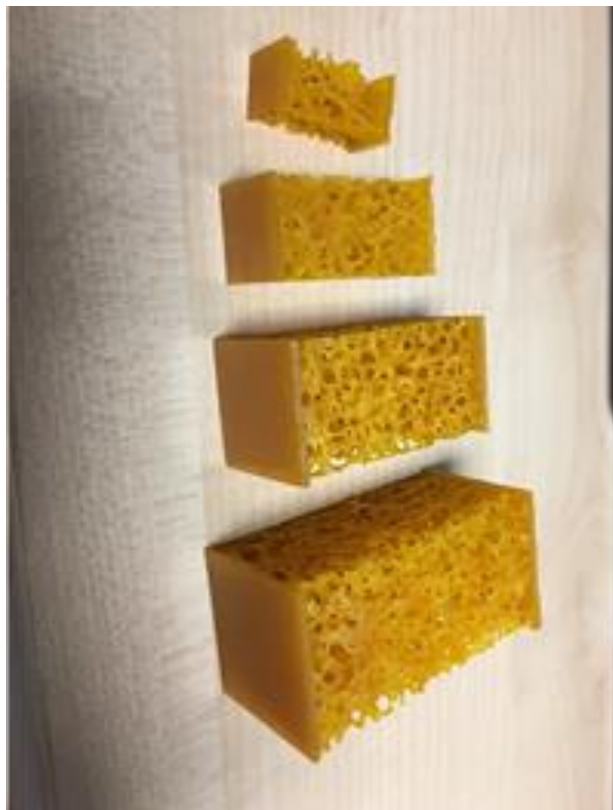


Figure 8.1: The enlarged 3D models that were printed together with plates at the ends

any size effect behaviour observed in finite element simulation should be observed during

experimental validation on the appropriate scale as described earlier. 3D printing was done using the Objet Eden350 printer at a 16 micron resolution. The material used for printing was the Objet Vero in yellow colour and it has material properties as indicated in Figure 8.2.

Vero PureWhite, VeroBlackPlus, VeroCyan, VeroGray, VeroMagenta, VeroMagentaV, VeroWhitePlus, VeroYellow, VeroYellowV		
	ASTM	Value
Tensile Strength	D-638-03	50 – 65 MPa (7,250 – 9,450 psi)
Elongation at Break	D-638-05	10 – 25%
Modulus of Elasticity	D-638-04	2,000 – 3,000 MPa (290,000 – 435,000 psi)
Flexural Strength	D-790-03	75 – 110 MPa (11,000 – 16,000 psi)
Flexural Modulus	D-790-04	2,200 – 3,200 MPa (320,000 – 465,000 psi)
HDT, °C @ 0.45MPa	D-648-06	45 – 50 °C (113 – 122 °F)
HDT, °C @ 1.82MPa	D-648-07	45 – 50 °C (113 – 122 °F)
Izod Notched Impact	D-256-06	20 – 30 J/m (0.375 – 0.562 ft-lb/inch)
Water Absorption	D-570-98 24hr	1.1 – 1.5%
Tg	DMA, E*	52 – 54 °C (126 – 129 °F)
Shore Hardness (D)	Scale D	83 – 86 (Scale D)
Rockwell Hardness	Scale D	73 – 76 (Scale M)
Polymerized Density	Scale M	1.17 – 1.18 g/cm <sup>3</sup>
Ash Content (VeroGray, VeroWhitePlus)	USP281	0.23 – 0.26%
Ash Content (VeroBlackPlus)	USP281	0.01 – 0.02%

Figure 8.2: Material properties of Objet Vero

In the case of unconfined uniaxial compression, thin plates had to be added to the samples so that these could be printed without breaking the trabeculae. These plates (shown in Figure 8.1) also serve as a stable surface where the sample can make contact with the compression platens on the machine and they are made of the same material as the rest of the sample (acrylonitrile butadiene styrene). In this case, it can be assumed that these plates do not deform and are rigid since very small displacements are being used. This means that the boundary conditions in this case are different from those used for the finite element simulations. In this case, finite element models

allow surface warping by allowing displacements in the y- and z-direction. On the other hand, for the experimental validation, such displacements are not allowed meaning that surface warping is not allowed. A simple finite element test was used to verify whether there is a very large difference between the experimental boundary conditions and the unconfined uniaxial compression boundary conditions used for finite element modelling. This was done by testing one of the smaller samples using finite element analysis using the experimental boundary conditions as depicted by Figure 8.4. Subsequently the percentage difference between both experimental and finite element boundary conditions was calculated. The percentage difference in normalized stiffness between samples was



Figure 8.4: The boundary conditions used for the experimental validation (a) not allowing surface warping ( $u_y, u_z=0$ ) and for the finite element simulations (b) allowing surface warping ( $u_y, u_z \neq 0$ )



Figure 8.3: 3D printed bovine samples used for uniaxial torsion together with the added flanges to enable testing

found to be <3.4%. Thus, it was concluded that the experimental boundary conditions should not have a large difference from the finite element model tests in terms of stiffness.

In the case of uniaxial torsion, flanges had to be added to the samples so that the samples could be gripped appropriately (shown in Figure 8.3). In this case, it was assumed that these plates do not deform and are rigid since a very small torsion angle was used. This means that the boundary conditions in this case were different from those used for the finite element simulations. In this case, finite element model allow surface warping by allowing displacements in the y- and z-direction. On the other hand, for the experimental validation, such displacements are not allowed meaning

that surface warping is not allowed. A simple finite element test was once again used to verify whether there is a very large difference between the experimental boundary conditions and the unconfined uniaxial compression boundary conditions used for finite element modelling. This was done by testing one of the smaller samples using finite element analysis using the experimental boundary conditions as depicted by Figure 8.5. Subsequently the percentage difference between

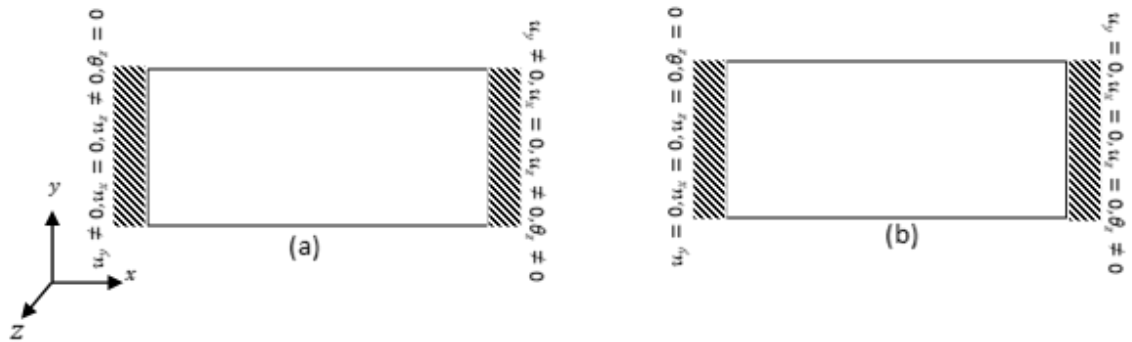


Figure 8.5: The boundary conditions used for finite element simulations (a) and for experimental validation (b)

both experimental and finite element boundary conditions was calculated. The percentage difference in exhibited normalized stiffness between samples was found to be <1.5%. Thus, it was concluded that the experimental boundary conditions should not have a large difference from the finite element model tests in terms of stiffness.

### 8.3 - Experimental setting

#### 8.3.1 - Number of samples

In the case of the experimental set-up, the same sizes used for the finite element analysis of the  $\mu$ CT samples were used. However, in this case, only two samples were tested for each size of the sample as depicted in Error! Reference source not found. below. In this case, only 2 samples for each size were printed due to time constraints arising from long printing times due to the highly complex geometry of the models being printed.

This means that a total of 8  $\mu$ CT samples were tested using finite element simulation.

Size (d=1.353mm)	2d x 2d x 4d	3d x 3d x 6d	4d x 4d x 8d	5d x 5d x 10d
Number of samples	2	2	2	2

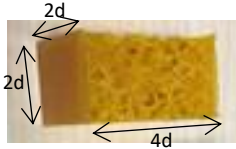
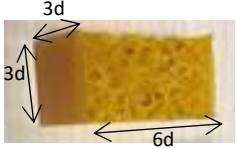
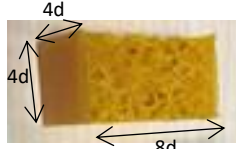
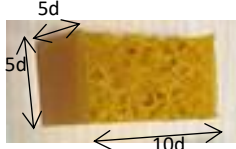
Image				
Maximum Load – Bose Electroforce 3200 (N)	7	7	7	7
Maximum Load – Instron Electropuls E3000 (N)	11	11	11	11

Table 8.1: The number of samples tested experimentally for each size

### 8.3.2 - Procedure overview

The 3D models obtained from  $\mu$ CT scanning were enlarged by five times. Subsequently, these were exported, and 3D printed. The 3D printed samples were then tested under unconfined uniaxial compression. Such a test was carried out using two different machines. This was done to minimise errors due to handling and/or equipment tolerances. The machines used for testing were:

- BOSE Electroforce 3200 with a 450N load cell,
- Instron Electropuls E3000 with a 3kN load cell.

## 8.4 – Testing

### 8.4.1 – Compression testing

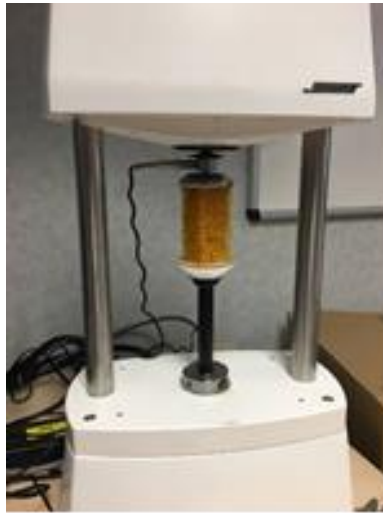


Figure 8.6: Compression testing of samples using the Bose Electroforce 3200

Two sets of tests in unconfined uniaxial compression were carried out on two different compression machines. The experimental protocol was similar in both cases with some minor differences due to hardware and time constraints. Each specimen was fixed by compressing between two platens within the compression machine.



Figure 8.7: The Instron Electropuls E3000

The first set was carried out on a BOSE Electroforce 3200 machine with a 450N load cell (Figure 8.6) having an accuracy of 2.25N. Each sample was tested a total of ten times to ensure repeatability of the test, and the average for each sample together with the standard error were calculated. A linear ramp-hold loading setting was used for both the loading and unloading phase, and only the loading phase was considered when obtaining results. The loading rate was of 0.2mm/min. The maximum load was modified for the different sample sizes so that the tests would be non-destructive whilst staying well below the plastic region. To achieve this, a maximum load of 7N was used for the largest samples, whilst a maximum load of 5N was used for the smallest samples. The largest samples started to exhibit an anomaly in size effect behaviour on this machine and it was suspected that the load cell had been damaged during other testing (for other research projects) that was being carried out in parallel. Thus, it was decided that the experiments would be repeated on a different machine.

The second set of tests was carried out on an Instron Electropuls E3000 machine with a 3kN load cell (Figure 8.7) having an accuracy of 15N. In this case, each sample was tested a total of five times and the averages for each sample together with the standard error were once again calculated. A linear ramp-hold loading setting was once again used in this case for both the loading and unloading phase, and only the loading phase was considered when obtaining results. The same loading rate used for the previous experiment was also used in this case. The maximum load was modified for the different sample sizes so that the tests would be non-destructive whilst staying well below the plastic region. To achieve this, a maximum load of 11N was used for the largest samples, whilst a maximum load of 6N was used for the smallest samples.

For each experiment done, the load vs. displacement data for both the loading and unloading case was obtained. This data was then trimmed to an appropriate start point where full contact of the

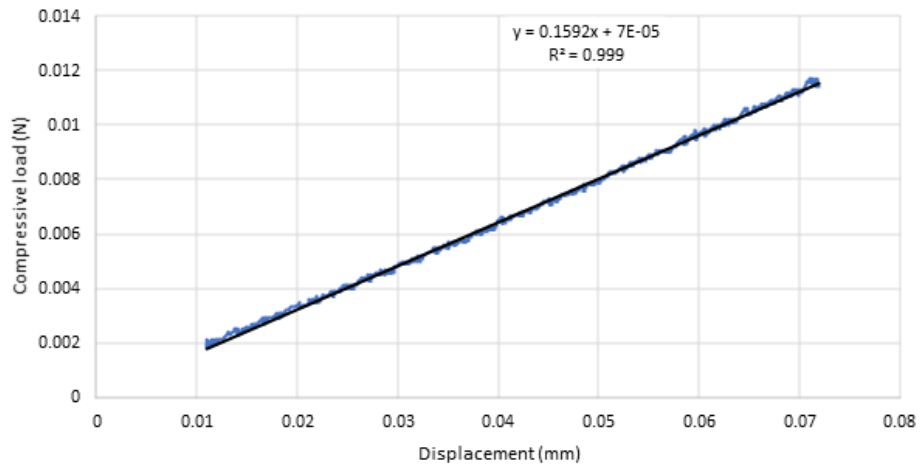


Figure 8.8: A graph of compressive load vs displacement for one of the samples

sample is made with the compression platens and the unloading phase was also excluded from the data. A graph of compressive load vs. displacement could then be plotted and a linear regression was fitted to the data as shown for one of the samples in Figure 8.8. The gradient of this line was then calculated to obtain the overall exhibited stiffness of each sample  $k$ , and this was then normalised by the cross-sectional edge length  $d$  to obtained values that are proportional to the overall exhibited Young's Modulus.

When calculating the stiffness from the gradient as shown in Figure 8.8, any misalignment between the sample and the platens was taken into consideration. Such misalignment would come from the sample being slightly bent due to the nature of the 3D printing process. To minimise this error, two steps were taken; recording on the machine was started only after the platens were visually observed to make full contact with the sample upon close examination. Another precaution that was taken was to eliminate initial parts of the graph where the relationship is non-linear. This initial non-linearity would have been caused due to additional material coming into contact with the platens in the case of inaccuracies when visually observing the sample in the previous step. It could also be observed that different samples gave very close results which also shows that the system was working appropriately. Such repeatability could also be observed when running compressions on the same sample, and also when testing different samples. In this case, elimination of non-linear readings does not affect the reading of stiffness as the gradient in the linear portion of the curve remains unaffected and only the y-intercept is affected, thus leading to an unaffected normalised stiffness.

#### 8.4.2 - Torsion testing

Upon trying to test samples under torsion, a problem with gripping the samples was identified. This was because the gripping force was too high and it would deform/break the 3D printed samples. As such there were plans to design a jig that fits into the grips of the machine so that samples could be gripped without getting deformed, however, there was not enough time to design these and testing had to be skipped.

#### 8.4.3 - Bending test

A test involving cantilever bending was also scheduled for the samples printed for compression testing. However, execution of these tests was not possible due to time constraints for the project.

#### 8.4.4 – Results

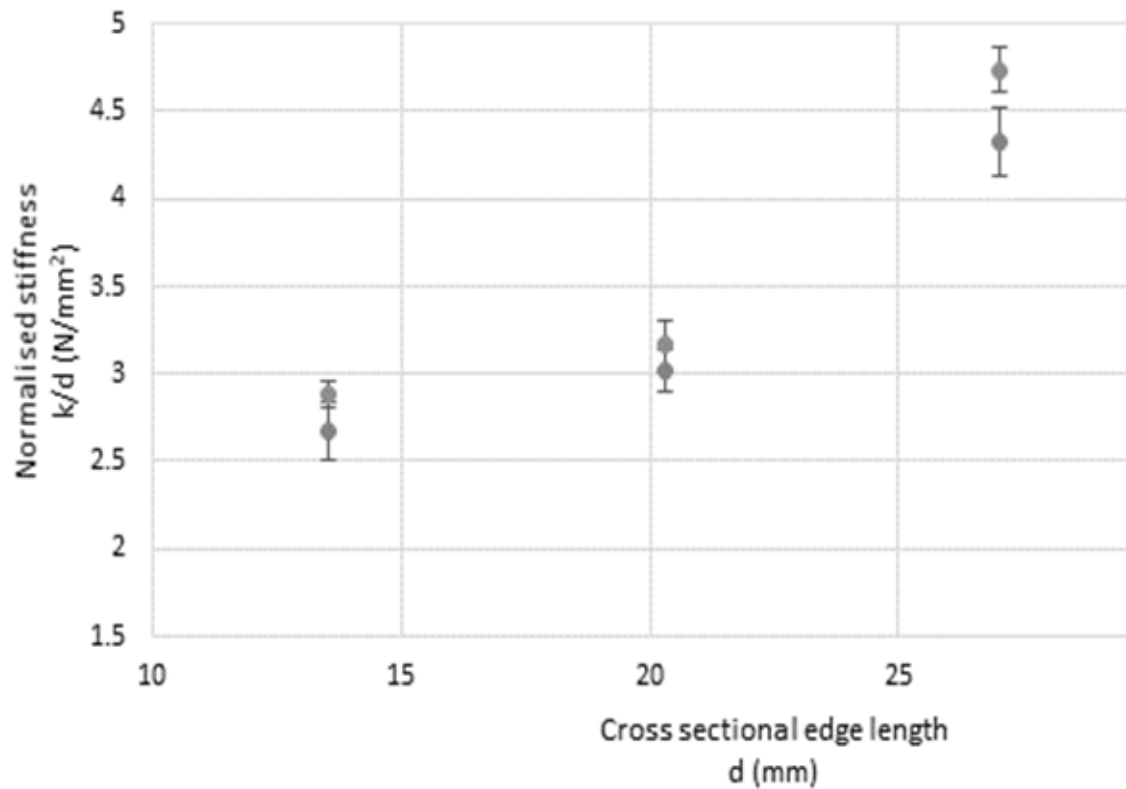


Figure 8.9: Results for compression of the bovine samples using the Bose Electroforce 3200 (different points indicate different samples with error bars indicating standard error for each sample)

Figure 8.9 above shows the relation of normalised stiffness to cross-sectional edge length of the 3D printed samples when they were tested under unconfined uniaxial compression using the Bose Electroforce 3200 machine. The plot shows the average of 10 tests for each sample with the error bars showing the standard error and different markers representing different samples. As can be seen, there is a trend of increasing stiffness as the size of the sample increases. However, this trend did not seem to hold for the largest sample that was tested. It is suspected that on the day when the largest samples were tested, the load cell had been damaged during use for other ongoing projects. Thus, there is a chance that results for the largest sample might be unreliable and/or inaccurate. For this reason, results for the largest sample are excluded in this case. It is important to note that such a size effect behaviour is not predicted in compression by micropolar theory, and a similar trend was also obtained when the  $\mu$ CT scans were used to create finite element models of trabecular bone (if the largest sample is not considered). When the increase in normalised stiffness observed in Figure 8.9 is compared to the results obtained from finite element simulation of the bovine samples in Section 6.3.1 (Figure 6.5), an evident similarity in size effect behaviour can be observed although the normalised stiffness lies in a different range between both models. This similarity in size effect behaviour further reinforces the theory that localised yielding and micro-damage contribute to the increase in normalised stiffness as the size of the sample increases due to an increase in trabecular density when the model is under load. Furthermore, the differences in magnitude of normalised stiffness between the models can be attributed to two factors. One such factor is the different materials properties of the individual trabeculae when compared to the 3D printed models since the 3D printed models are made of plastic whilst the bovine samples consist of excised real bone. The other factor possibly contributing to this difference in magnitude is the fact that the 3D printed samples were also enlarged by a factor of ten so that 3D printing could be made possible within the resolution of the available printer. Although this does not affect the exhibition of the size effect behaviour (since the length scales and aspect ratios are maintained), it is entirely possible that with the magnification effect, the overall normalised stiffness could vary.

The results obtained from the Instron Electropuls E3000 suggested a difference in behaviour than that which was observed in Figure 8.9 with the Bose Electroforce 3200. The overall normalised stiffness seemed to be slightly higher than that which was observed in Figure 8.9. This can be attributed to the fact that the Instron Electropuls E3000 has a larger load cell than the Bose Electroforce 3200. Such a load cell on the Instron Electropuls E3000 was used with a load that was around 0.1% of the load cell capacity which is not within the optimal range for accuracy of the load

cell. This means that precision might have been affected in this case, meaning that for very small samples, the load cell would have not been capable of measuring the loads accurately, resulting in an overestimation of normalised stiffness. It is also important to note that the same samples that were tested on the Bose Electroforce 3200 were retested later using the Instron Electropuls E3000, meaning that there is also a risk that the yield point of the printed samples may have been reached prior to testing on the Instron Electropuls, thus affecting the readings being read. The localised yielding and micro-damage caused by initial testing on the Bose Electroforce 3200 may have also caused a variation in stiffness of the samples. There was also the possibility that some localised yielding and micro-damage on the trabecular level from prior testing on the Bose Electroforce 3200 may have affected the stiffness of the samples being tested on the Instron Electropulse E3000. It was ensured that this was not the case since repeated test from on the same samples on the Bose Electroforce 3200 (prior to testing on the Instron Electropulse E3000) did not show any signs of plastic strain and repeated tests on the same sample provided very similar force-displacement graphs). It was thus concluded that any yielding in the samples and/or any inaccuracies in the results from the Instron Electropuls E3000 resulted from two main factors; the load cell not being accurate enough, and the load on the sample being excessive. All of these factors made the results from the Instron Electropuls E3000 inconclusive and only the results observed on the Bose Electroforce E3000 (Figure 8.9) were considered valid since at this point, the samples would not have undergone any localised yielding or micro-damage within the trabeculae.

### 8.5 – Summary

Within this section, the procedure for enlarging and 3D printing some of the trabecular bone models modelled in FEA of Bovine samples is provided together with results of the same printed samples under uniaxial unconfined compression using two different machines having load cells of different precision. It has been observed that results obtained from the Bose Electroforce E3200 are comparable in size effect behaviour to those obtained from the finite element models in Chapter 6. Results from the Instron Electropuls E3000 indicate that the load cell might have been too large for the measurement of forces and samples on this scale and as such are inconclusive.

This section provided further insight into the size-effect behaviour of the 3D printed samples and it also provided the opportunity to compare these results with those obtained from the testing of in silico models in FEA of Bovine samples. Comparison of the results of the Bose Electroforce 3200 with finite element models validated the accuracy of some of the bovine models in Chapter 6 in

terms of size effect behaviour and are very promising. No definite conclusions can be done from this testing since the number of samples tested was very small (only 2 samples for every size) and the largest two models gave inconclusive results due to the damage load cell.

## 9 Discussion and Conclusions

### 9.1 – Discussion

In the previous chapters, results of the various types of analyses have been provided. Finite element simulation of the bovine samples indicated an increase in normalised stiffness as the size of the sample increases. This contrasted with the predictions from micropolar theory, meaning that this theory may not be suitable for modelling the size effect behaviour of trabecular bone. Further analysis into the microstructural stress distribution within cancellous bone indicates that localised yielding and micro-damage of the trabeculae may lead to this stiffening effect as the size of the sample increases and similar behaviour was also observed in literature by Guillen et al., 2011 and Sabet et al., 2017. This means that such a size effect behaviour does not arise from micropolar effects, but rather from the mentioned localised yielding and micro-damage. This leads to compression of the trabeculae into a tighter lattice, increasing the density while the samples are under load. It is theorised that the tighter packing of the trabeculae while under load leads to the increase in normalised stiffness as the size of the sample increases, however, the sample sizes taken within this study also need to be taken into consideration. Only one large sample was used, and this sample was then further subdivided into different samples. Boundary conditions were not always modelled in the ideal way leading to potential inaccuracies within the results. Although such inaccuracies were accounted for and should not change the overall size effect behaviour observed, they also provide limitations on the confidence of this study.

Experimental results from the Bose Electroforce 3200 were also very promising and indicated similarities to finite element models of bovine samples under compression. This did not apply to the largest sample that was tested on the Bose Electroforce 3200. However, it is suspected that this sample was being tested with a defective or damaged load cell. Experimental results on the Instron Electropuls E3000 did not lead to any conclusive results. This arose from the fact that the load cell of this machine was not accurate enough for the loads being applied. Another potential cause of such inconclusive results could be the possibility of damaged samples when these were being tested on the Instron Electropuls E3000 arising from the fact that these same samples had been priorly tested on the Bose Electroforce 3200. The fact that experimental results were close to finite element simulation results in terms of general trend for size effect behaviour is promising. However, consideration on the fact that only two samples were 3D printed and tested. Further evidence and testing would need to be collected and tested to provide more confidence in these observations

whilst also eliminating the issues with defective hardware or load cell inaccuracies that were encountered within this phase of testing.

Computer generated models exhibited micropolar size effects where the smaller samples showed a higher normalised stiffness (micropolar size-effect). Analysis of the stress distribution under compression within such models shows that the regular structure of these arrays leads to the struts with the same orientation as the loading direction are loaded and this leads to the model following the predictions done by micropolar theory and classical elasticity (i.e., no size effect behaviour). The regularised structure of such arrays also leads to a more uniform and repetitive stress distribution when the models are placed under cantilever bending and uniaxial torsion. This in turn leads to the exhibition of micropolar size effects and in turn a behaviour that contrasts with that obtained in the bovine samples. Such an observation is significant because it further reaffirms that the randomised nature of the trabecular structure within the bovine samples may lead to the anti-micropolar size effects observed in such samples (stiffening effect as the size of the sample increases).

The similarity in size-effect behaviour between the bovine  $\mu$ CT models and the experimental setup is of particular importance in this case because this is the first study that uses a 3D printed analogue material to facilitate testing at an easily achievable scale. The size effect behaviour between finite element,  $\mu$ CT based models and the experimental model further validates the relevance of the models whilst also providing an opportunity for more accurate experimental data collection by using such an experimental setup in conjunction with digital volume correlation (DVC) techniques to further validate finite element models and understand the effect the microstructure of trabecular bone has on the macro-scale behaviour in terms of size-effect characterisation.

There were various studies where bone was assumed to exhibit micropolar behaviour (Ibrahim Goda et al., 2012; Goda et al., 2013a; Ramézani et al., 2012) and as such it was expected that bone would exhibit micropolar behaviour. This coincides with the computer-generated models but contrasts with the bovine samples (both under finite element simulation and under experimental testing). The main reason for this contrast in behaviour can be theorised to be from the randomised structure of struts within trabecular bone. This contrasts with the organised structure in the computer-generated models to such a degree that it affects the size effect behaviour of the overall model. This research shows that there is a possibility that the assumption of trabecular bone exhibiting micropolar behaviour or that it can be modelled using regularised computer-generated arrays may

be inaccurate in nature and may lead to different behaviour both on the micro scale and on the macro scale.

From the analysis of the stress distribution of the models, it can be observed that the magnitude and amount of stress concentrations within the models contribute to the exhibition of micropolar or anti-micropolar size effects. It could be observed that computer generated arrays where stress concentrations were mostly in the same relative locations and small in number contributed to a micropolar size effect exhibition of the overall model. On the other hand, finite element models of the bovine samples consisted of randomised stress concentrations on the thinner struts with stresses having a lower magnitude on thicker trabeculae with a smoother surface texture. It is being theorised that the concentration of stresses on thinner trabeculae causes the model to exhibit a higher overall stiffness. This occurs due to localised yielding and micro-damage within the trabeculae, which causes micromotions of the thinner trabeculae from these stress concentrations. Such stress concentrations would cause micromotions in the material, thus resulting in a higher aggregation of material at certain locations, thus exhibiting a higher stiffness. This would eventually result in a stiffening effect on the macro-scale behaviour of the model. Such an overall increase in stiffness was also observed in the experimental results carried out with the Bose Electroforce (excluding the largest sample due to a defective load cell) and indicates similarities to the behaviour of the bovine finite element models on the macro-scale.

There have also been studies that assume that trabecular bone exhibits micropolar behaviour (Bioengineering Conference Big Sky, 1999; Ibrahim Goda et al., 2012; Goda et al., 2013a; Goda et al., 2013b; Yang & Lakes, 1982) and this research project contradicts such studies in this assumption. This leads to two main questions that need to be asked regarding the behaviour of cancellous bone with respect to size-effects, macro-scale behaviour and micro-scale behaviour; the first question is whether this study is accurate enough to warrant further examination into the creation of further regularised computer-generated models which would mimic the size effect behaviour of trabecular bone. Such structures could potentially include thinner struts together with thicker struts in particular regions. The second question is on whether previous studies have come close enough to accurately understanding how trabecular bone works both in terms of experimentation and in terms of simulation (on the micro-scale).

In the studies mentioning the behaviour of micropolar materials and/or theorising that trabecular bone exhibits micropolar behaviour (Bioengineering Conference Big Sky, 1999; Ibrahim Goda et al.,

2012; Goda et al., 2013a; Goda et al., 2013b; Yang & Lakes, 1982), studies either do not model the micro-scale behaviour of the bone on a trabecular level, or they outright assume that such a model is capable of mimicking the behaviour of trabecular bone. This study differs to these as the micro-scale behaviour is modelled down to the trabecular level and provides a much deeper level of detail. To further validate these models, the micro-scale behaviour can also be observed through experimentation with the Bose Electrofoce machine and these results contrast with what other studies have theorised concerning regularised and computer-generated arrays being capable of modelling trabecular bone down to the micro-scale in terms of size effect behaviour.

The observed behaviour also contrasts with what has been said in literature on the surface finish potentially having an effect on the exhibition of anti-micropolar or micropolar size effects by materials as described by Wheel et al. (Wheel et al., 2015). However, it also raises questions as to the implications from such a size effect behaviour. Wheel et al. (Wheel et al., 2015) also observed similar size effect behaviour when loading samples in bending. However, in this study, the scale of the sample was much larger and anti-micropolar size effect behaviour was attributed to surface finish. There is a small possibility that this could also be the case for the samples tested in this study, however, it must be noted that the effect of surface finish in such samples may be very minimal due to the porous nature of the samples. The theory that micro-motions and trabecular yielding lead to this anti-micropolar size-effect behaviour seems to be more plausible when the stress distribution within the sample is taken into consideration. The results and trend observed from the finite element models and from the experimentally tested samples would suggest that the material would consistently exhibit a stiffening effect as the size of the sample increases. However, this would imply that an infinitesimally large sample should exhibit an infinitesimally large normalised stiffness. This is physically impossible and raises further questions as to what may occur as the size of the sample exceeds the sizes tested within this study.

The general consensus in literature and within this study is that micropolar theory (together with the assumptions made within such a theory), can be used as a good representation of non-continuum solids such as cancellous bone. However, a very important point to take into consideration is whether such assumptions are appropriate for modelling structures with a randomized nature such as cancellous bone. The difference in size effect behavior may also be attributed to the potentially inappropriate assumptions that are made when deriving the basic constitutive equations of micropolar solids. This would mean that a more generalized and complex

non-local theory such as micromorphic theory may possibly be a more accurate representation when modelling size-effect behavior of cancellous bone.

For the samples analysed under in-silico testing conditions, a quadratic mathematical relationship could be found for the observed size effect behaviour with Pearson correlation coefficients of 0.9926, 0.9828, and 0.9926 for compression, torsion and bending respectively as shown in Figure 9.4-Figure 9.6. Such data would also need to be further validated with the use of a material model that is elastic-perfectly plastic together with the use of more samples for further statistical confidence in the mathematical relationship. It would be anticipated that the change of the material model affects the material relationship in terms of constants, however, the relationship would still be represented by a quadratic functions for the samples that are of sizes within the same range of those analysed in this study.

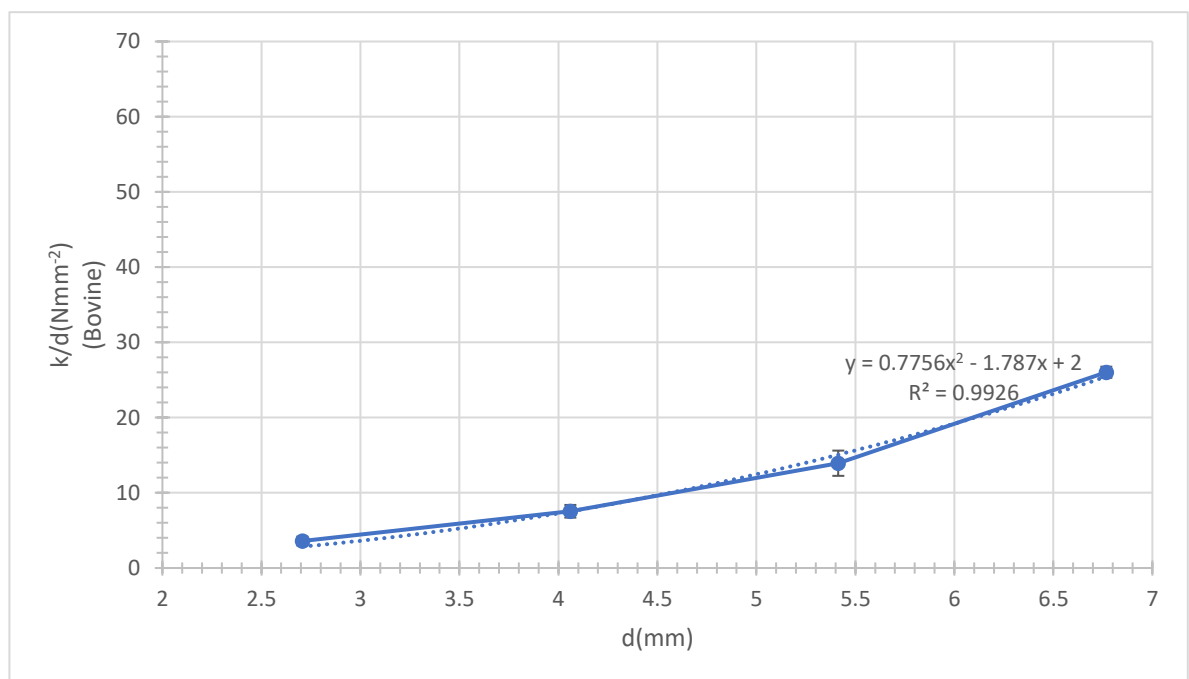


Figure 9.1: Fitting of a quadratic function to the in-silico data for compression testing

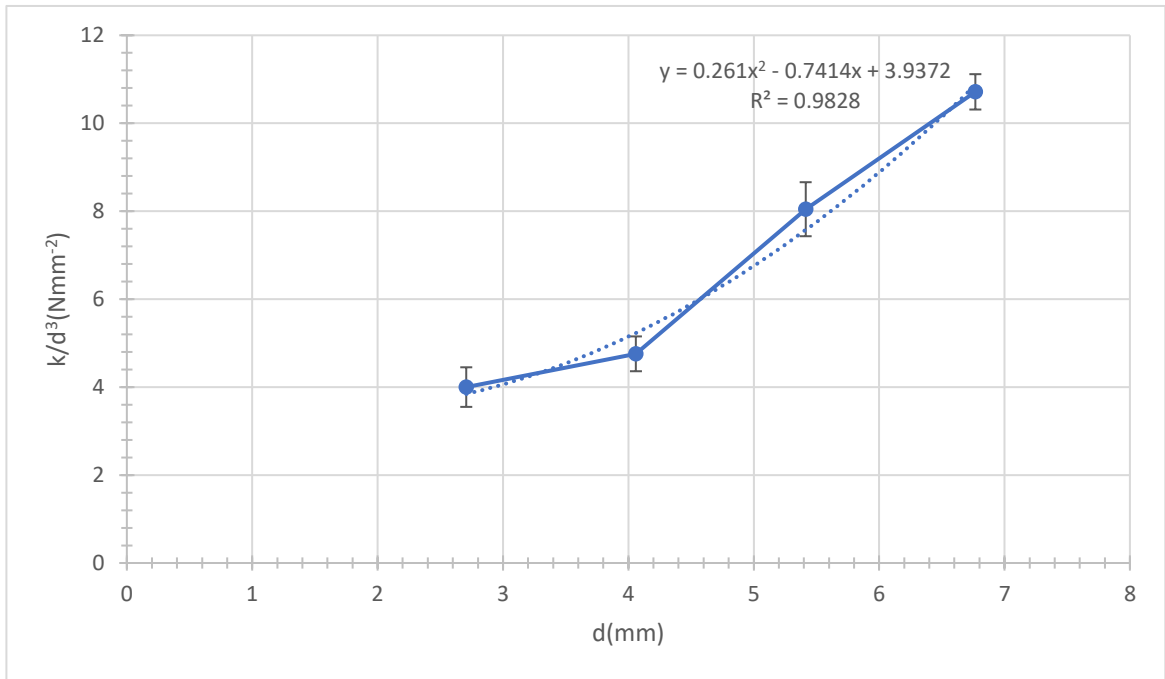


Figure 9.3: Fitting of a quadratic function to the in-silico data for torsion testing

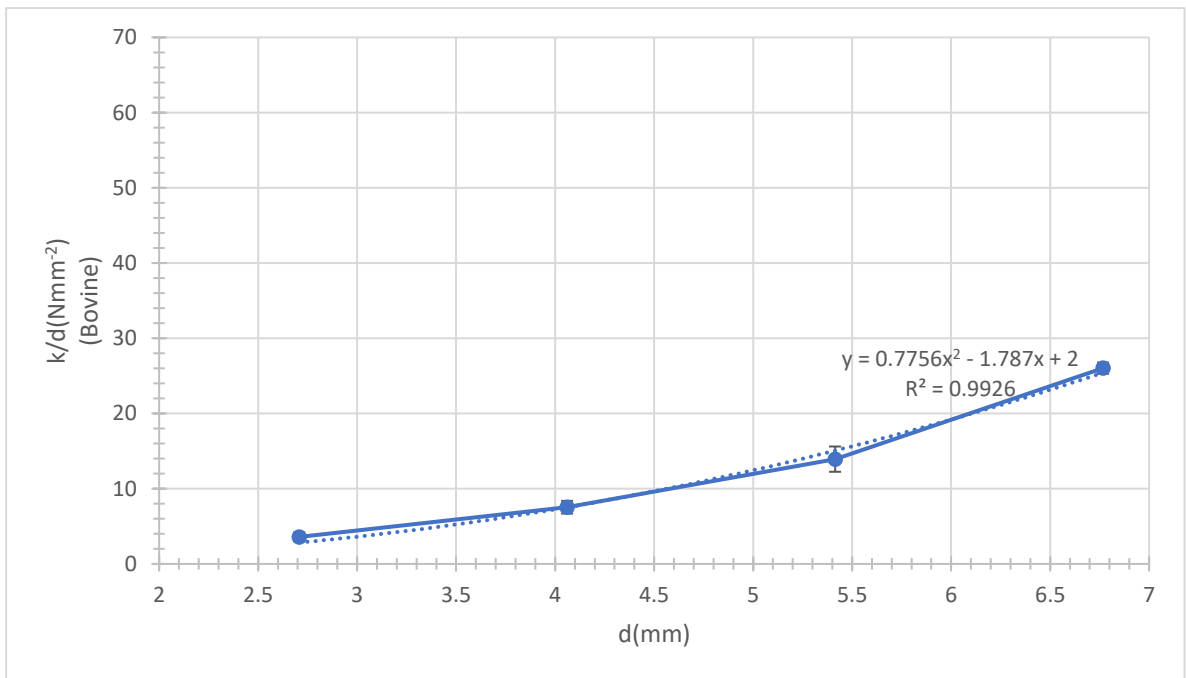


Figure 9.2: Fitting of a quadratic function to the in-silico data for cantilever bending

## 9.2 – Limitations and Further work

The results from this study indicate that other computer-generated models need to be considered for accurately modelling trabecular bone on the micro-scale. Other potential geometries that could be considered could be rod models with a larger degree of perturbations than those that were included in this study, together with variations in diameter along the rod lengths and potentially changes in shape as well. This would more closely represent trabecular bone and would give the model an opportunity to simulate more closely the amount of stress concentrations that were observed in trabecular bone. On the other hand, reproducing the magnitude and locations of these stress concentrations could pose a larger degree of difficulty as the degree of randomisation within trabecular bone might be very hard to mimic.

Something that also needs to be taken into consideration is the degree of smoothing that was applied to the model. As can be noted in Chapter 5, smoothing was applied to a very large degree so that a model that could be meshed was eventually obtained. This level of smoothing sheds some degree of doubt with regards to how close the printed and modelled geometry is to actual trabecular bone. The fact that the printed models tested on the Bose Electroforce machine correlate to a large degree with the behaviour observed under finite element simulation for the same samples are promising. However, this does not necessarily mean that such results are perfectly representative of trabecular bone as in both these cases the geometry had already been smoothed prior to the experiment taking place. A possibility that needs to be taken into consideration is that some of the specks and edges that were smoothed out might have been actual geometry of the bone and that should not have been smoothed to obtain a truly representative geometry. This could have affected the model by reducing the amount of stress concentrations and thus affecting the overall size effect behaviour that could be observed. If the theory being proposed in this study is correct, it can be said that a reduction of smoothing in future studies would result in even more stress concentrations. This would lead to a further accentuation of anti-micropolar size effect behaviour.

The significance of this study relates to structures with a randomised nature such as trabecular bone and foams. The results observed in this study would not be significant in biological structures that have an organised and regular microstructure such as cortical bone amongst others. However, these could pose a large degree of significance in the modelling of foams and other randomised structures amongst others. Further work would have to be carried out to determine whether the theorised behaviour can be verified, finding a mathematical relationship for the anti-micropolar size effect

behaviour and determining micropolar material constants for the micropolar size-effects that are predicted. This could be done by further testing of excised trabecular bone through finite element modelling and in vitro testing. An increase to the accuracy with which trabecular bone can be represented in 3D meshes would also mean that the accuracy of modelling can be increased leading to less room for errors when analysing stress distribution and size effect behaviour in  $\mu$ CT scanned samples. Studies could also be carried out to observe whether the theory being proposed is only representative of trabecular bone or whether it could be used to model any material that has a randomised microstructure such as foams. The use of a more generalized non-local theory such as micromorphic theory for modelling such randomized microstructures could also be investigated. Furthermore, the accuracy of the in-silico models can be increased by using a material model that is inclusive of yielding behaviour. This should exacerbate the exhibition of size effects and lead to a sharper increase in normalised stiffness as the size of the sample increases (for the anti-micropolar region).

Further to the behaviours that are being postulated in **Error! Reference source not found.**, **Error! Reference source not found.** and **Error! Reference source not found.**. It is of critical importance to note that these are predictions based on the data collected and the general trend observed in size effect behaviour together with the understandings of micropolar theory and elastic theory. Further testing would need to be carried out to ascertain such postulations and such testing should include a larger sample size (to provide statistical significance), samples from different anatomical regions, and loading under different loading modes (compression, bending and torsion) for physical samples. Such samples would also ideally be tested on the actual sample rather than on a 3D printed scaled sample to provide a better level of accuracy. Finite element models should also have boundary conditions optimised to match the physical loading conditions whilst also ideally having a larger sample size for testing together with different anatomical regions.

### 9.3 – Conclusion

In conclusion, it can be said that the behaviour observed in this study contrasts with other studies that have been published in the past assuming that bone exhibits micropolar behaviour or that it can be represented by a computer-generated models. This study is highly promising in that the level of accuracy that have been used have never been used in other studies, so it raises questions as to whether other theories that have been used to model trabecular bone are accurately modelling the size effect behaviour of trabecular bone. This study is very promising in that experimental results in

compression have been used to validate the behaviour predicted by finite element models. Such experimental results can also be correlated to what has been observed under finite element simulation, however, further work needs to be done in torsion and bending to further validate these results. There are also questions that can be raised as to whether the level of smoothing affects the model to a large degree (although in this case this was necessary to obtain a model that could be meshed), and it would be interesting to potentially obtain other models with a lower level of smoothing and observe the size effect behaviour in comparison to the models in this study.

Despite that various studies on human trabecular bone have shown that around 90% of stiffness and strength of trabecular bone can be explained/modelled using considerations for density and local material properties of trabecular bone, such models do not take into account size effect behaviour of trabecular bone. The most important conclusion of this study is that it has been shown that trabecular bone does not behave in a manner according to conventional linear elasticity and not even conventional micropolar elasticity where size effect behaviour is concerned. It has been shown through *in silico* loading that the variations in thickness along the trabeculae of trabecular bone and the randomised structure of such trabeculae may contribute to stress concentrations, localised yielding, and micro-damage within the microstructural architecture of cancellous bone. These stress concentrations may lead to micro-motions which eventually lead to an aggregation of material when under load, which in turn may lead to a local stiffening effect. It is being theorised that this results in an anti-micropolar size-effect behaviour at very small length scales such as those observed within this study. The most significant finding within this study is that such behaviour has also been observed and validated through experimental testing in compression and thus it provides a certain level of confidence in the accuracy of these models and in understanding the effect of the microstructural architecture on the macro-scale behaviour of trabecular bone and potentially other similar structures such as foams. Despite all of this, the limited sample sizes and other limitations discussed within this study need to be considered and further investigations need to be carried out. It is theorised that as the size of the sample increases, the effects that the local stiffening effect has on the whole sample decreases, up to a point. After this, it is theorised that micropolar theory becomes more predominant in the size-effect behaviour of cancellous bone, causing the normalised stiffness to decrease again up to an asymptotic value that can be derived using classical elasticity. Such a theory is significant because in this case, it would show that micropolar theory can be applicable to cancellous bone only at certain length scales. At smaller length scales, another theory would need to be applied and the determination of such length scales would be pivotal in modelling

size effect behaviour in cancellous bone. Determining the length scales at which anti-micropolar effects and micropolar effects are more predominant in cancellous bone would also signify that the modelling of cancellous bone could be potentially simplified using mathematical models that model non-continuum models without modelling the micro-architecture of the structure itself. In turn, the modelling of periprosthetic stress and the predictions for aseptic loosening of implants can be made more accurate by using non-continuum mechanics to incorporate size effect behaviour and further increase the accuracy of predictions for aseptic loosening. Incorporating a non-continuum mathematical model of trabecular bone would also increase the ease of modelling by eliminating the need to obtain local properties of trabecular bone at various points since such properties would then be included within the mathematical model that accounts for voids within the structure and variations in mechanical properties.

## 10 References

- Anderson, W. B., & Lakes, R. S. (1994). Size effects due to Cosserat elasticity and surface damage in closed-cell polymethacrylimide foam. *Journal of Materials Science*, 29(24), 6413-6419. <https://doi.org/10.1007/BF00353997>
- Baggi, L., Cappelloni, I., Di Girolamo, M., Maceri, F., & Vairo, G. (2008). The influence of implant diameter and length on stress distribution of osseointegrated implants related to crestal bone geometry: a three-dimensional finite element analysis. *J Prosthet Dent*, 100(6), 422-431. [https://doi.org/10.1016/s0022-3913\(08\)60259-0](https://doi.org/10.1016/s0022-3913(08)60259-0)
- Bakar, N., Saidi, B., & Yamin, L. (2019). Measurement of trabecular bone parameters with different bone thickness and voxel size in mice using micro CT. *Malaysian Journal of Fundamental and Applied Sciences*, 15, 65-68. <https://doi.org/10.11113/mjfas.v15n2019.1128>
- Bauer, T. W., & Schils, J. (1999). The pathology of total joint arthroplasty.II. Mechanisms of implant failure. *Skeletal Radiol*, 28(9), 483-497. <https://doi.org/10.1007/s002560050552>
- Bertoldi, K., Bigoni, D., & Drugan, W. J. (2007). Structural interfaces in linear elasticity. Part I: Nonlocality and gradient approximations. *Journal of the Mechanics and Physics of Solids*, 55, 1-34. <https://doi.org/10.1016/j.jmps.2006.06.004>
- Beveridge, A. (2011). Novel computational methods to predict the deformation of macroscopic heterogeneous materials.
- Beveridge, A. J., Wheel, M., & Nash, D. H. (2010). Computational Modelling and Experimental Characterisation of Heterogeneous Materials.
- Beveridge, A. J., Wheel, M. A., & Nash, D. (2013). The micropolar elastic behaviour of model macroscopically heterogeneous materials. *International Journal of Solids and Structures*, 50, 246–255. <https://doi.org/10.1016/j.ijsolstr.2012.09.023>
- Bioengineering Conference Big Sky, M. (1999). *Micropolar model of trabecular bone* (Vol. 42). American Society of Mechanical Engineers.
- Bravo, A. E., Osnaya, L. C., Ramírez, E. I., Jacobo, V. H., & Ortiz, A. (2019). The effect of bone marrow on the mechanical behavior of porcine trabecular bone. *Biomedical Physics & Engineering Express*, 5(6), 065023. <https://doi.org/10.1088/2057-1976/ab4dc0>
- Brezny, R., & Green, D. (1990). Characterization of edge effects in cellular materials. *Journal of Materials Science*, 25(11), 4571-4578.
- Buccino F, Colombo C, Vergani LM. A Review on Multiscale Bone Damage: From the Clinical to the Research Perspective. *Materials*. 2021; 14(5):1240. <https://doi.org/10.3390/ma14051240>

- Buechner, P. M., & Lakes, R. S. (2003). Size effects in the elasticity and viscoelasticity of bone. *Biomechanics and Modeling in Mechanobiology*, 1(4), 295-301. <https://doi.org/10.1007/s10237-002-0026-8>
- Choi, K., Kuhn, J. L., Ciarelli, M. J., & Goldstein, S. A. (1990). The elastic moduli of human subchondral, trabecular, and cortical bone tissue and the size-dependency of cortical bone modulus. *Journal of Biomechanics*, 23(11), 1103-1113. [https://doi.org/https://doi.org/10.1016/0021-9290\(90\)90003-L](https://doi.org/https://doi.org/10.1016/0021-9290(90)90003-L)
- Clarke, B. (2008). Normal bone anatomy and physiology. *Clin J Am Soc Nephrol*, 3 Suppl 3(Suppl 3), S131-139. <https://doi.org/10.2215/cjn.04151206>
- Cristofolini, L., Juszczak, M., Taddei, F., & Viceconti, M. (2009). Strain distribution in the proximal human femoral metaphysis. *Proc Inst Mech Eng H*, 223(3), 273-288. <https://doi.org/10.1243/09544119jeim497>
- Dagenais, S., Garbedian, S., & Wai, E. K. (2009). Systematic review of the prevalence of radiographic primary hip osteoarthritis. *Clin Orthop Relat Res*, 467(3), 623-637. <https://doi.org/10.1007/s11999-008-0625-5>
- Dall'Ara, E., Luisier, B., Schmidt, R., Kainberger, F., Zysset, P., & Pahr, D. (2013). A nonlinear QCT-based finite element model validation study for the human femur tested in two configurations in vitro. *Bone*, 52(1), 27-38. <https://doi.org/10.1016/j.bone.2012.09.006>
- Dall'Ara, E., Pahr, D., Varga, P., Kainberger, F., & Zysset, P. (2012). QCT-based finite element models predict human vertebral strength in vitro significantly better than simulated DEXA. *Osteoporosis International*, 23(2), 563-572. <https://doi.org/10.1007/s00198-011-1568-3>
- Dall'Ara, E., Peña-Fernández, M., Palanca, M., Giorgi, M., Cristofolini, L., & Tozzi, G. (2017). Precision of Digital Volume Correlation Approaches for Strain Analysis in Bone Imaged with Micro-Computed Tomography at Different Dimensional Levels [Original Research]. *Frontiers in Materials*, 4. <https://doi.org/10.3389/fmats.2017.00031>
- Daszkiewicz, K., Maquer, G., & Zysset, P. (2017). The effective elastic properties of human trabecular bone may be approximated using micro finite element analyses of embedded volume elements. *Biomechanics and Modeling in Mechanobiology*, 16. <https://doi.org/10.1007/s10237-016-0849-3>
- Davies, A. P., Vince, A. S., Shepstone, L., Donell, S. T., & Glasgow, M. M. (2002). The radiologic prevalence of patellofemoral osteoarthritis. *Clin Orthop Relat Res*(402), 206-212. <https://doi.org/10.1097/00003086-200209000-00020>

- Della Rocca, G. J., Leung, K. S., & Pape, H. C. (2011). Periprosthetic fractures: epidemiology and future projections. *J Orthop Trauma*, 25 Suppl 2, S66-70. <https://doi.org/10.1097/BOT.0b013e31821b8c28>
- Dyson, E. D., & Whitehouse, W. J. (1968). Composition of trabecular bone in children and its relation to radiation dosimetry. *Nature*, 217(5128), 576-578. <https://doi.org/10.1038/217576a0>
- Eringen, A. C. (1966). Linear Theory of Micropolar Elasticity. *Journal of Mathematics and Mechanics*, 15(6), 909-923. <http://www.jstor.org/stable/24901442>
- Felson, D. T., Naimark, A., Anderson, J., Kazis, L., Castelli, W., & Meenan, R. F. (1987). The prevalence of knee osteoarthritis in the elderly. The Framingham Osteoarthritis Study. *Arthritis Rheum*, 30(8), 914-918. <https://doi.org/10.1002/art.1780300811>
- Forest, S., Barbe, F., & Cailletaud, G. (2000). Cosserat modelling of size effects in the mechanical behavior of polycrystals and multi-phase materials. *International Journal of Solids and Structures*, 37, 7105-7126. [https://doi.org/10.1016/S0020-7683\(99\)00330-3](https://doi.org/10.1016/S0020-7683(99)00330-3)
- Frost, H. M. (1994). Wolff's Law and bone's structural adaptations to mechanical usage: an overview for clinicians. *Angle Orthod*, 64(3), 175-188. [https://doi.org/10.1043/0003-3219\(1994\)064<0175:Wlabsa>2.0.Co;2](https://doi.org/10.1043/0003-3219(1994)064<0175:Wlabsa>2.0.Co;2)
- Gauthier, R. D., & Jahsman, W. E. (1975). A Quest for Micropolar Elastic Constants. *Journal of Applied Mechanics*, 42(2), 369-374. <https://doi.org/10.1115/1.3423583>
- Gitman, I. M. (2012). Anisotropic gradient elasticity for modelling bone tissue. *Computational Materials Science*, 52(1), 136-138. <https://doi.org/https://doi.org/10.1016/j.commatsci.2011.06.022>
- Goda, I., Assidi, M., Belouettar, S., & Ganghoffer, J.-F. (2012). A micropolar anisotropic constitutive model of cancellous bone from discrete homogenization. *Journal of the mechanical behavior of biomedical materials*, 16C, 87-108. <https://doi.org/10.1016/j.jmbbm.2012.07.012>
- Goda, I., Assidi, M., & Ganghoffer, J.-F. (2013a). A 3D elastic micropolar model of vertebral trabecular bone from lattice homogenization of the bone microstructure. *Biomechanics and Modeling in Mechanobiology*, 13. <https://doi.org/10.1007/s10237-013-0486-z>
- Goda, I., Assidi, M., & Ganghoffer, J.-F. (2013b). Cosserat Anisotropic Models of Trabecular Bone from the Homogenization of the Trabecular Structure: 2D and 3D Frameworks. In H. Altenbach, S. Forest, & A. Krivtsov (Eds.), *Generalized Continua as Models for Materials: with*

- Multi-scale Effects or Under Multi-field Actions* (pp. 111-141). Springer Berlin Heidelberg.  
[https://doi.org/10.1007/978-3-642-36394-8\\_7](https://doi.org/10.1007/978-3-642-36394-8_7)
- Goda, I., Assidi, M., & Ganghoffer, J. F. (2012). Cosserat 3D anisotropic models of trabecular bone from the homogenisation of the trabecular structure. *Computer Methods in Biomechanics and Biomedical Engineering*, 15(sup1), 288-290.  
<https://doi.org/10.1080/10255842.2012.713645>
- Gong, J. K., Arnold, J. S., & Cohn, S. H. (1964). COMPOSITION OF TRABECULAR AND CORTICAL BONE. *Anat Rec*, 149, 325-331. <https://doi.org/10.1002/ar.1091490303>
- Gøthesen, O., Espehaug, B., Havelin, L., Petursson, G., Lygre, S., Ellison, P., Hallan, G., & Furnes, O. (2013). Survival rates and causes of revision in cemented primary total knee replacement: a report from the Norwegian Arthroplasty Register 1994-2009. *Bone Joint J*, 95-b(5), 636-642.  
<https://doi.org/10.1302/0301-620x.95b5.30271>
- Grotle, M., Hagen, K. B., Natvig, B., Dahl, F. A., & Kvien, T. K. (2008). Prevalence and burden of osteoarthritis: results from a population survey in Norway. *J Rheumatol*, 35(4), 677-684.
- Guha I, Zhang X, Rajapakse CS, Chang G, Saha PK. Finite element analysis of trabecular bone microstructure using CT imaging and continuum mechanical modeling. *Med Phys*. 2022 Jun;49(6):3886-3899. doi: 10.1002/mp.15629. Epub 2022 Apr 5. PMID: 35319784; PMCID: PMC9325403.
- Guillén T, Zhang QH, Tozzi G, Ohrndorf A, Christ HJ, Tong J. (2011). Compressive behaviour of bovine cancellous bone and bone analogous materials, microCT characterisation and FE analysis. *J Mech Behav Biomed Mater*, 4(7), 1452-1461.
- Hogan, H. A. (1992). Micromechanics modeling of Haversian cortical bone properties. *J Biomech*, 25(5), 549-556. [https://doi.org/10.1016/0021-9290\(92\)90095-i](https://doi.org/10.1016/0021-9290(92)90095-i)
- Huiskes, R. (1990). The various stress patterns of press-fit, ingrown, and cemented femoral stems. *Clin Orthop Relat Res*(261), 27-38.
- Klein-Nulend, J., Bakker, A. D., Bacabac, R. G., Vatsa, A., & Weinbaum, S. (2013). Mechanosensation and transduction in osteocytes. *Bone*, 54(2), 182-190.  
<https://doi.org/10.1016/j.bone.2012.10.013>
- Ko, C. C., Douglas, W. H., & Cheng, Y. S. (1995). Intrinsic mechanical competence of cortical and trabecular bone measured by nanoindentation and microindentation probes.
- Lakes, R. (1986). Experimental microelasticity of two porous solids. *International Journal of Solids and Structures*, 22(1), 55-63.

- Lakes, R. S. (1983). Size effects and micromechanics of a porous solid. *Journal of Materials Science*, 18(9), 2572-2580.
- Lakes, R. S. (1995). EXPERIMENTAL METHODS FOR STUDY OF COSSERAT ELASTIC SOLIDS AND OTHER GENERALIZED ELASTIC CONTINUA.
- Lim, T.-H., & Hong, J. H. (2000). Poroelastic properties of bovine vertebral trabecular bone [https://doi.org/10.1002/jor.1100180421]. *Journal of Orthopaedic Research*, 18(4), 671-677. https://doi.org/https://doi.org/10.1002/jor.1100180421
- McNamara, L. M., Van der Linden, J. C., Weinans, H., & Prendergast, P. J. (2006). Stress-concentrating effect of resorption lacunae in trabecular bone. *J Biomech*, 39(4), 734-741. https://doi.org/10.1016/j.jbiomech.2004.12.027
- McPhee S, Kershaw LE, Daniel CR, Peña Fernández M, Cillán-García E, Taylor SE, Wolfram U. QCT-based computational bone strength assessment updated with MRI-derived 'hidden' microporosity. *J Mech Behav Biomed Mater*. 2023 Nov;147:106094. doi: 10.1016/j.jmbbm.2023.106094. Epub 2023 Aug 28. PMID: 37741181.
- Müller R, Rügsegger P. Micro-tomographic imaging for the nondestructive evaluation of trabecular bone architecture. *Stud Health Technol Inform*. 1997;40:61-79. PMID: 10168883.
- Mys, K., Varga, P., Stockmans, F., Gueorguiev, B., Wyers, C. E., van den Bergh, J. P. W., & van Lenthe, G. H. Quantification of 3D microstructural parameters of trabecular bone is affected by the analysis software. *Bone*, 142, 2021 Article 115653. https://doi.org/10.1016/j.bone.2020.115653
- Pabst, W. (2005). Micropolar materials. *Ceramics - Silikaty*, 49, 170-180.
- Park, H., & Lakes, R. (1986). Cosserat micromechanics of human bone: strain redistribution by a hydration sensitive constituent. *Journal of Biomechanics*, 19(5), 385-397.
- Patterson-Kane, J. C., & Firth, E. C. (2014). CHAPTER 13 - Tendon, ligament, bone, and cartilage: Anatomy, physiology, and adaptations to exercise and training. In D. R. Hodgson, K. H. McKeever, & C. M. McGowan (Eds.), *The Athletic Horse (Second Edition)* (pp. 202-242). W.B. Saunders. https://doi.org/https://doi.org/10.1016/B978-0-7216-0075-8.00022-8
- Peyrin F, Salome M, Cloetens P, Laval-Jeantet AM, Ritman E, Rügsegger P. Micro-CT examinations of trabecular bone samples at different resolutions: 14, 7 and 2 micron level. *Technol Health Care*. 1998 Dec;6(5-6):391-401. PMID: 10100941.

- Quintana, J. M., Arostegui, I., Escobar, A., Azkarate, J., Goenaga, J. I., & Lafuente, I. (2008). Prevalence of knee and hip osteoarthritis and the appropriateness of joint replacement in an older population. *Arch Intern Med*, *168*(14), 1576-1584. <https://doi.org/10.1001/archinte.168.14.1576>
- Ramézani, H., El-Hraiech, A., Jeong, J., & Benhamou, C.-L. (2012). Size effect method application for modeling of human cancellous bone using geometrically exact Cosserat elasticity. *Computer methods in applied mechanics and engineering*, *237-240*, 227-243. <https://doi.org/https://doi.org/10.1016/j.cma.2012.05.002>
- Rho, J. Y., Ashman, R. B., & Turner, C. H. (1993). Young's modulus of trabecular and cortical bone material: Ultrasonic and microtensile measurements. *Journal of Biomechanics*, *26*(2), 111-119. [https://doi.org/https://doi.org/10.1016/0021-9290\(93\)90042-D](https://doi.org/https://doi.org/10.1016/0021-9290(93)90042-D)
- Rho, J. Y., Roy, M. E., 2nd, Tsui, T. Y., & Pharr, G. M. (1999). Elastic properties of microstructural components of human bone tissue as measured by nanoindentation. *J Biomed Mater Res*, *45*(1), 48-54. [https://doi.org/10.1002/\(sici\)1097-4636\(199904\)45:1](https://doi.org/10.1002/(sici)1097-4636(199904)45:1)
- Roy, M., Rho, J. Y., Tsui, T. Y., & Pharr, G. M. (1996). Variation of Young's modulus and hardness in human lumbar vertebrae measured by nanoindentation. *ASME-PUBLICATIONS-BED*, *33*, 385-386.
- Sabet, F. A., Jin, O., Koric, S., & Jasiuk, I. (2017). Nonlinear micro-CT based FE modeling of trabecular bone-Sensitivity of apparent response to tissue constitutive law and bone volume fraction. *International Journal for Numerical Methods in Biomedical Engineering*, *34*(4), e2941. <https://doi.org/doi:10.1002/cnm.2941>
- Sandino, C., McErlain David, D., Schipilow, J., & Boyd Steven, K. Estimation of the Poroelastic Properties of Trabecular Bone at the Microscopic Scale Using CT Based FE Models. *Poromechanics V*, 1107-1112. <https://doi.org/doi:10.1061/9780784412992.132>
- Sathappan, S. S., Pang, H. N., Manoj, A., Ashwin, T., & Satku, K. (2009). Does stress shielding occur with the use of long-stem prosthesis in total knee arthroplasty? *Knee Surg Sports Traumatol Arthrosc*, *17*(2), 179-183. <https://doi.org/10.1007/s00167-008-0649-0>
- Silva, A. M. H. d., Alves, J. M., Silva, O. L. d., & Silva Junior, N. F. d. (2014). Two and three-dimensional morphometric analysis of trabecular bone using X-ray microtomography ( $\mu$ CT). *Revista Brasileira de Engenharia Biomédica*, *30*, 93-101. [http://old.scielo.br/scielo.php?script=sci\\_arttext&pid=S1517-31512014000200002&nrm=iso](http://old.scielo.br/scielo.php?script=sci_arttext&pid=S1517-31512014000200002&nrm=iso)

- Stefanek P, Synek A, Dall'Ara E, Pahr DH. Comparison of linear and nonlinear stepwise  $\mu$ FE displacement predictions to digital volume correlation measurements of trabecular bone biopsies. *J Mech Behav Biomed Mater.* 2023 Feb;138:105631. doi: 10.1016/j.jmbbm.2022.105631. Epub 2022 Dec 22. PMID: 36592570.
- Townsend, P. R., Rose, R. M., & Radin, E. L. (1975). Buckling studies of single human trabeculae. *J Biomech*, 8(3-4), 199-201. [https://doi.org/10.1016/0021-9290\(75\)90025-1](https://doi.org/10.1016/0021-9290(75)90025-1)
- Turner, C. H., Rho, J., Takano, Y., Tsui, T. Y., & Pharr, G. M. (1999). The elastic properties of trabecular and cortical bone tissues are similar: results from two microscopic measurement techniques. *J Biomech*, 32(4), 437-441. [https://doi.org/10.1016/s0021-9290\(98\)00177-8](https://doi.org/10.1016/s0021-9290(98)00177-8)
- Waseem, A., Beveridge, A. J., Wheel, M. A., & Nash, D. (2013). The influence of void size on the micropolar constitutive properties of model heterogeneous materials. *European Journal of Mechanics - A/Solids*, 40, 148–157. <https://doi.org/10.1016/j.euromechsol.2013.01.002>
- Wheel, M. A., Frame, J. C., & Riches, P. E. (2015). Is smaller always stiffer? On size effects in supposedly generalised continua. *International Journal of Solids and Structures*, 67-68, 84-92. <https://doi.org/https://doi.org/10.1016/j.ijsolstr.2015.03.026>
- Yang, J., & Lakes, R. S. (1982). Experimental study of micropolar and couple stress elasticity in compact bone in bending. *Journal of Biomechanics*, 15(2), 91-98.
- Zysset, P. K., Dall'ara, E., Varga, P., & Pahr, D. H. (2013). Finite element analysis for prediction of bone strength. *BoneKEy reports*, 2, 386-386. <https://doi.org/10.1038/bonekey.2013.120>
- Zysset, P. K., Guo, X. E., Hoffler, C. E., Moore, K. E., & Goldstein, S. A. (1999). Elastic modulus and hardness of cortical and trabecular bone lamellae measured by nanoindentation in the human femur. *J Biomech*, 32(10), 1005-1012. [https://doi.org/10.1016/s0021-9290\(99\)00111-6](https://doi.org/10.1016/s0021-9290(99)00111-6)

11 Appendices

## Appendix 1 – ANSYS script used for compression of bovine samples

```
/clear
/input,5x5x10_1cleaned,cdb      !importing the CDB file
/prep7
L=13.5344745                    !define the total length of the sample (this was varied according to the length of the sample so the strain remains constant for every size)
*get,maxx,node,,mxloc,x        !retrieve maximum x-position
*get,maxy,node,,mxloc,y        !retrieve maximum y-position
*get,maxz,node,,mxloc,z        !retrieve maximum z-position
*get,minx,node,,mnloc,x        !retrieve minimum x-position
*get,miny,node,,mnloc,y        !retrieve minimum y-position
*get,minz,node,,mnloc,z        !retrieve minimum z-position

*get,nmax,node,,num,max        !get highest node number

!Material properties
mpdel,all,all                   !delete material properties exported from 3-matic and CTAn
mp,ex,1,12e3                    !new material properties
mp,prxy,1,0.3

allsel
seltol,0.03                     !set the selection tolerance to 0.03mm

nselect,s,loc,z,minz            !selecting the face parallel to z-direction at the fixed end
d,all,uz,0                      !setting boundary conditions at the selected face for a fixed face
allsel

nselect,s,loc,x,minx            !selecting the face parallel to x-direction at the fixed end
d,all,ux,0                      !setting boundary conditions at the selected face for a fixed face
allsel

nselect,s,loc,y,miny            !selecting the face parallel to y-direction at the fixed end
d,all,uy,0                      !setting boundary conditions at the selected face for a fixed face
allsel

nselect,s,loc,z,maxz            !selecting the face parallel to z-direction at the loaded end
d,all,uz,-L/1000                !setting boundary conditions at the selected face for predefined displacement
allsel

/solu
solve
save
finish

/post1
etable,sene,sene                ! Retrieve strain energy per element
ssum                            ! Sum strain energy from ETABLE
*GET,my_Energy,SSUM,0,Item1,SENE ! Gets SENE from ETABLE and defines it as "my_Energy"
```

## Appendix 2 – ANSYS script used for cantilever bending of bovine samples

```

/clear
/input,2x2x4_1cleaned,cdb
/prep7
*get,maxx,node,,mxloc,x           !retrieve maximum x-position
*get,maxy,node,,mxloc,y           !retrieve maximum y-position
*get,maxz,node,,mxloc,z           !retrieve maximum z-position
*get,minx,node,,mnloc,x           !retrieve minimum x-position
*get,miny,node,,mnloc,y           !retrieve minimum y-position
*get,minz,node,,mnloc,z           !retrieve minimum z-position

*get,nmax,node,,num,max           !get highest node number

!Material properties
mpdel,all,all                     !delete material properties exported from 3-matic and CTAn
mp,ex,1,12e3                      !new material properties
mp,prxy,1,0.3

et,2,mass21                       !creating a mass element so that master nodes can have this element type
r,2,1,1,1,1,1

n,nmax+1,minx+((maxx-minx)/2),miny+((maxy-miny)/2),minz-0.05           !master node for the fixed face
Type,2
Real,2
E,nmax+1

n,nmax+2,minx+((maxx-minx)/2),miny+((maxy-miny)/2),maxz+0.05           !master node for the loaded face
Type,2
Real,2
E,nmax+2

!allsel
!selecting the corner node for fixed B.C.s so that the object does not move
!seltol,0.0001
!seltol
!nsel,s,loc,z,(maxz-minz)/2
!*get,maxyy,node,,mxloc,y           !retrieve maximum y-position from the currently selected set
!nsel,r,loc,y,maxyy
!*get,maxxx,node,,mxloc,x           !retrieve maximum y-position from the currently selected set
!nsel,r,loc,x,maxxx

!B.C.s for the fixed node
!d,all,uz,0

allsel
seltol,0.03                       !set the selection tolerance to 0.03mm

nsel,s,loc,z,minz                 !creating constraint equations at the fixed end to allow warping of the face
nsel,a,node,,nmax+1
cerig,nmax+1,all,all

allsel

nsel,s,loc,z,maxz                 !creating constraint equations at the loaded end
nsel,a,node,,nmax+2
cerig,nmax+2,all,uy

allsel
d,nmax+1,all,0                   !master node B.C.s for the fixed end
!dlist

dy=0.05                           !displacement in mm
d,nmax+2,uy,dy                   !displacing the master node at the end
allsel
!dlist

!mpchg,1,all                       !assign material properties to all elements

/solu
solve
save
finish

/post1
etable,sene,sene                 ! Retrieve strain energy per element
ssum                             ! Sum strain energy from ETABLE
*GET,my_Energy,SSUM,0,Item1,SENE ! Gets SENE from ETABLE and defines it as "my_Energy"

```

## Appendix 3 – ANSYS script used for torsion of bovine samples

```

/clear
/input,4x4x8_10cleaned,cdb           !importing the CDB file
/prep7
*get,maxx,node,,mxloc,x             !retrieve maximum x-position
*get,maxy,node,,mxloc,y             !retrieve maximum y-position
*get,maxz,node,,mxloc,z             !retrieve maximum z-position
*get,minx,node,,mnloc,x             !retrieve minimum x-position
*get,miny,node,,mnloc,y             !retrieve minimum y-position
*get,minz,node,,mnloc,z             !retrieve minimum z-position

*get,nmax,node,,num,max              !get highest node number

!Material properties
mpdel,all,all                        !delete material properties exported from 3-matic and CTAn
mp,ex,1,12e3                          !new material properties
mp,prxy,1,0.3

et,2,mass21                          !creating a mass element so that master nodes can have this element type
r,2,1,1,1,1,1

n,nmax+1,minx+((maxx-minx)/2),miny+((maxy-miny)/2),minz-0.05           !master node for the fixed face
Type,2
Real,2
E,nmax+1

n,nmax+2,minx+((maxx-minx)/2),miny+((maxy-miny)/2),maxz+0.05           !master node for the loaded face
Type,2
Real,2
E,nmax+2

!allsel
!selecting the corner node for fixed B.C.s so that the object does not move
!seltol,0.0001
!seltol
!nsel,s,loc,z,(maxz-minz)/2
!*get,maxyy,node,,mxloc,y           !retrieve maximum y-position from the currently selected set
!nsel,r,loc,y,maxyy
!*get,maxxx,node,,mxloc,x           !retrieve maximum y-position from the currently selected set
!nsel,r,loc,x,maxxx

!B.C.s for the fixed node
!d,all,uz,0

allsel
seltol,0.03                          !set the selection tolerance to 0.03mm

nsel,s,loc,z,minz                      !creating constraint equations at the fixed end to allow warping of the face
nsel,a,node,,nmax+1
cerig,nmax+1,all,uy,ux

allsel

nsel,s,loc,z,maxz                      !creating constraint equations at the loaded end
nsel,a,node,,nmax+2
cerig,nmax+2,all,uy,ux

allsel
d,nmax+1,all,0                          !master node B.C.s for the fixed end
!dlist

theta=0.05                             !angle of twist in radians
d,nmax+2,ux,0
d,nmax+2,uy,0
d,nmax+2,uz,0
d,nmax+2,rotz,theta                    !master node torsion for the loaded end
!allsel
!dlist

!mpchg,1,all                            !assign material properties to all elements

/solu
solve
save
finish

/post1
etable,sene,sene                        ! Retrieve strain energy per element
ssum                                    ! Sum strain energy from ETABLE
*GET,my_Energy,SSUM,0,Item1,SENE       ! Gets SENE from ETABLE and defines it as "my_Energy"

```

## Appendix 4 – ANSYS script used for creation and compression of the regular cross array

```

/filename,regularcompression2x2x4,1
/prep7 !Enter preprocessor

!Defining lengths for points
Lh=1.35344745 !Lh defined in mm
Lv=1.35344745 !Lv defined in mm
!points
k,1,0,0,0
k,2,Lv/2,0,0
k,3,0,Lv/2,0
k,4,-Lv/2,0,0
k,5,0,-Lv/2,0
k,6,0,0,Lh/2
k,7,0,0,-Lh/2

!create lines
*do,i,2,7,1
l,i,i
*enddo

rv=0.1626338581 !Radius in mm
rh=0.1626338581 !Radius in mm

!Additional points for defining circles out of the working plane
k,8,-Lv/2,0,rh
k,9,0,Lv/2,rh

!creating thick cylinders
circle,6,rv
al,7,8,9,10
vdrag,1,,,,,5,6

!creating thin cylinders
circle,4,rh,1,8
al,27,28,29,30
vdrag,12,,,,,3,1

circle,3,rh,1,9
al,47,48,49,50
vdrag,23,,,,,2,4

vadd,all !combine all volumes into one volume
numcmp,all

!Material properties
mp,ex,,12e3
mp,prxy,,0.3

et,,solid185
esize,rh/3
MSHKEY,0 !use free meshing
MSHAPE,1,3d !use triangular elements
vmesh,all !mesh volume

!Create (K)x(L)x(M) array
K=2
L=2
M=4

vgen,K,1,,,lv
nummrg,all
numcmp,all

VGEN,L,1,K,1,,lv
nummrg,all
numcmp,all

VGEN,M,1,K*L,1,,lh
nummrg,all
numcmp,all

/NERR,,,-1 !ignore warning/error messages

!Compression loading (Loads and B.C.s)
asel,s,loc,z,-lv/2
da,all,uz,0

asel,s,loc,y,-lv/2
da,all,uy,0

asel,s,loc,x,-lv/2
da,all,ux,0

allsel

asel,s,loc,z,(2*M-1)*lv/2
da,all,uz,-0.001*Lh*(M)

allsel

/solu
solve
save
finish

/post1
etable,sene,sene ! Retrieve strain energy per element
ssum ! Sum strain energy from ETABLE
*GET,my_Energy,SSUM,0,Item1,SENE ! Gets SENE from ETABLE and defines it as "my_Energy"

```

## Appendix 5 – ANSYS script used for creation and torsion of the regular cross array

```

/filename,regular_5x5x10_torsion,1
/prep7 !Enter preprocessor

A=60
!Defining lengths for points
!Lh=(13.74*A+288)*1e-3 !Lh defined in mm
Lh=1.35344745 !Lh defined in mm
!Lv=(6.74*A+456)*1e-3 !Lv defined in mm
Lv=1.35344745 !Lv defined in mm
!points
k,1,0,0,0
k,2,Lv/2,0,0
k,3,0,Lv/2,0
k,4,-Lv/2,0,0
k,5,0,-Lv/2,0
k,6,0,0,Lh/2
k,7,0,0,-Lh/2

!create lines
*do,i,2,7,1
l,1,i
*enddo

!rv=((0.14*A+208)*1e-3)/2 !Radius in mm
rv=0.1626338581 !Radius in mm
!rh=(-1.03*A+189)*1e-3)/2 !Radius in mm
rh=0.1626338581 !Radius in mm

!Additional points for defining circles out of the working plane
k,8,-Lv/2,0,rh
k,9,0,Lv/2,rh

!creating thick cylinders
circle,6,rv
al,7,8,9,10
vdrag,1,,,,,5,6

!creating thin cylinders
circle,4,rh,1,8
al,27,28,29,30
vdrag,12,,,,,3,1

circle,3,rh,1,9
al,47,48,49,50
vdrag,23,,,,,2,4

vadd,all !combine all volumes into one volume
numcmp,all

!Material properties
mp,ex,,12e3
mp,prxy,,0.3

et,,solid185
esize,rh/3
MSHKEY,0 !use free meshing
MSHAPE,1,3d !use triangular elements
vmesh,all !mesh volume

```

```

!Create (K)x(L)x(M) array
K=5
L=5
M=10

vgen,K,1,,lv
nummrg,all
numcmp,all

VGEN,L,1,K,1,,lv
nummrg,all
numcmp,all

VGEN,M,1,K*L,1,,lh
nummrg,all
numcmp,all

/NERR,,,-1          !ignore warning/error messages

!Torsion loading (Loads and B.C.s)
*get,maxx,node,,mxloc,x          !retrieve maximum x-position
*get,maxy,node,,mxloc,y          !retrieve maximum y-position
*get,maxz,node,,mxloc,z          !retrieve maximum z-position
*get,minx,node,,mnloc,x          !retrieve minimum x-position
*get,miny,node,,mnloc,y          !retrieve minimum y-position
*get,minz,node,,mnloc,z          !retrieve minimum z-position

*get,nmax,node,,num,max          !get highest node number

!Material properties
mpdel,all,all                    !delete material properties exported from 3-matic and CTAn
mp,ex,1,12e3                      !new material properties
mp,prxy,1,0.3

et,2,mass21                        !creating a mass element so that master nodes can have this element type
r,2,1,1,1,1

n,nmax+1,minx+((maxx-minx)/2),miny+((maxy-miny)/2),minz-0.05          !master node for the fixed face
Type,2
Real,2
E,nmax+1

n,nmax+2,minx+((maxx-minx)/2),miny+((maxy-miny)/2),maxz+0.05          !master node for the loaded face
Type,2
Real,2
E,nmax+2

allsel

nsel,s,loc,z,minz                  !creating constraint equations at the fixed end to allow warping of the face
nsel,a,node,,nmax+1
cerig,nmax+1,all,uy,ux

allsel

nsel,s,loc,z,maxz                  !creating constraint equations at the loaded end
nsel,a,node,,nmax+2
cerig,nmax+2,all,uy,ux

allsel
d,nmax+1,all,0                    !master node B.C.s for the fixed end
!dlist

theta=0.05                          !angle of twist in radians
d,nmax+2,ux,0
d,nmax+2,uy,0
d,nmax+2,uz,0
d,nmax+2,rotz,theta                !master node torsion for the loaded end
allsel
!dlist

!mpchg,1,all                       !assign material properties to all elements

/solu
solve
save
finish

/post1
etable,sene,sene                    ! Retrieve strain energy per element
ssum                                ! Sum strain energy from ETABLE
*GET,my_Energy,SSUM,0,Item1,SENE    ! Gets SENE from ETABLE and defines it as "my_Energy"

```

## Appendix 6 – ANSYS script used for creation and cantilever bending of the regular cross array

```
/filename,regular_5x5x10_bending,1
/prep7 !Enter preprocessor

!Defining lengths for points
Lh=1.35344745 !Lh defined in mm
Lv=1.35344745 !Lv defined in mm
!points
k,1,0,0,0
k,2,Lv/2,0,0
k,3,0,Lv/2,0
k,4,-Lv/2,0,0
k,5,0,-Lv/2,0
k,6,0,0,Lh/2
k,7,0,0,-Lh/2

!create lines
*do,i,2,7,1
l,1,i
*enddo

rv=0.1626338581 !Radius in mm
rh=0.1626338581 !Radius in mm

!Additional points for defining circles out of the working plane
k,8,-Lv/2,0,rh
k,9,0,Lv/2,rh

!creating thick cylinders
circle,6,rv
al,7,8,9,10
vdrag,1,,,,,5,6

!creating thin cylinders
circle,4,rh,1,8
al,27,28,29,30
vdrag,12,,,,,3,1

circle,3,rh,1,9
al,47,48,49,50
vdrag,23,,,,,2,4

vadd,all !combine all volumes into one volume
numcmp,all

!Material properties
mp,ex,,12e3
mp,prxy,,0.3

et,,solid185
esize,rh/3
MSHKEY,0 !use free meshing
MSHAPE,1,3d !use triangular elements
vmesh,all !mesh volume

!Create (K)x(L)x(M) array
K=5
L=5
M=10

vgen,K,1,,lv
nummrg,all
numcmp,all

VGEN,L,1,K,1,,lv
nummrg,all
numcmp,all

VGEN,M,1,K*L,1,,lh
nummrg,all
numcmp,all

/!NERR,,,-1 !ignore warning/error messages

!Torsion loading (Loads and B.C.s)
asel,s,loc,z,-lv/2 !creating constraint equations at the fixed end to allow warping of the face
da,all,all,0

allsel

asel,s,loc,z,(2*M-1)*lv/2 !creating constraint equations at the loaded end
da,all,uy,-0.01

allsel

/solu
solve
save
finish

/post1
etable,sene,sene ! Retrieve strain energy per element
ssum ! Sum strain energy from ETABLE
*GET,my_Energy,SSUM,0,Item1,SENE ! Gets SENE from ETABLE and defines it as "my_Energy"
```

## Appendix 7 – ANSYS script used for creation and compression of the perturbed array

```

/filename,compressionperturbed2x2x4,1
/prep7 !Enter preprocessor

A=60
!Defining lengths for points
!Lh=(13.74*A+288)*1e-3 !Lh defined in mm
Lh=1.35344745 !Lh defined in mm
!Lv=(6.74*A+456)*1e-3 !Lv defined in mm
Lv=1.35344745 !Lv defined in mm
!points
k,1,0,0,0
k,2,Lv/2,0,0
k,3,0,Lv/2,0
k,4,-Lv/2,0,0
k,5,0,-Lv/2,0
k,6,0,0,Lh/2
k,7,0,0,-Lh/2

!create lines
*do,i,2,7,1
l,1,i,i
*enddo

!rv=(0.14*A+208)*1e-3/2 !Radius in mm
rv=0.1626338581 !Radius in mm
!rh=(-1.03*A+189)*1e-3/2 !Radius in mm
rh=0.1626338581 !Radius in mm

!Additional points for defining circles out of the working plane
k,8,-Lv/2,0,rh
k,9,0,Lv/2,rh

!creating thick cylinders
circle,6,rv
al,7,8,9,10
vdrag,1,,,,,5,6

!creating thin cylinders
circle,4,rh,1,8
al,27,28,29,30
vdrag,12,,,,,3,1

circle,3,rh,1,9
al,47,48,49,50
vdrag,23,,,,,2,4

vadd,all !combine all volumes into one volume
numcmp,all

!Material properties
mp,ex,,12e3
mp,prxy,,0.3

et,,solid185
esize,rh/3
MSHKEY,0 !use free meshing
MSHAPE,1,3d !use triangular elements
vmesh,all !mesh volume

!create (K)x(L)x(M) array
!e.g. K=3 gives a 4x4x4 array
K=2
L=2
M=4

vgen,K,1,,lv
nummg,all
numcmp,all

VGEN,L,1,K,1,,lv
nummg,all
numcmp,all

VGEN,M,1,K*L,1,,lh
nummg,all
numcmp,all

/NERR,,,-1 !ignore warning/error messages

esize,rh
MSHKEY,0 !use free meshing
MSHAPE,1,3d !use triangular elements
vmesh,all !mesh volume

!Fixing the edges so perturbations can be applied to the middle
asel,s,loc,k,-lv/2
asel,a,loc,k,lv*(2^K-1)/2
asel,a,loc,y,-lv/2
asel,a,loc,y,lv*(2^L-1)/2
asel,a,loc,z,-lh/2
asel,a,loc,z,lh*(2^M-1)/2
da,all,all,0

*dim,ARR,array,K,L,M !define a 3-D array with size according to the number of unit cells
*do,i,1,K
*do,ii,1,L
*do,iii,1,M
*vfill,arr(i,ii,iii),gdis,0,lv
*enddo
*enddo
*enddo

```

```

!applying the displacements to the middle points

*do,i,1,K,1
*do,j,1,L,1
*do,ll,1,M,1

      seltol,rv          !selection tolerance
      nsel,s,loc,x,(i-1)*Lv
      nsel,r,loc,y,(j-1)*Lv
      nsel,r,loc,z,(ll-1)*Lh

      d,all,ux,ARR(i,j,ll)
      d,all,uy,ARR(i,j,ll)
      d,all,uz,ARR(i,j,ll)
*enddo
*enddo
*enddo

allsel

dtran
ftran

/solu
solve
save
finish

/prep7
lsclear,all          !clear all oprevious loads and B.C.s
upgeom,0.05,1,1,compressionperturbed2x2x4,rst  !Update the geometry to the deformed state that was obtained by the previous loads to a deformation scale scale of 0.1
/NERR,,,-1          !ignore warning/error messages

!Axial loading (Loads and B.C.s)
seltol
nsel,s,loc,x,-lv/2
d,all,ux,0
nsel,s,loc,y,-lv/2
d,all,uy,0
nsel,s,loc,z,-lh/2
d,all,uz,0

nsel,s,loc,z,lh*(2*M-1)/2
d,all,uz,-0.001*Lh*(M)

allsel
dtran
ftran

/solu
solve
save
finish

/post1
etable,sene,sene          ! Retrieve strain energy per element
ssum                    ! Sum strain energy from ETABLE
*GET,my_Energy,SSUM,0,Item1,SENE  ! Gets SENE from ETABLE and defines it as "my_Energy"

```

## Appendix 8 – ANSYS script used for creation and torsion of the perturbed array

```

/filename,torsionperturbed0_05_2x2x4,1
/prep7 !Enter preprocessor

A=60
!Defining lengths for points
!Lh=(13.74*A+288)*1e-3 !Lh defined in mm
Lh=1.35344745 !Lh defined in mm
!Lv=(6.74*A+456)*1e-3 !Lv defined in mm
Lv=1.35344745 !Lv defined in mm
!points
k,1,0,0,0
k,2,Lv/2,0,0
k,3,0,Lv/2,0
k,4,-Lv/2,0,0
k,5,0,-Lv/2,0
k,6,0,0,Lh/2
k,7,0,0,-Lh/2

!create lines
*do,i,2,7,1
l,i,i
*enddo

!rv=((0.14*A+208)*1e-3)/2 !Radius in mm
rv=0.1626338581 !Radius in mm
!rh=(-1.03*A+189)*1e-3)/2 !Radius in mm
rh=0.1626338581 !Radius in mm

!Additional points for defining circles out of the working plane
k,8,-Lv/2,0,rh
k,9,0,Lv/2,rh

!creating thick cylinders
circle,6,rv
al,7,8,9,10
vdrag,1,,,,,5,6

!creating thin cylinders
circle,4,rh,1,8
al,27,28,29,30
vdrag,12,,,,,3,1

circle,3,rh,1,9
al,47,48,49,50
vdrag,23,,,,,2,4

vadd,all !combine all volumes into one volume
numcmp,all

!Material properties
mp,ex,,12e3
mp,prxy,,0.3

et,,solid185
esize,rh/3
MSHKEY,0 !use free meshing
MSHAPE,1,3d !use triangular elements
vmesh,all !mesh volume

!Create (K)x(L)x(M) array
K=2
L=2
M=4

vgen,K,1,,lv
numcmp,all

VGEN,L,1,K,1,,lv
numcmp,all

VGEN,M,1,K*L,1,,lh
numcmp,all

nummr,all
numcmp,all

/NERR,,,-1 !ignore warning/error messages

esize,rh/4
MSHKEY,0 !use free meshing
MSHAPE,1,3d !use triangular elements
vmesh,all !mesh volume

!Fixing the edges so perturbations can be applied to the middle
asel,s,loc,x,-lv/2
asel,a,loc,x,lv*(2*K-1)/2
asel,a,loc,y,-lv/2
asel,a,loc,y,lv*(2*L-1)/2
asel,a,loc,z,-lh/2
asel,a,loc,z,lh*(2*M-1)/2
da,all,all,0

*dim,ARR,array,K,L,M !define a 3-D array with size according to the number of unit cells
*do,i,1,K
*do,ii,1,L
*do,iii,1,M
*vfill,arr(i,ii,iii),gdis,0,lv
*enddo
*enddo
*enddo

```

```

!applying the displacements to the middle points
*do,i,1,K,1
*do,j,1,L,1
*do,ll,1,M,1

      seltol,rv          !selection tolerance
      nsel,s,loc,x,(i-1)*Lv
      nsel,r,loc,y,(j-1)*Lv
      nsel,r,loc,z,(ll-1)*Lh

      d,all,ux,ARR(i,j,ll)
      d,all,uy,ARR(i,j,ll)
      d,all,uz,ARR(i,j,ll)
*enddo
*enddo
*enddo

allsel

dtran
ftran

/solu
solve
save
finish

/prep7
!sclear,all          !clear all oprevious loads and B.C.s
upgeom,0.05,1,1,torsionperturbed0.05_2x2x4,rst !Update the geometry to the deformed state that was obtained by the previous loads to a deformation scale scale of 0.1
/NERR,,-1          !ignore warning/error messages

!Torsion loading (Loads and B.C.s)
*get,nmax,node,,num,max          !get highest node number

et,2,mass21          !creating a mass element so that master nodes can have this element type
r,2,1,1,1,1,1

n,,(K-1)*(lv/2),(L-1)*lv/2,-lv/2-0.05 !master node for the fixed face
Type,2
Real,2
E,nmax+1

n,,(K-1)*(lv/2),(L-1)*lv/2,(2*M-1)*lv/2+0.05 !master node for the loaded face
Type,2
Real,2
E,nmax+2

allsel

nsel,s,loc,z,-lv/2          !creating constraint equations at the fixed end to allow warping of the face
nsel,a,node,,nmax+1
cerig,nmax+1,all,uy,ux

nsel,s,loc,z,(2*M-1)*lv/2 !creating constraint equations at the loaded end
nsel,a,node,,nmax+2
cerig,nmax+2,all,uy,ux

allsel
d,nmax+1,all,0          !master node B.C.s for the fixed end
!dlist

theta=0.05          !angle of twist in radians
d,nmax+2,ux,0
d,nmax+2,uy,0
d,nmax+2,uz,0
d,nmax+2,rotz,theta          !master node torsion for the loaded end
allsel
!dlist

!mpchg,1,all          !assign material properties to all elements

allsel

/solu
solve
save
finish

/post1
etable,sene,sene          ! Retrieve strain energy per element
ssum          ! Sum strain energy from ETABLE
*GET,my_Energy,SSUM,0,Item1,SENE          ! Gets SENE from ETABLE and defines it as "my_Energy"

```

## Appendix 9 – ANSYS script used for creation and cantilever bending of the perturbed array

```

/filename,bendingperturbed0_05_2x2x4,1
/prep7 !Enter preprocessor

A=60
!Defining lengths for points
!Lh=(13.74*A+288)*1e-3 !Lh defined in mm
Lh=1.35344745 !Lh defined in mm
!Lv=(6.74*A+456)*1e-3 !Lv defined in mm
Lv=1.35344745 !Lv defined in mm
!points
k,1,0,0,0
k,2,Lv/2,0,0
k,3,0,Lv/2,0
k,4,-Lv/2,0,0
k,5,0,-Lv/2,0
k,6,0,0,Lh/2
k,7,0,0,-Lh/2

!create lines
*do,1,2,7,1
l,1,1
*enddo

!rv=((0.14*A+208)*1e-3)/2 !Radius in mm
rv=0.1626338581 !Radius in mm
!rh=(-1.03*A+189)*1e-3/2 !Radius in mm
rh=0.1626338581 !Radius in mm

!Additional points for defining circles out of the working plane
k,8,-Lv/2,0,rh
k,9,0,Lv/2,rh

!creating thick cylinders
circle,6,rv
al,7,8,9,10
vdrag,1,,,,,5,6

!creating thin cylinders
circle,4,rh,1,8
al,27,28,29,30
vdrag,12,,,,,3,1

circle,3,rh,1,9
al,47,48,49,50
vdrag,23,,,,,2,4

vadd,all !combine all volumes into one volume
numcmp,all

!Material properties
mp,ex,,12e3
mp,prxy,,0.3

et,,solid185
esize,rh/3
MSHKEY,0 !use free meshing
MSHAPE,1,3d !use triangular elements
vmesh,all !mesh volume
!Create (K)x(L)x(M) array
!e.g. K=3 gives a 4x4x4 array
K=2
L=2
M=4

vgen,K,1,,,lv
nummg,all
numcmp,all

VGEN,L,1,K,1,,lv
nummg,all
numcmp,all

VGEN,M,1,K*L,1,,,lh
nummg,all
numcmp,all

/NERR,,, -1 !ignore warning/error messages

esize,rh
MSHKEY,0 !use free meshing
MSHAPE,1,3d !use triangular elements
vmesh,all !mesh volume

!Fixing the edges so perturbations can be applied to the middle
asel,s,loc,x,-lv/2
asel,a,loc,x,lv*(2*K-1)/2
asel,a,loc,y,-lv/2
asel,a,loc,y,lv*(2*L-1)/2
asel,a,loc,z,-lh/2
asel,a,loc,z,lh*(2*M-1)/2
da,all,all,0

*dim,ARR,array,K,L,M !define a 3-D array with size according to the number of unit cells
*do,i,1,K
*do,ii,1,L
*do,iii,1,M
*vfill,arr(i,ii,iii),gdis,0,lv
*enddo
*enddo
*enddo

```

```

!applying the displacements to the middle points

*do,i,1,K,1
*do,j,1,L,1
*do,ll,1,M,1

      seltol,rv          !selection tolerance
      nsel,s,loc,x,(i-1)*Lv
      nsel,r,loc,y,(j-1)*Lv
      nsel,r,loc,z,(ll-1)*Lh

          d,all,ux,ARR(i,j,ll)
          d,all,uy,ARR(i,j,ll)
          d,all,uz,ARR(i,j,ll)
*enddo
*enddo
*enddo

allsel

dtran
ftran

/solu
solve
save
finish

/prep7
!sclear,all          !clear all oprevious loads and B.C.s
upgeom,0.05,1,1,bendingperturbed0_05_2x2x4,rst !Update the geometry to the deformed state that was obtained by the previous loads to a deformation scale scale of 0.1
/NERR,,,-1          !ignore warning/error messages

!Axial loading (Loads and B.C.s)
seltol
nsel,s,loc,z,-lh/2
d,all,all,0

nsel,s,loc,z,lh*(2*M-1)/2
d,all,uy,-0.01

allsel

/solu
solve
save
finish

/post1
etable,sene,sene          ! Retrieve strain energy per element
ssum                    ! Sum strain energy from ETABLE
*GET,my_Energy,SSUM,0,Item1,SENE ! Gets SENE from ETABLE and defines it as "my_Energy"

```

Appendix 10 – ANSYS script used for creation and compression of the cubic array

```

/cwd,/mnt/lustre/qdb15201/FEresults
/filename,5x5x10cubicarraycompression

/prep7

!r=0.1626338581
r=0.07658
Lt=1.353344746

K=5
L=5
M=10

k,1,0,0,0
k,2,0,Lt,0
k,3,Lt,Lt,0
k,4,Lt,0,0
k,5,0,0,Lt
k,6,0,Lt,Lt
k,7,Lt,Lt,Lt
k,8,Lt,0,Lt

1,1,2
1,2,3
1,3,4
1,4,1

1,2,6
1,3,7
1,4,8
1,1,5

1,5,6
1,6,7
1,7,8
1,8,5

circle,1,r,5,2
al,13,14,15,16

circle,1,r,2,5
al,17,18,19,20

circle,4,r,1,3
al,21,22,23,24

circle,4,r,3,1
al,25,26,27,28

circle,4,r,8,3
al,29,30,31,32

circle,2,r,3,6
al,33,34,35,36

circle,2,r,6,3
al,37,38,39,40

circle,3,r,7,2
al,41,42,43,44

circle,5,r,6,8
al,45,46,47,48

circle,5,r,8,6
al,49,50,51,52

circle,8,r,7,5
al,53,54,55,56

circle,7,r,6,8
al,57,58,59,60

vdrag,1,,,,,5
vdrag,2,,,,,3
vdrag,3,,,,,2
vdrag,3,,,,,2
vdrag,4,,,,,1
vdrag,6,,,,,2
vdrag,7,,,,,6
vdrag,8,,,,,7
vdrag,5,,,,,8
vdrag,9,,,,,9
vdrag,10,,,,,12
vdrag,11,,,,,11
vdrag,12,,,,,10

vadd,all !combine all volumes into one volume
numcmp,all

sph4,r,r,r
vgen,,2,,, -r, -r,,,1
vgen,2,2,,, Lt,,,0
vgen,2,2,,, Lt,,0
vgen,2,2,,, Lt,Lt,,0
vgen,2,2,,, Lt,,,0
vgen,2,2,,, Lt,Lt,,,0
vgen,2,2,,, Lt,Lt,,0
vgen,2,2,,, Lt,Lt,Lt,,0

vadd,all
numcmp,all

!Material properties
mp,ex,,12e3
mp,prxy,,0.3

!Element type (Tetrahedral 4-node brick element)
et,,solid185
esize,r/3
MSHKEY,0
MSHAPE,1,3d
vmesh,all !use free meshing
!use triangular elements
!mesh volume

```

```

!Create (K)x(L)x(M) array
vgen,K,1,,Lt
numcmp,all

VGEN,L,1,K,1,,Lt
numcmp,all

VGEN,M,1,K*L,1,,Lt
numcmp,all

nummrg,all
numcmp,all

/NERR,,-1          !ignore warning/error messages

!Compression loading (Loads and B.C.s)
nset,s,loc,z,-r
d,all,uz,0

nset,s,loc,y,-r
d,all,uy,0

nset,s,loc,x,-r
d,all,ux,0

allsel

nset,s,loc,z,(Lt*M)+r
d,all,uz,-0.001*(Lt*(M)+r)

allsel

/solu
solve
save
finish

/post1
etable,sene,sene          ! Retrieve strain energy per element
ssum                     ! Sum strain energy from ETABLE
*GET,my_Energy,SSUM,0,Item1,SENE  ! Gets SENE from ETABLE and defines it as "my_Energy"

```

## Appendix 11 – ANSYS script used for creation and torsion of the cubic array

```

/cwd,/mnt/lustre/qdb15201/FEresults
/filename,5x5x10cubicarraytorsion

/prep7

r=0.07658
Lt=1.353344746

K=5
L=5
M=10

k,1,0,0,0
k,2,0,Lt,0
k,3,Lt,Lt,0
k,4,Lt,0,0
k,5,0,0,Lt
k,6,0,Lt,Lt
k,7,Lt,Lt,Lt
k,8,Lt,0,Lt

l,1,2
l,2,3
l,3,4
l,4,1

l,2,6
l,3,7
l,4,8
l,1,5

l,5,6
l,6,7
l,7,8
l,8,5

circle,1,r,5,2
al,13,14,15,16

circle,1,r,2,5
al,17,18,19,20

circle,4,r,1,3
al,21,22,23,24

circle,4,r,3,1
al,25,26,27,28

circle,4,r,8,3
al,29,30,31,32

circle,2,r,3,6
al,33,34,35,36

circle,2,r,6,3
al,37,38,39,40

circle,3,r,7,2
al,41,42,43,44

circle,5,r,6,8
al,45,46,47,48

circle,5,r,8,6
al,49,50,51,52

circle,8,r,7,5
al,53,54,55,56

circle,7,r,6,8
al,57,58,59,60

vdrag,1,,,,,5
vdrag,2,,,,,3
vdrag,3,,,,,2
vdrag,3,,,,,2
vdrag,4,,,,,1
vdrag,6,,,,,2
vdrag,7,,,,,6
vdrag,8,,,,,7
vdrag,5,,,,,8
vdrag,9,,,,,9
vdrag,10,,,,,12
vdrag,11,,,,,11
vdrag,12,,,,,10

vadd,all          !combine all volumes into one volume
numcmp,all

sph4,r,r,r
vgen,,2,,, -r, -r,,,,1
vgen,2,2,,,Lt,,,0
vgen,2,2,,,Lt,,,0
vgen,2,2,,,Lt,Lt,,,0
vgen,2,2,,,Lt,,,0
vgen,2,2,,,Lt,Lt,,,0
vgen,2,2,,,Lt,Lt,,,0
vgen,2,2,,,Lt,Lt,Lt,,,0

vadd,all
numcmp,all

!Material properties
mp,ex,1,12e3
mp,prxy,1,0.3

!Element type (Tetrahedral 4-node brick element)
et,,solid185
esize,r/2
MSHKEY,0          !use free meshing
MSHAPE,1,3d      !use triangular elements
vmesh,all        !mesh volume

```

```

!Create (K)x(L)x(M) array
vgen,K,1,,Lt
numcmp,all

VGEN,L,1,K,1,,Lt
numcmp,all

VGEN,M,1,K*L,1,,Lt
numcmp,all

nummrg,all
numcmp,all

/NERR,,,-1          !ignore warning/error messages

!Torsion loading (Loads and B.C.s)
*get,maxx,node,,mxloc,x          !retrieve maximum x-position
*get,maxy,node,,mxloc,y          !retrieve maximum y-position
*get,maxz,node,,mxloc,z          !retrieve maximum z-position
*get,minx,node,,mnloc,x          !retrieve minimum x-position
*get,miny,node,,mnloc,y          !retrieve minimum y-position
*get,minz,node,,mnloc,z          !retrieve minimum z-position

*get,nmax,node,,num,max          !get highest node number

et,2,mass21              !creating a mass element so that master nodes can have this element type
r,2,1,1,1,1,1

n,nmax+1,minx+((maxx-minx)/2),miny+((maxy-miny)/2),minz-0.05          !master node for the fixed face
Type,2
Real,2
E,nmax+1

n,nmax+2,minx+((maxx-minx)/2),miny+((maxy-miny)/2),maxz+0.05          !master node for the loaded face
Type,2
Real,2
E,nmax+2

allsel

nset,s,loc,z,minz          !creating constraint equations at the fixed end to allow warping of the face
nset,a,node,,nmax+1
cerig,nmax+1,all,uy,ux

allsel

nset,s,loc,z,maxz          !creating constraint equations at the loaded end
nset,a,node,,nmax+2
cerig,nmax+2,all,uy,ux

allsel
d,nmax+1,all,0          !master node B.C.s for the fixed end
!dlist

theta=0.05              !angle of twist in radians
d,nmax+2,ux,0
d,nmax+2,uy,0
d,nmax+2,uz,0
d,nmax+2,rotz,theta          !master node torsion for the loaded end
allsel
!dlist

!mpchg,1,all          !assign material properties to all elements

/solu
solve
save
finish

/post1
etable,sene,sene          ! Retrieve strain energy per element
ssum                    ! Sum strain energy from ETABLE
*GET,my_Energy,SSUM,0,Item1,SENE          ! Gets SENE from ETABLE and defines it as "my_Energy"

```

## Appendix 12 – ANSYS script used for creation and cantilever of the cubic array

```

/cwd,/mnt/lustre/qdb15201/FEresults
/filename,3x3x6cubicarraybending

/prep7

!r=0.1626338581
r=0.07658
Lt=1.353344746

K=3
L=3
M=6

k,1,0,0,0
k,2,0,Lt,0
k,3,Lt,Lt,0
k,4,Lt,0,0
k,5,0,0,Lt
k,6,0,Lt,Lt
k,7,Lt,Lt,Lt
k,8,Lt,0,Lt

l,1,2
l,2,3
l,3,4
l,4,1

l,2,6
l,3,7
l,4,8
l,1,5

l,5,6
l,6,7
l,7,8
l,8,5

circle,1,r,5,2
al,13,14,15,16

circle,1,r,2,5
al,17,18,19,20

circle,4,r,1,3
al,21,22,23,24

circle,4,r,3,1
al,25,26,27,28

circle,4,r,8,3
al,29,30,31,32

circle,2,r,3,6
al,33,34,35,36

circle,2,r,6,3
al,37,38,39,40

circle,3,r,7,2
al,41,42,43,44

circle,5,r,6,8
al,45,46,47,48

circle,5,r,8,6
al,49,50,51,52

circle,8,r,7,5
al,53,54,55,56

circle,7,r,6,8
al,57,58,59,60

vdrag,1,,,,,5
vdrag,2,,,,,3
vdrag,3,,,,,2
vdrag,3,,,,,2
vdrag,4,,,,,1
vdrag,6,,,,,2
vdrag,7,,,,,6
vdrag,8,,,,,7
vdrag,5,,,,,8
vdrag,9,,,,,9
vdrag,10,,,,,12
vdrag,11,,,,,11
vdrag,12,,,,,10

vadd,all          !combine all volumes into one volume
numcmp,all
|
sph4,r,r,r
vgen,,2,,, -r,-r,,,1
vgen,2,2,,,Lt,,,0
vgen,2,2,,,Lt,,0
vgen,2,2,,,Lt,Lt,,0
vgen,2,2,,,Lt,,,0
vgen,2,2,,,Lt,Lt,,0
vgen,2,2,,,Lt,Lt,Lt,,0

vadd,all
numcmp,all

!Material properties
mp,ex,,12e3
mp,prxy,,0.3

!Element type (Tetrahedral 4-node brick element)
et,,solid185
esize,r/3
MSHKEY,0          !use free meshing
MSHAPE,1,3d      !use triangular elements
vmesh,all        !mesh volume

```

```

!Create (K)x(L)x(M) array
vgen,K,1,,Lt
numcmp,all

VGEN,L,1,K,1,,Lt
numcmp,all

VGEN,M,1,K*L,1,,Lt
numcmp,all

nummrg,all
numcmp,all

/NERR,,,-1           !ignore warning/error messages

!Compression loading (Loads and B.C.s)
nset,s,loc,z,-r
d,all,all,0

allsel

nset,s,loc,z,(Lt*M)+r
d,all,uy,-0.01

allsel

/solu
solve
save
finish

/post1
etable,sene,sene           ! Retrieve strain energy per element
ssum                       ! Sum strain energy from ETABLE
*GET,my_Energy,SSUM,0,Item1,SENE ! Gets SENE from ETABLE and defines it as "my_Energy"

```

Appendix 13 – ANSYS script used for creation and compression of the cubic array with

added diagonals

```

/cwd,/mnt/lustre/qdb15201/FEresults
/filename,5x5x10cubicarraydiagonalscompression

```

```
/prep7
```

```

r=0.05387
Lt=1.353344746

```

```

K=5
L=5
M=10

```

```

k,1,0,0,0
k,2,0,Lt,0
k,3,Lt,Lt,0
k,4,Lt,0,0
k,5,0,0,Lt
k,6,0,Lt,Lt
k,7,Lt,Lt,Lt
k,8,Lt,0,Lt

```

```

1,1,2
1,2,3
1,3,4
1,4,1

```

```

1,2,6
1,3,7
1,4,8
1,1,5

```

```

1,5,6
1,6,7
1,7,8
1,8,5

```

```

circle,1,r,5,2
al,13,14,15,16

```

```

circle,1,r,2,5
al,17,18,19,20

```

```

circle,4,r,1,3
al,21,22,23,24

```

```

circle,4,r,3,1
al,25,26,27,28

```

```

circle,4,r,8,3
al,29,30,31,32

```

```

circle,2,r,3,6
al,33,34,35,36

```

```

circle,2,r,6,3
al,37,38,39,40

```

```

circle,3,r,7,2
al,41,42,43,44

```

```

circle,5,r,6,8
al,45,46,47,48

```

```

circle,5,r,8,6
al,49,50,51,52

```

```

circle,8,r,7,5
al,53,54,55,56

```

```

circle,7,r,6,8
al,57,58,59,60

```

```

vdrag,1,,,,,5
vdrag,2,,,,,3
vdrag,3,,,,,2
vdrag,4,,,,,1
vdrag,6,,,,,2
vdrag,7,,,,,6
vdrag,8,,,,,7
vdrag,5,,,,,8
vdrag,9,,,,,9
vdrag,10,,,,,12
vdrag,11,,,,,11
vdrag,12,,,,,10

```

```

sph4,r,r,r
vgen,,13,,, -r, -r,,,,1
vgen,2,13,,, Lt,,,0
vgen,2,13,,, Lt,,0
vgen,2,13,,, Lt,Lt,,0
vgen,2,13,,, Lt,,,,0
vgen,2,13,,, Lt,Lt,,,0
vgen,2,13,,, Lt,,Lt,,0
vgen,2,13,,, Lt,Lt,Lt,,0

```

---

```

!creating diagonals
circle,1,r,7
al,189,190,191,192
l,1,7
vdrag,89,,,,,193

circle,2,r,8
al,202,203,204,205
l,2,8
vdrag,95,,,,,206

circle,6,r,4
al,215,216,217,218
l,6,4
vdrag,101,,,,,219

circle,5,r,3
al,228,229,230,231
l,5,3
vdrag,107,,,,,232

!Create (K)x(L)x(M) array
vgen,K,all,,,Lt
vgen,L,all,,,Lt
vgen,M,all,,,Lt

nummrg,all
numcmp,all

/NERR,,,-1          !ignore warning/error messages

!Material properties
mp,ex,1,12e3
mp,prxy,1,0.3

!Element type (Tetrahedral 4-node brick element)
et,,solid185
esize,r/2
MSHKEY,0             !use free meshing
MSHAPE,1,3d         !use triangular elements
vmesh,all           !mesh volume

nummrg,all

!Compression loading (Loads and B.C.s)
nsel,s,loc,z,-r
d,all,uz,0

```

---

```
nselect,s,loc,y,-r  
d,all,uy,0
```

```
nselect,s,loc,x,-r  
d,all,ux,0
```

```
allselect
```

```
nselect,s,loc,z,(Lt*M)+r  
d,all,uz,-0.001*(Lt*(M)+r)
```

```
allselect
```

```
/solu  
solve  
save  
finish
```

```
/post1
```

```
etable,sene,sene
```

```
! Retrieve strain energy per element
```

```
ssum
```

```
! Sum strain energy from ETABLE
```

```
*GET,my_Energy,SSUM,0,Item1,SENE
```

```
! Gets SENE from ETABLE and defines it as "my_Energy"
```

## Appendix 14 – ANSYS script used for creation and torsion of the cubic array with

```

/cwd,/mnt/lustre/qdb15201/FEresults
/filename,5x5x10cubicarraydiagonaltorsion

/prep7

r=0.05387
Lt=1.353344746

K=5
L=5
M=10

k,1,0,0,0
k,2,0,Lt,0
k,3,Lt,Lt,0
k,4,Lt,0,0
k,5,0,0,Lt
k,6,0,Lt,Lt
k,7,Lt,Lt,Lt
k,8,Lt,0,Lt

l,1,2
l,2,3
l,3,4
l,4,1

l,2,6
l,3,7
l,4,8
l,1,5

l,5,6
l,6,7
l,7,8
l,8,5

circle,1,r,5,2
al,13,14,15,16

circle,1,r,2,5
al,17,18,19,20

circle,4,r,1,3
al,21,22,23,24

circle,4,r,3,1
al,25,26,27,28

circle,4,r,8,3
al,29,30,31,32

circle,2,r,3,6
al,33,34,35,36

circle,2,r,6,3
al,37,38,39,40

circle,3,r,7,2
al,41,42,43,44

circle,5,r,6,8
al,45,46,47,48

circle,5,r,8,6
al,49,50,51,52

circle,8,r,7,5
al,53,54,55,56

circle,7,r,6,8
al,57,58,59,60

vdrag,1,,,,,5
vdrag,2,,,,,3
vdrag,3,,,,,2
vdrag,4,,,,,1
vdrag,6,,,,,2
vdrag,7,,,,,6
vdrag,8,,,,,7
vdrag,5,,,,,8
vdrag,9,,,,,9
vdrag,10,,,,,12
vdrag,11,,,,,11
vdrag,12,,,,,10

sph4,r,r,r
vgen,,13,,, -r, -r,,,,,1
vgen,2,13,,, Lt,,,0
vgen,2,13,,,, Lt,,0
vgen,2,13,,, Lt,Lt,,0
vgen,2,13,,, Lt,,,0
vgen,2,13,,, Lt,Lt,,,0
vgen,2,13,,, Lt,, Lt,,0
vgen,2,13,,, Lt,Lt,Lt,,0

!creating diagonals
circle,1,r,7
al,189,190,191,192
l,1,7
vdrag,89,,,,,193

circle,2,r,8
al,202,203,204,205
l,2,8
vdrag,95,,,,,206

circle,6,r,4
al,215,216,217,218
l,6,4
vdrag,101,,,,,219

circle,5,r,3
al,228,229,230,231
l,5,3
vdrag,107,,,,,232

```

added diagonals

```

!Create (K)x(L)x(M) array
vgen,K,all,,Lt
vgen,L,all,,Lt
vgen,M,all,,Lt

nummrg,all
numcmp,all

/NERR,,,-1          !ignore warning/error messages

!Material properties
mp,ex,1,12e3
mp,prxy,1,0.3

!Element type (Tetrahedral 4-node brick element)
et,,solid185
esize,r/2
MSHKEY,0           !use free meshing
MSHAPE,1,3d       !use triangular elements
vmesh,all         !mesh volume

nummrg,all

!Torsion loading (Loads and B.C.s)
*get,maxx,node,,mxloc,x      !retrieve maximum x-position
*get,maxy,node,,mxloc,y      !retrieve maximum y-position
*get,maxz,node,,mxloc,z      !retrieve maximum z-position
*get,minx,node,,mnloc,x      !retrieve minimum x-position
*get,miny,node,,mnloc,y      !retrieve minimum y-position
*get,minz,node,,mnloc,z      !retrieve minimum z-position

*get,nmax,node,,num,max      !get highest node number

et,2,mass21          !creating a mass element so that master nodes can have this element type
r,2,1,1,1,1

n,nmax+1,minx+((maxx-minx)/2),miny+((maxy-miny)/2),minz-0.05      !master node for the fixed face
Type,2
Real,2
E,nmax+1

n,nmax+2,minx+((maxx-minx)/2),miny+((maxy-miny)/2),maxz+0.05      !master node for the loaded face
Type,2
Real,2
E,nmax+2

allsel

nset,s,loc,z,minz          !creating constraint equations at the fixed end to allow warping of the face
nset,a,node,,nmax+1
cerig,nmax+1,all,uy,ux

allsel

nset,s,loc,z,maxz          !creating constraint equations at the loaded end
nset,a,node,,nmax+2
cerig,nmax+2,all,uy,ux

allsel
d,nmax+1,all,0            !master node B.C.s for the fixed end
!dlist

theta=0.05                !angle of twist in radians
d,nmax+2,ux,0
d,nmax+2,uy,0
d,nmax+2,uz,0
d,nmax+2,rotz,theta      !master node torsion for the loaded end
allsel
!dlist

d,1,uz,0                  !fix one node so that the model does not move in the z-direction

!mpchg,1,all              !assign material properties to all elements

/solu
solve
save
finish

/post1
etable,sene,sene          ! Retrieve strain energy per element
ssum                      ! Sum strain energy from ETABLE
*GET,my_Energy,SSUM,0,Item1,SENE ! Gets SENE from ETABLE and defines it as "my_Energy"

```

Appendix 15 – ANSYS script used for creation and cantilever bending of the cubic array with added diagonals

```

/cwd,/mnt/lustre/qdb15201/FEResults
/filename,5x5x10cubicarraydiagonalsbending

/prep7

r=0.05387
Lt=1.353344746

K=5
L=5
M=10

k,1,0,0,0
k,2,0,Lt,0
k,3,Lt,Lt,0
k,4,Lt,0,0
k,5,0,0,Lt
k,6,0,Lt,Lt
k,7,Lt,Lt,Lt
k,8,Lt,0,Lt

l,1,2
l,2,3
l,3,4
l,4,1

l,2,6
l,3,7
l,4,8
l,1,5

l,5,6
l,6,7
l,7,8
l,8,5

circle,1,r,5,2
al,13,14,15,16

circle,1,r,2,5
al,17,18,19,20

circle,4,r,1,3
al,21,22,23,24

circle,4,r,3,1
al,25,26,27,28

circle,4,r,8,3
al,29,30,31,32

circle,2,r,3,6
al,33,34,35,36

circle,2,r,6,3
al,37,38,39,40

circle,3,r,7,2
al,41,42,43,44

circle,5,r,6,8
al,45,46,47,48

circle,5,r,8,6
al,49,50,51,52

circle,8,r,7,5
al,53,54,55,56

circle,7,r,6,8
al,57,58,59,60

vdrag,1,,,,,5
vdrag,2,,,,,3
vdrag,3,,,,,2
vdrag,4,,,,,1
vdrag,6,,,,,2
vdrag,7,,,,,6
vdrag,8,,,,,7
vdrag,5,,,,,8
vdrag,9,,,,,9
vdrag,10,,,,,12
vdrag,11,,,,,11
vdrag,12,,,,,10

sph4,r,r,r
vgen,,13,,, -r, -r,,,,1
vgen,2,13,,, Lt,,,0
vgen,2,13,,, Lt,,,0
vgen,2,13,,, Lt,Lt,,,0
vgen,2,13,,, Lt,,,0
vgen,2,13,,, Lt,Lt,,,0
vgen,2,13,,, Lt,Lt,,,0
vgen,2,13,,, Lt,Lt,Lt,,,0

!creating diagonals
circle,1,r,7
al,189,190,191,192
l,1,7
vdrag,89,,,,,193

circle,2,r,8
al,202,203,204,205
l,2,8
vdrag,95,,,,,206

circle,6,r,4
al,215,216,217,218
l,6,4
vdrag,101,,,,,219

circle,5,r,3
al,228,229,230,231
l,5,3
vdrag,107,,,,,232

```

```

!Create (K)x(L)x(M) array
vgen,K,all,,,Lt
vgen,L,all,,,Lt
vgen,M,all,,,,Lt

nummrg,all
numcmp,all

/NERR,,-1          !ignore warning/error messages

!Material properties
mp,ex,1,12e3
mp,prxy,1,0.3

!Element type (Tetrahedral 4-node brick element)
et,,solid185
esize,r/2
MSHKEY,0          !use free meshing
MSHAPE,1,3d      !use triangular elements
vmesh,all        !mesh volume

nummrg,all

!Compression loading (Loads and B.C.s)
nset,s,loc,z,-r
d,all,all,0

allsel

nset,s,loc,z,(Lt*M)+r
d,all,uy,-0.01

allsel

/solu
solve
save
finish

/post1
etable,sene,sene          ! Retrieve strain energy per element
ssum                     ! Sum strain energy from ETABLE
*GET,my_Energy,SSUM,0,Item1,SENE ! Gets SENE from ETABLE and defines it as "my_Energy"

```

